

Alma Mater Studiorum - Università di Bologna

DOTTORATO DI RICERCA IN  
MECCANICA E SCIENZE AVANZATE DELL'INGEGNERIA

Ciclo 34

**Settore Concorsuale:** 09/A1 - INGEGNERIA AERONAUTICA, AEROSPAZIALE E NAVALE

**Settore Scientifico Disciplinare:** ING-IND/05 - IMPIANTI E SISTEMI AEROSPAZIALI

DEEP SPACE ORBIT DETERMINATION AND GUIDANCE OF THE LICIA CUBE  
MICROSATELLITE MISSION

**Presentata da:** Igor Gai

**Coordinatore Dottorato**

Marco Carricato

**Supervisore**

Paolo Tortora

**Co-supervisore**

Marco Zannoni

**Esame finale anno 2022**



To my family.



# Author's Note

This thesis is continuously revised to correct all typos that are found during a never-ending revision process. To obtain the most updated version, please feel free to contact the author by sending an e-mail to: `igor.gai@unibo.it`.

Some of the information contained in this document, including but not limited to spacecraft system specifications, trajectories, scientific and technical data are classified as confidential information. Therefore, this document shall not be disclosed to others than the authorized people until those information are disclosed to the public.



# DEEP SPACE ORBIT DETERMINATION AND GUIDANCE OF THE LICIAcube MICROSATELLITE MISSION

## Abstract

Since the CubeSat standard was born for educational purposes in the 2000s, the launches of such objects exponentially increased with time. After less than 20 years, thanks also to their very short design and manufacturing time, this new class of nano and microsattelites today offers many applications for near-Earth purposes, with a strong heritage in these kinds of missions. Recently, the Jet Propulsion Laboratory (JPL)'s Mars Cube One (MarCO) mission demonstrated that these probes are also mature enough to be employed in the deep space, even though with the limitations related to the employed commercial components. Currently, other deep space CubeSats are planned either as stand-alone missions or as companions of a traditional large probe. Among the latter are the Juventas and Milani CubeSats that will be deployed by the European Space Agency (ESA) Hera probe once it reaches the Didymos system.

Therefore, developing a dedicated navigation suite is crucial to reaching the mission's goals, considering the limitations of the onboard components compared to typical deep space missions. In this framework, the Light Italian Cubesat for Imaging of Asteroids (LICIAcube) mission represents an ideal candidate test-bench, as it performs a flyby of the Didymos asteroid system subject to a strong position, epochs, and pointing requirements. This mission will also allow us to infer the capabilities of such microsattelites and highlight their limitations compared with the benefits of a lighter design and tailoring efforts. In this work, the Orbit Determination (OD) and guidance methods and tools adopted for classical deep space missions have been tailored for the CubeSat applications and validated through extensive analyses. In addition, navigation procedures and interfaces have been designed in view of the operations foreseen in late 2022. The pre-launch covariance analysis has been performed to assess the mission's feasibility for the nominal trajectory and its associated uncertainties, based on conservative assumptions on the main parameters. Extensive sensitivity analyses have been carried out to understand the main mission parameters affecting the performance and to demonstrate the robustness of the designed trajectory and operation schedule in fulfilling the mission requirements. The developed system was also stressed by tuning the models to access different reconstruction methods for the maneuvers. The analysis demonstrated the feasibility of the LICIAcube mission navigation in compliance with the mission requirements, compatible with the limited resources available, both in space and on the ground.

---



# Acknowledgements

First of all, I have to express my gratitude to Prof. Paolo Tortora for granting me the opportunity to work on this project and proving himself a fair person and always available for support. A great thanks to Marco Zannoni, who has supported me with the on-field work, with neverending discussions (many of them on the return train). He demonstrated to be a friend as well as an excellent teacher. Similarly, I should thank all the radiosience and planetary exploration lab friends more than colleagues. I need to name at least Luis Gomez, who assisted me since the beginning of my PhD, and Marco Lombardo, with whom I worked very close.

I also wish to thank the LICIACube team for the continuous work we're doing together and the JPL's Dan Lubey and Matt Smith for the valuable discussions for developing the work.

A great thanks to all my friends who were so close also during the isolation.

Last but not least, a huge thanks to my family, who always supported me. Thanks, I should extend to my brothers Davide and Angelica and my parents, Paolo and Cosetta, and my grandparents. They worked hard to provide the family's future generations the opportunity to reach higher education. Finally, thanks to my beloved half, my wife Alessia, who stands by my side throughout all this time. She shared with me the happiness (as well as the burden and the stress) of this great project.

---



# Acronyms

<b>AFC</b>	Asteroid Framing Camera
<b>AIDA</b>	Asteroid Impact and Deflection Assessment
<b>AIM</b>	Asteroid Impact Mission
<b>ADCS</b>	Attitude Determination and Control Subsystem
<b>AMC</b>	Advanced Media Calibrations
<b>APL</b>	Applied Physics Laboratory
<b>ASI</b>	Italian Space Agency
<b>C/A</b>	Closest Approach
<b>DART</b>	Double Asteroid Redirection Test
<b>DCO</b>	Data Cut-Off
<b>DRA</b>	Design Reference Asteroid
<b>DRACO</b>	Didymos Reconnaissance and Asteroid Camera for Optical navigation
<b>DSN</b>	Deep Space Network
<b>EME2000</b>	Earth Mean Equator at J2000
<b>EMO2000</b>	Earth Mean Orbit at J2000
<b>ESA</b>	European Space Agency
<b>FOV</b>	Field of View
<b>FPC</b>	Flight Path Control
<b>GNC</b>	Guidance, Navigation and Control
<b>G/S</b>	Ground Station
<b>ICD</b>	Interface Control Document
<b>INAF</b>	Istituto Nazionale di Astrofisica
<b>I/O</b>	Input and Output
<b>ISL</b>	Inter-Satellite Link
<b>JHU</b>	Johns Hopkins University
<b>JPL</b>	Jet Propulsion Laboratory
<b>LAMBIC</b>	Linear Analysis of Maneuvers with Bounds and Inequality Constraints
<b>LEIA</b>	LICIACube Explorer Imaging for Asteroid
<b>LICIACube</b>	Light Italian Cubesat for Imaging of Asteroids
<b>LIDAR</b>	LIght Detection And Ranging

<b>LTOF</b>	Linearized Time of Flight
<b>LUKE</b>	LICIACube Unit Key Explorer
<b>MA</b>	Mission Analysis
<b>MCC</b>	Mission Control Center
<b>MarCO</b>	Mars Cube One
<b>MOC</b>	Mission Operations Center
<b>MONTE</b>	Mission-analysis and Operations Navigation Toolkit Environment
<b>NASA</b>	National Aeronautics and Space Administration
<b>NAV</b>	Navigation
<b>NEA</b>	Near Earth Asteroid
<b>NEXT-C</b>	NASA's Evolutionary Xenon Thruster - Commercial
<b>NEO</b>	Near Earth Object
<b>OD</b>	Orbit Determination
<b>OM</b>	Orbital Maneuver
<b>OPNAV</b>	Optical Navigation
<b>PHA</b>	Potentially Hazardous Asteroid
<b>PL</b>	Payload
<b>POLIMI</b>	Polytecnic of Milan
<b>PS</b>	Propulsion System
<b>ROSA</b>	Deployable Space Systems Roll-Out Solar Array
<b>RCS</b>	Reaction Control System
<b>RMS</b>	Root Mean Square
<b>RW</b>	Reaction Wheel
<b>S/C</b>	spacecraft
<b>SEP</b>	Sun-Earth-Probe
<b>SFTP</b>	SSH File Transfer Protocol
<b>SMART Nav</b>	Small-body Maneuvering Autonomous Real-Time Navigation
<b>SOC</b>	Science Operations Center
<b>SPA</b>	Sun Phase Angle
<b>SRP</b>	Solar Radiation Pressure
<b>SSDC</b>	Space Science Data Center
<b>STM</b>	State Transition Matrix
<b>TCA</b>	Time of Closest Approach
<b>TSAC</b>	Tracking System Analytical Calibration
<b>UNIBO</b>	University of Bologna
<b>USO</b>	Ultra Stable Oscillator

# Contents

<b>1</b>	<b>Introduction</b>	<b>1</b>
1.1	Dissertation aim . . . . .	1
1.2	Deep space CubeSats . . . . .	2
1.3	Planetary defense missions . . . . .	3
1.3.1	The Didymos system . . . . .	3
1.3.2	DART . . . . .	5
1.3.3	Hera . . . . .	6
1.4	The Navigation problem . . . . .	6
1.4.1	The Orbit Determination problem . . . . .	6
1.4.2	The Flight Path Control problem . . . . .	12
<b>2</b>	<b>The LICIACube mission</b>	<b>15</b>
2.1	Introduction . . . . .	15
2.2	The spacecraft . . . . .	16
2.2.1	Technical specifications . . . . .	17
2.3	Science objectives . . . . .	18
2.4	Navigation objectives . . . . .	19
2.5	Trajectory design . . . . .	20
2.5.1	B-plane definition . . . . .	20
2.5.2	Procedure . . . . .	21
2.5.3	Orbital maneuvers . . . . .	22
2.5.4	Reference trajectory . . . . .	24
2.6	Mission timeline . . . . .	25
2.6.1	Tracking schedule . . . . .	25
2.6.2	Optical navigation schedule . . . . .	27
2.6.3	Maneuvers schedule . . . . .	29
2.6.4	Data Cut-Offs . . . . .	30
2.6.5	Attitude . . . . .	31
<b>3</b>	<b>Navigation model</b>	<b>33</b>
3.1	Rotational models . . . . .	33
3.1.1	Didymos primary . . . . .	33
3.1.2	Didymos secondary . . . . .	34
3.2	Didymos dynamical model . . . . .	35
3.2.1	Didymos system . . . . .	35
3.2.2	Dimorphos . . . . .	36
3.3	Shape models . . . . .	38
3.4	Gravitational models . . . . .	38
3.4.1	Didymos primary . . . . .	39

3.4.2	Didymos secondary . . . . .	40
3.5	Light Italian Cubesat for Imaging of Asteroids (LICIACube) spacecraft models . . . . .	41
3.5.1	Initial conditions . . . . .	41
3.5.2	Forces . . . . .	42
3.5.3	Shape . . . . .	43
3.5.4	Solar Radiation Pressure . . . . .	44
3.5.5	Maneuvers . . . . .	45
3.5.6	Stochastics . . . . .	45
<b>4</b>	<b>Orbit Determination simulations</b>	<b>47</b>
4.1	Introduction . . . . .	47
4.2	Procedure . . . . .	47
4.2.1	Requirements verification . . . . .	49
4.3	Measurements . . . . .	51
4.3.1	Radio-tracking . . . . .	53
4.3.2	Optical measurements . . . . .	54
4.4	Maneuvers execution . . . . .	56
4.5	Parameters . . . . .	57
4.6	Baseline results . . . . .	58
4.7	Robustness analysis . . . . .	67
4.7.1	A-priori covariance . . . . .	68
4.7.2	Observables . . . . .	76
4.7.3	Maneuver model . . . . .	82
<b>5</b>	<b>Flight Path Control simulations</b>	<b>85</b>
5.1	Introduction . . . . .	85
5.2	Statistical $\Delta v$ analysis . . . . .	85
5.3	Validation procedure . . . . .	87
5.4	Results . . . . .	88
<b>6</b>	<b>Operations preparation</b>	<b>93</b>
6.1	Introduction . . . . .	93
6.2	Interfaces . . . . .	93
6.3	Navigation operations . . . . .	94
6.3.1	Staff . . . . .	95
6.3.2	Processes . . . . .	95
6.3.3	Maneuvers . . . . .	97
6.4	Tools . . . . .	99
6.5	Testing . . . . .	100
<b>7</b>	<b>Conclusions and future perspectives</b>	<b>103</b>
	<b>List of Figures</b>	<b>105</b>
	<b>List of Tables</b>	<b>107</b>
	<b>Bibliography</b>	<b>109</b>

# Chapter 1

## Introduction

### Contents

---

<b>1.1</b>	<b>Dissertation aim</b>	<b>1</b>
<b>1.2</b>	<b>Deep space CubeSats</b>	<b>2</b>
<b>1.3</b>	<b>Planetary defense missions</b>	<b>3</b>
1.3.1	The Didymos system	3
1.3.2	DART	5
1.3.3	Hera	6
<b>1.4</b>	<b>The Navigation problem</b>	<b>6</b>
1.4.1	The Orbit Determination problem	6
1.4.2	The Flight Path Control problem	12

---

### 1.1 Dissertation aim

In the framework of CubeSats navigation in the deep space, this dissertation thesis aims at providing a suitable toolkit for the Orbit Determination (OD) software Mission-analysis and Operations Navigation Toolkit Environment (MONTE) [25]. The developed environment takes into account typical tasks from space mission phases A to E, namely from preliminary analysis up to the operations. This work also includes particular considerations for the peculiarity of CubeSats in deep space as previous missions experiences, power, data budget, and radio-tracking limitations. The developed software relies on different tools aimed at the following goals:

- preliminary study of the scientific objectives to formalize the Navigation (NAV) requirements;
- assessment of the expected performances of the baseline to support the trajectory design and the mission timeline definition;
- extended covariance analysis to verify the requirements compliance and the system robustness;
- operations planning, to define the interfaces for data exchange between the operations control center and the NAV team;
- operations support, providing a suitable set of tools for OD and ancillary tools for quick debugging, such as data visualization and editing;

- operations preparation, to define a set of procedures for the real-time operations based on the feasibility and the mission requirements;
- operations preliminary testing, to check all the previous points in a closed loop with other teams.

## 1.2 Deep space CubeSats

The CubeSats were born in the 2000s as a small satellite standard for educational purposes. Their initial aim was to provide experience to university students about the development of a real near-Earth space mission. Thus, the standard was developed to shrink the design and manufacturing times and costs, including standardization of the weight and dimensions for the probes as multiple of 1U (called *unit*), given by a 10 cm-sided cube, as defined by the CubeSats Design Specification [17]. With the increasing number of launched missions in the low Earth orbit and thanks to the miniaturization efforts providing for a large number of standard off-the-shelf components, the cost of such CubeSats eventually dropped, and they began to attract the attention of a larger users group, composed of space agencies and private companies. Therefore, the number of this kind of probes launched has shown an exponential growth ever since the project was born, reaching over 1600 CubeSats launched by the end of 2021 [40]. Simultaneously, the increasing heritage of past missions improved the components' reliability and increased the range of possible applications. The employment of the CubeSats spreads among many different purposes, including - but not limited to - technological demonstrator, Earth observation, space weather monitoring, and remote sensing [62]. In addition to this stand-alone configuration, the CubeSats may also be employed in a multi-spacecraft way, for instance, as mother-daughter spaceships, constellations, or swarms [64].

Conversely, deep space missions typically have a very high design, development, and operating costs which entailed these missions take a long time from acceptance to spacecraft flight. Moreover, the developed items usually apply older technologies with a long heritage or new technology with the drawback of extended test and qualification time. Therefore, the technology onboard a large probe of interplanetary missions is often old as the spacecraft leaves. Of course, it would not be possible to demand to a CubeSat the tasks of an interplanetary probe, but one may take advantage of an expensive Earth orbit escape launch to add extra spacecraft(s) to cover complementary duties and retrieve the highest mission return with a minor cost in flown mass [64]. In this context, the heritage acquired by the near-Earth CubeSats made these probes great candidates for deep space missions. CubeSats may be either used as stand-alone or carried by the main spacecraft to the mission target, depending on the apparent limitation on the available  $\Delta V$  required. A large number of CubeSats deep space missions are currently planned in the incoming years, starting from the lunar orbits opportunity provided by Orion for the first Space Launch System flight (e.g., Argomoon [21]) up to interplanetary applications with mother and daughter spacecraft, such as LICIACube carried by Double Asteroid Redirection Test (DART) or Juventas and Milani onboard of Hera.

The unique deep space CubeSat mission already flown took advantage of the InSight launch. The twin probes Mars Cube One (MarCO) [44] demonstrated the feasibility of CubeSat in a deep space mission, although they highlighted significant limitations mostly related to the standard components' performance and reliability. After its separation from the Atlas V Centaur upper stage, right after InSight, the CubeSats were independently navigated toward Mars to demonstrate the feasibility of these probes in deep space. A

shortcoming of particular interest for this dissertation is related to the problem experienced with the propulsion system by both the probes. During the cruise to Mars, a plenum valve leakage provoked the propellant condensation, thus leading to an anomalous thrust. The NAV team identified this issue and promptly corrected it with adequate mitigation actions. Nonetheless, the anomaly was reported, and following investigations attributed the issue to the lack of extensive testing before launch for the characterization of the propulsion system. Although the mission goals were finally achieved, this should represent an important starting point for considerations about future deep space CubeSat missions.

### 1.3 Planetary defense missions

Near Earth Objects (NEOs) represent a class of celestial bodies whose orbit about the Sun has a perihelion lower than 1.3 AU and includes both asteroids and comets. The asteroids population, known as Near Earth Asteroids (NEAs), is generally composed of rocky objects with very different diameters. A subset of these bodies, which may potentially cause major damages in case of impact with the Earth, is named Potentially Hazardous Asteroids (PHAs). This class of object includes the asteroids with a mean diameter larger than 140 m and a minimum orbit intersection distance to Earth lower than 0.05 AU [50]. As the known population of NEOs has been dramatically increasing in the last decades, the statistics of a potentially catastrophic event grows as well, although keeping to a very low probability. Nonetheless, the ability to be prepared for such events may represent the only chance for humankind's survival.

Planetary defense missions aim at preventing impact with a PHA with many different viable techniques. Among them, gravity tractor requires a long time to provide a substantial effect, whereas nuclear explosion deflection by radiation is judged to be the only feasible solution for asteroids much larger than 100 meters in diameter [2]. Nonetheless, the most effective deflection technique for smaller asteroids, whose impact on Earth is assumed to be more probable [70], is the impact with a rocket-launched spacecraft. In the past years, some missions have been proposed, such as the European Space Agency (ESA)'s Don Quijote mission concept [12], ancestor of the modern DART mission. In July 2005, the National Aeronautics and Space Administration (NASA)'s Deep Impact already demonstrated the capability to autonomously achieve a high speed ( $\sim 10.3$  km/s) impact on a celestial body, the comet Tempel 1 [1]. Nevertheless, that mission goal was to investigate the comet nucleus, so the low spacecraft-to-comet mass ratio did not allow a measurement of the induced heliocentric deflection. Other rendezvous missions targeting tasks have been successfully achieved to study the composition of similar bodies either by probes touchdown for Hayabusa missions on the asteroids Itokawa and Ryugu respectively [28, 39] and Philae lander on the comet 67P/Churyumov-Gerasimenko for the Rosetta mission [46].

Two main planetary defense missions are planned for the 2020s to the Didymos asteroids system, HERA and DART, both part of the international cooperation project between ESA and NASA - the Asteroid Impact and Deflection Assessment (AIDA).

#### 1.3.1 The Didymos system

The (65803) Didymos system is a binary asteroids system - hence named after the Greek God of twins - discovered in 1996 by the University of Arizona Steward Observatory Spacewatch survey. The system is composed of two asteroids [53] - the primary called Didymos of a mean diameter of 780 m, and a secondary named Dimorphos of mean

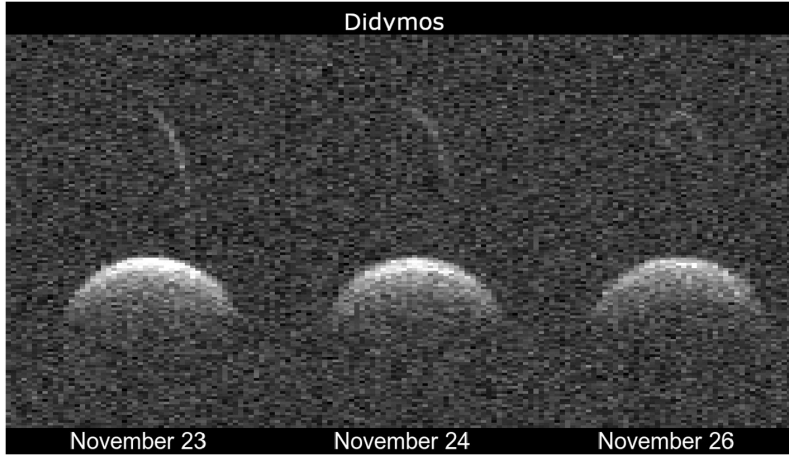


Figure 1.1: (65803) Didymos sum of daily delay-Doppler observation obtain using Arecibo [48]. The larger object at the bottom is Didymos primary, whereas the curved smear at the top is Dimorphos trajectory arc covered during the observation time span.

diameter of about 160 m - and has a low obliquity retrograde orbit about the Sun. Table 1.1 shows the orbital parameters of Didymos. Like most of the binary near-Earth asteroids,

Table 1.1: Heliocentric orbital parameters of (65803) Didymos [37].

Parameter	Value	Unit
Reference epoch	2459600.5 (2022-Jan-21.0)	TDB
Eccentricity	0.383	
Inclination	3.408	deg
Period	2.108	years

the Didymos system is asynchronous, namely the primary rotation period is shorter than the mutual one. The secondary observed data mainly comes from photometric by [52], eventually confirmed by lightcurve and radar imaging by Arecibo [53]. Figure 1.1 shows radar observations daily sum, which highlights the presence of a secondary object orbiting the primary. The primary bulk density is typical of the S-type range [19], whereas the secondary one is unknown: predictions constrained the secondary density to be similar or smaller than the primary [66]. For this reason, whatever the internal model of Dimorphos, it should be relatively compact with a density similar to the primary.

Given the particular nature of binary asteroids and the hypotheses related to their origin and possible evolution [66, 65], the Didymos binary asteroid is interesting to the in-situ exploration to allow deeper investigations of its internal structure and composition. Moreover, in the context of planetary protection, the Didymos system represents an ideal candidate for the intentional impact of a spacecraft (S/C). Although Didymos is not a threat to Earth, it was the most accessible known binary asteroid (at the epoch of the mission's proposal) in terms of required  $\Delta V$  and the impact on the secondary asteroid may produce a measurable effect on its rotational period, as explained in the following section. In addition, Dimorphos has the typical size of asteroids which may threaten the Earth.

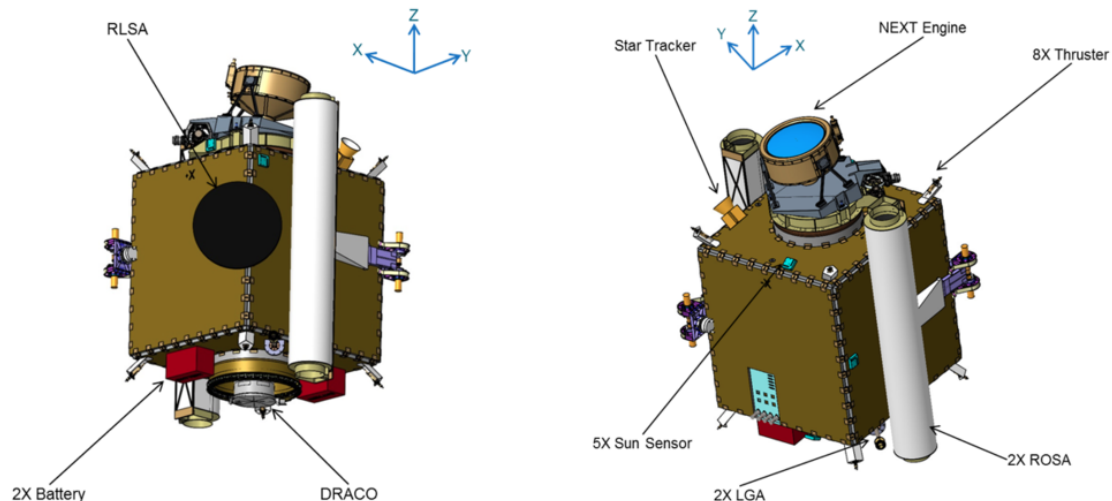


Figure 1.2: DART 3D view, with rolled-up solar arrays. Source: [nasa.gov/planetarydefense/dart](https://nasa.gov/planetarydefense/dart)

### 1.3.2 DART

The Double Asteroid Redirection Test (DART) is a NASA mission developed by Johns Hopkins University (JHU) Applied Physics Laboratory (APL) as a technological demonstrator to assess an asteroid redirection by impact [55, 13]. After almost a year of cruise using the NASA’s Evolutionary Xenon Thruster - Commercial (NEXT-C) ion-engine electric propulsion, DART will impact Dimorphos with a relative speed of about 6.6 km/sec. The spacecraft mounts a single optical payload, the Didymos Reconnaissance and Asteroid Camera for Optical navigation (DRACO). This high-resolution imager will collect science data and support the Small-body Maneuvering Autonomous Real-Time Navigation (SMART Nav) in the final approach to the target. The propulsion system is fed by the two Deployable Space Systems Roll-Out Solar Arrays (ROSAs) used to recharge the probe’s batteries. A view of the DART spacecraft is depicted in figure 1.2 in the solar arrays rolled-up configuration.

Since it is a feasibility study, DART does not aim at shifting the heliocentric trajectory of the asteroid. Conversely, it will impact the Didymos secondary to produce an observable delay in its rotation period about the primary. In order to maximize the observability with the minimum propellant cost, a retrograde impact to Dimorphos is planned, namely reaching it in the direction opposite to its rotation velocity with respect to Didymos primary. The impact will cause a decrease of the orbital energy of the secondary rotation about the primary, expected to be larger than 73s per orbit, corresponding to 10% of the period, to be observable from ground telescopes [13]. Based on different models used, it is foreseen the formation of a crater and the generation of an ejecta plume that will be studied thanks to the flyby pictures acquired by LICIAcube. Mounted on a piggyback dispenser, the CubeSat LICIAcube will travel to the system until its release a few days before the DART impact to support the post-impact data collection (further details in section 2).

DART was launched from Vandenberg US Air Force base on November 24th, 2021 and is planned to reach and impact Dimorphos at the end of September 2022.

### 1.3.3 Hera

Based on the previous concept of Asteroid Impact Mission (AIM), Hera (named after the Greek God of marriage) is a mission of the ESA [45]. Hera is aimed at the Didymos system with a planned arrival date a few years later than DART when the impact-generated ejecta will not be observable anymore. However, by injecting the spacecraft into a low-altitude Didymos orbit, it will be possible to retrieve a detailed characterization of the Didymos asteroids, including information about the gravity field, composition, spectrometry, and DART crater. This information should improve the results obtained by the data of DART and LICIAcube.

Hera will be equipped with the Asteroid Framing Camera (AFC) inherited by the NASA DAWN mission to perform both navigation and high-resolution imaging of the asteroids. Moreover, the spacecraft mounts a laser altimeter, the LIght Detection And Ranging (LIDAR), employed to reconstruct the asteroid's shapes, topography, and mass and to support the study of the surface composition.

To achieve its mission goals, Hera will carry in-situ two 6U CubeSats, Juventas [30] and Milani [27], to perform the planned analyses. Moreover, these will act as a demonstrator of the Inter-Satellite Link (ISL) used by the two picosatellites to communicate with the mothership Hera.

## 1.4 The Navigation problem

The S/C *reference trajectory* is computed in advance by the mission design to optimize the scientific return of the mission against the minimization of the propellant consumption. Nonetheless, the actual trajectory followed during the operations is often different due both to the mismodeling of the model used to compute the reference trajectory and to the errors in the *real world*, such as the release errors, maneuvers execution errors, attitude errors. The general problem of spacecraft navigation consists of the acquisition of measurements used to retrieve the actual state of the spacecraft and the subsequent correction through orbital maneuvers. A schema of the entire process is summarized in figure 1.3, where the dashed box represents the trajectory reconstruction, namely the OD, and the outer block of guidance, also known as Flight Path Control (FPC), refers to the trajectory control. A detailed mathematical formulation of the OD and FPC processes is given in the following. Moreover, the implemented model, observables, and the main error sources that may affect the results can be found in the chapter 3.

### 1.4.1 The Orbit Determination problem

The OD problem is an iterative process that estimates a set of parameters relative to a body motion [31]. This process is performed by comparing some acquired observables to the corresponding ones simulated by dedicated software, which implements a detailed model of the problem dynamics and the observables generation. During this dissertation thesis, this task is demanded to the JPL's OD software MONTE [25].

According to the schema in figure 1.3, the OD process relies on two types of models to reflect the real world: one is provided for the dynamic of the spacecraft and the celestial bodies of interest, one for the measurements. Thus, it would be possible to provide a prediction of the trajectories for all the bodies in the model and compute the spacecraft observables, referred to as *computed observables*. These are eventually compared with the *observed observables*, namely the acquired measurements, obtaining the *residuals*. If the environment was perfectly modeled and the real and the modeled worlds perfectly

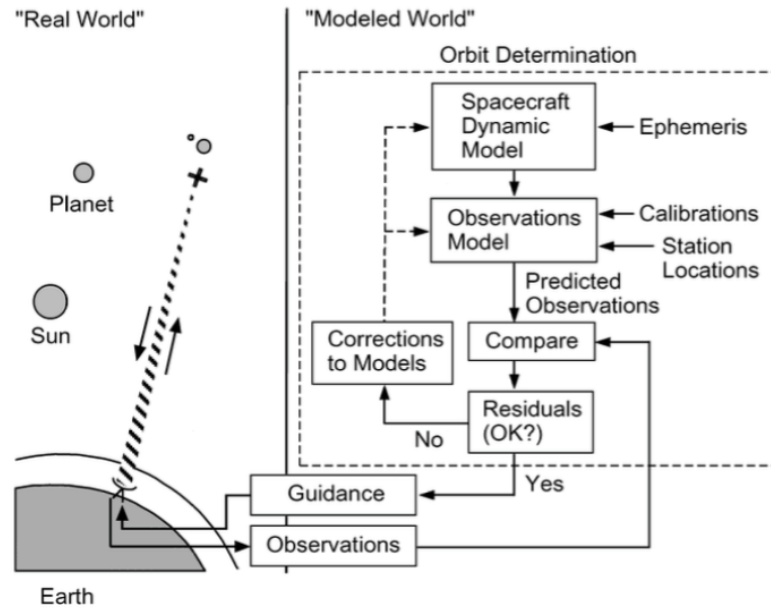


Figure 1.3: Schematic representation of the OD process [60].

match, the residuals would consist of only the measurement noise, for simplicity, assumed zero-mean, white, and gaussian. Due to practical mismodeling and errors, signatures are introduced into the residuals requiring the tuning of the models' parameters, usually applying a linearized batch weighted least-square filter to fit the residual. Because the models are not linear, the procedure must be iterated until convergence. Therefore, the OD solution is the set of parameters value which minimized the weighted residual, in a least-square sense [9]. The set of solve-for parameters shall contain at least the spacecraft's initial state, although any parameter that affects the probe's trajectory could be included. Thus the set of parameters extends, for instance, to states and gravity fields of the celestial bodies, but also other spacecraft's properties such as maneuvers or Solar Radiation Pressure (SRP) coefficients.

A detailed mathematical formulation of the statistical OD has been developed by [59] in the chapter 4 and [61] in chapter 9. Although, it is worth recalling a few basic concepts.

Let us assume the general OD problem, given the following non-linear dynamical model:

$$\begin{cases} \dot{\mathbf{x}} = f(\mathbf{x}, t) \\ \mathbf{x}(t_0) \end{cases} \quad (1.1)$$

where  $\mathbf{x}$  is the  $n \times 1$  state vector including, at least, the spacecraft state. The observable model relates the state vector to the measurements:

$$y_i = g_i(\mathbf{x}(t_i), t_i) \quad i \in [1, \dots, m] \quad (1.2)$$

where  $\mathbf{y}$  is the  $m \times 1$  observables vector. Therefore the least-squares estimation consists in the computation of the state  $\hat{\mathbf{x}}$  based on the *computed observables*  $\hat{\mathbf{y}}$  and subject to the cost function to be minimized:

$$J = \sum_{i=1}^m \delta \hat{\mathbf{y}}_i^2 \quad (1.3)$$

being  $\delta\hat{\mathbf{y}} = \mathbf{y} - \hat{\mathbf{y}}$  the residual between the *observed* and the *computed observables*. Equation 1.3 can be modified accounting for the measurements noise, given the standard deviations of the  $i$ -th observable  $\sigma_i$ , as:

$$J = \sum_{i=1}^m \left( \frac{\delta\hat{\mathbf{y}}_i}{\sigma_i} \right)^2 = (\mathbf{y} - \hat{\mathbf{y}}(\hat{\mathbf{x}}))W(\mathbf{y} - \hat{\mathbf{y}}(\hat{\mathbf{x}}))^T \quad (1.4)$$

said  $W$  the matrix of the observables weights. In addition, called  $A = \partial\hat{\mathbf{y}}/\partial\hat{\mathbf{x}}$  the matrix of observation partials, namely the variation of the observable with respect to a change in the parameters, and assuming a linearized first order approximation, the state can be estimated by an iterative method, whose correction step can be written as:

$$\delta\hat{\mathbf{x}}_k = (A^TWA)^{-1}A^TW(\delta\hat{\mathbf{y}}) \quad (1.5)$$

Called  $P_0^{-1}$  the *a priori* information matrix, i.e. the inverse of the *a priori* covariance matrix, and  $\tilde{\mathbf{x}}$  the *a priori* state vector correction, we obtain:

$$\delta\hat{\mathbf{x}}_k = (A^TWA + P_0^{-1})^{-1}(A^TW\delta\hat{\mathbf{y}} + P_0^{-1}\tilde{\mathbf{x}}) \quad (1.6)$$

The first term of the equation 1.6 is usually called covariance matrix,  $P_{\hat{\mathbf{x}}}$ .

$$P_{\hat{\mathbf{x}}} = (A^TWA + P_0^{-1})^{-1} \quad (1.7)$$

This contains the information about the formal accuracy and the correlation among the different solve-for parameters. In fact, each element of the main diagonal  $P_{\hat{\mathbf{x}}_{ii}}$  is related to the uncertainty of the  $i$ -th parameter  $\sigma_i$  as:

$$\sqrt{P_{\hat{\mathbf{x}}_{ii}}} = \sigma_i \quad (1.8)$$

whereas the off-diagonal elements expresses the covariance of the  $i$ -th and  $j$ -th parameters:

$$P_{\hat{\mathbf{x}}_{ij}} = \rho_{ij}\sigma_i\sigma_j \quad (1.9)$$

being  $\rho_{ij}$  the correlation coefficient between the  $i$ -th and  $j$ -th parameters. Note that the formal accuracy is estimated through the OD process, and thus, usually, it is not realistic. This is caused by multiple sources generally related to the simplifications in the adopted assumptions including the *a priori* weights, the non-white noise, and, above all, the model errors. About this latter one, the linearization of a nonlinear dynamic system is usually compensated by conservative assumptions on the process noise covariance to obtain reliable results.

## Observables

An observable is any measured physical quantity carrying information about the solve-for parameters. Among many types, the typical observables used in deep space navigation are:

- Range, obtained from the round-trip light time of a modulated signal transmitted between a Ground Station (G/S) and the S/C, in range units;
- Range-rate, obtained from the Doppler shift, namely the frequency shift of the carrier of the received signal with respect to the transmitted signal;

- DDOR (Delta - Differential One-way Range), computed as the difference between the reception time of the same signal received by two widely-separated ground stations, which allows obtaining an angular measurement of the S/C along the stations' baseline (DOR), eventually compared to the same measure of a nearby radio source (quasar), to infer the precise probe's position;
- Optical observables, obtained from optical pictures of the target body taken from the probe, providing any direct measurement of the S/C position relative to a target body and/or features on the surface of the target.

For the LICIACube mission, the main observables used are the two-way range and the range-rate (F2). The choice to discard the one-way and three-way range-rate (F1 and F3) observables was made due to the lower precision related to the S/C clock stability and the inter-station clock drift, respectively. The typical two-way configuration is based on the round-trip of the signal, which is transmitted from the ground source to the S/C (uplink) and back to the same transmitting ground station (downlink). In this configuration, the S/C receiver locks the uplink carrier, demodulates the signal, and re-modulates it on a downlink carrier coherently to the uplink but with a frequency different from the uplink one. Changing in the carrier frequency is required to avoid interference between the transmitting and receiving signals, which shall be in different bands. The uplink and downlink carriers' frequencies are standardized and related by a precise turn-around ratio ( $M_2$ ).

The opportunity for optical measurements is also taken into account in this dissertation, but the exact availability will be strongly related to the effective data rate required to download these observables, which are considerable in data size.

**Range observables** The range observables measure the trip light-time employed by the modulated signal (as an electromagnetic wave) to travel at the speed of light between an emitter and a receiver. The employed two-way configuration exploits the modulation shift of the ground received signal to compute its delay. As a first approximation, it represents the sum round-trip light time of uplink and downlink:

$$\tau = \frac{\rho_u + \rho_d}{c} \quad (1.10)$$

being  $\rho_u$  and  $\rho_d$  represents the one-way range, in uplink and downlink respectively, and  $c$  is the speed of light.

**Range-rate** The range-rate observables exploit the Doppler shift of the signal that provide a measure of the relative radial velocity. Assume the uplink signal transmitted from the ground station with a frequency  $f_T$ , at a given time  $t_1$ . The signal is acquired by the probe at the time  $t_2$ , with a given Doppler shift dependent to the relative radial velocity between the S/C and the ground station. Finally, the probe transmits a coherent downlink signal, with a turn-around ratio  $M_2$ , back to the Earth. The ground station receives the signal at  $t_3$  with a frequency  $f_R$  which, as first approximation, is

$$f_R = \left(1 - \frac{\dot{\rho}_u + \dot{\rho}_d}{c}\right) f_T \quad (1.11)$$

The Doppler shift is obtained by integrating the phase change over the Doppler cycle count, providing a measure of the mean range-rate. Thus, the integrated Doppler observables

over a count-time (or integration time) interval  $T_c$  can be written as:

$$F = \frac{1}{T_c} \int_{\bar{t}-T_c/2}^{\bar{t}+T_c/2} (f_{ref} - f_T) dt \quad (1.12)$$

where  $\bar{t}$  corresponds to the midpoint epoch of  $T_c$  and  $f_{ref}$  is an arbitrary reference frequency, usually  $M_2 \cdot f_T$ .

**Optical observables** Unlike Earth-based observables such as range and Doppler, the optical observables are acquired directly by the spacecraft without the need for any ground support. Of course, this implies the presence of dedicated navigation or scientific optical payload, which could be used to retrieve navigation images. Furthermore, since the OD tasks are performed on Earth, the images have to be downloaded, with an additional data rate and time cost. The main application of the optical observables is to provide information on the relative position of the spacecraft with respect to the target(s). Due to geometric considerations, optical images provide information mainly in the so-called plane-of-sky, intended as the plane perpendicular to the camera boresight. In general, the contribution provided in the radial direction is quite scarce. Formally speaking, the optical observable is not intended to be the *raw* image, but the information content has to be retrieved by pre-processing [20]. This procedure aims at extracting data points information as pixels' relative distances and shapes fitting, which could be quantified as parameters in the filter. Different methods are currently used to obtain processable measurements, depending on the distance and targets dimension in the picture. The most used methods are:

- **centerfinding:** this method [8] can be applied either to resolved (larger objects in the Field of View (FOV)) or unresolved (smaller objects or stars) bodies. In the former case, either limb-fitting (to get the target shape) or brightness centerfinding algorithms may be applied to determine the body centroid. In the latter case, the point-spread function is usually exploited to find the center of the illuminated area.
- **feature tracking:** when the object is large, or even greater than the FOV, features (landmarks) can be detected on the target surface. Therefore, relevant data could be extrapolated by comparing multiple pictures of the same landmarks together with the shape model of the object.

This latter method requires larger manipulation and is more complicated; furthermore, in the approach phase, the target images will not be large enough to have a resolved object in the FOV. Therefore only the centerfinding method will be applied for the LICIACube mission.

### Noise sources

The attainable accuracy of the OD is limited by various error sources that may affect the measured observables, both radio- and optical-based. The most relevant sources of error relative to the radio-tracking observables [60] are:

- **instrumental noise**, due to random processes inside the electronic components both in the ground station and the spacecraft segments. This noise is mainly related to the *system noise temperature*, or *thermal noise*.

- **clock instabilities**, related to the oscillator errors in the generation of the reference frequency, which directly translates into errors in the range-rate measurements. Since the stability of the oscillator is an intrinsic characteristic of the clock, the F2 configuration is used to minimize the clock instability errors using the same ground station to remove deviations introduced by different clocks, using the same oscillator to generate initial and final reference frequency. Conversely, both F1 and F3 configurations are affected by this noise due to the usage of different clocks (ground and S/C) and the inter-station clock offset present using two different ground stations, respectively. Inter-station clock drift can be calibrated with good accuracy so that F3 can be used. Instead, the F1 usage for navigation purposes requires the employment of a very precise onboard clock, for instance, an Ultra Stable Oscillator (USO).
- **dynamical mismodelling**, namely any imperfection in the model due to non-deterministic and non-gravitational models, which affects the observables by the erroneous integrated S/C trajectory.
- **transmission media**, inducing a path delay when the signal propagates through any media. The transmission media can be divided into dispersive and non-dispersive media, depending on whether the induced delay is frequency-dependent.

In a dispersive media, the induced path delay decrease with the inverse of the squared frequency, so higher frequencies are less susceptible to dispersive noise. Thanks to this property, the induced path delay of a signal can be corrected via multi-frequency link calibrations[43, 6]. Typical sources of dispersive noise are the Earth's ionosphere and the solar plasma. In the absence of a multi-frequency link, the Earth's ionosphere can be calibrated with good accuracy using GNSS-based techniques.

Conversely, the delay induced by non-dispersive media is not frequency-dependent. It is mainly caused by the Earth's troposphere and consists of two contributions: the dry component causes a stable but larger delay, whereas the wet component is responsible for a smaller, but not stable, delay. Despite the former contribution being location dependent, thus related to the ground station area, the latter is instead due to the water content in the atmosphere along the antenna-spacecraft line of sight. The tropospheric delays can be calibrated through the Tracking System Analytical Calibration (TSAC) and Advanced Media Calibrations (AMC).

The optical observables are also susceptible to error sources, such as:

- **instrumental noise**, the same random noise induced on the radio components also affects the imager sensors, causing mismatching in the single pixels or entire stripes.
- **dynamical mismodelling**, as already said, may cause an incorrect expected spacecraft state, thus providing errors in the expected target position in the images.
- **mechanical misalignments**, caused either by imperfect mounting or by thermal expansion, which may cause a camera boresight orientation different than expected. It can be partially corrected by ground and operative calibrations.
- **sensors defects** can be caused by dead or hot pixels which have an anomalous behavior detecting lower or higher light intensity than the effective one, respectively.
- **pre-processing**, the information extraction process from the image may be affected by multiple errors depending on the applied method. The illumination angle, which

may cause large areas of shadow, and the body irregularities mainly affect the limb fitting algorithms and landmarks recognition. Instead, the point spread function may affect every method.

- **pointing instability**, caused by the probes Attitude Determination and Control Subsystem (ADCS), may induce smearing in the pictures and provide a more imprecise reconstruction.
- **pointing error**, due to payload non-considered misalignment with respect to the body-frame and (e.g., temporary thermal-elastic deformation). Permanent misalignment due to mounting may be accounted for by the pre-launch calibrations.
- **lens distortion** may cause a deformation of the objects being, in general, larger moving far from the boresight. This effect may be strongly reduced by extensive pre-launch calibration to estimate the lens distortion matrix.

### 1.4.2 The Flight Path Control problem

Once the OD process estimated the trajectory of the spacecraft, the deviation with respect to the reference is computed. Generally, the comparison between the reference and the estimated trajectories provides reasonably low errors if the model is well built. Nonetheless, large *a priori* uncertainties from the launcher deployment and/or poorly characterized subsystems (such as the propulsion one), may lead to significant deviations. The FPC task is to clean up the errors at some pre-determined control points (flyby or other critical events), allowing deviations in between. Typically, the trajectory control applies impulsive maneuvers, namely velocity variation of the spacecraft, to maintain the planned path. For the LICIA Cube mission, the only control point defines the flyby condition in the b-plane, so maneuvers have been planned only during the approach phase.

Given a generic trajectory, let us define the set of target variables  $\mathbf{s}$  as the subset of the state, and the function  $\mathbf{s} = \mathbf{f}(\mathbf{x})$  which expresses the value of the target, given the independent control variable  $\mathbf{x} = (x_1, x_2, \dots, x_n)^T$  of the maneuver(s) velocity components. The aimpoint  $\mathbf{q}$  is defined as the target variable values of the reference trajectory. The mathematical problem to be solved [67] is to find the independent control variable  $\mathbf{x}$  such that:

$$\mathbf{f}(\mathbf{x}) - \mathbf{q} \simeq \mathbf{0} \quad (1.13)$$

The convergence of the method is tuned by the minimization of the residual  $\mathbf{r}$ , in a least-square sense:

$$\min_{\mathbf{x} \in \mathbb{R}^n} h(\mathbf{x}) = \frac{1}{2} \sum_{i=1}^m (\mathbf{r}_i(\mathbf{x}))^2 \quad (1.14)$$

The linear Gauss-Newton algorithm computes the iterative correction as:

$$\mathbf{x}_{k+1} = \mathbf{x}_k - (A^T(\mathbf{x}_k)A(\mathbf{x}_k))^{-1} \mathbf{g}(\mathbf{x}_k) \quad (1.15)$$

where  $\mathbf{g}(\mathbf{x}_k) = \nabla h(\mathbf{x}_k) = A^T(\mathbf{x}_k) \mathbf{r}(\mathbf{x}_k)$  and  $A = \partial \mathbf{f}(\mathbf{x}) / \partial \mathbf{x}$  is the partials matrix of the miss-targeting with respect to the control variable. The corrections are applied until the residual of each components is below a tolerance value  $\epsilon_i$ , that verifies:

$$|f_i(\mathbf{x}) - q_i| = |r_i(\mathbf{x})| < \epsilon_i \quad (1.16)$$

Since the matrix  $A$  could be non-full-rank, it should be modified using a complete orthogonal factorization. Furthermore, this method may be non locally convergent if the

problem is sufficiently nonlinear or has large residuals. Hence, it is usually convenient to apply nonlinear methods, such as the Hanson-Krogh algorithm [33]. If the Hessian matrix  $H = \nabla^2 h(\mathbf{x})$  is available, the equation 1.15 can be modified as:

$$\mathbf{x}_{k+1} = \mathbf{x}_k - H^{-1}(\mathbf{x}_k)\mathbf{g}(\mathbf{x}_k) \quad (1.17)$$

being:

$$H_k = A^T(\mathbf{x}_k)A(\mathbf{x}_k) + \sum_{i=1}^m \mathbf{r}_i(\mathbf{x}_k)\nabla^2 \mathbf{r}_i(\mathbf{x}_k) \quad (1.18)$$

The Hanson-Krogh problems aims at the minimization of the cost function defined by an Euclidean norm constrained over a rectangular domain (thrust-region algorithm). Thus, it solves a nonlinear least-square problem for the minimization of the function:

$$\min_{\mathbf{x}_{k+1} \in \mathbb{R}^n} \left\| -(\mathbf{x}_k) + \frac{\partial(\mathbf{x}_k)}{\partial(\mathbf{x})}(\mathbf{x}_k - \mathbf{x}_{k+1}) + \frac{1}{2} \sum_{j=1}^q \mathbf{a}_j \left( (\mathbf{x}_k - \mathbf{x}_{k+1})^T \nabla_j \mathbf{x}_k \right)^2 \right\| \quad (1.19)$$

subject to the constraints  $\mathbf{e}_k - \hat{\nu} \leq \frac{\partial \mathbf{e}(\mathbf{x}_k)}{\partial(\mathbf{x})}(\mathbf{x}_k - \mathbf{x}_{k+1}) \leq \mathbf{e}(\mathbf{x}_k) - \hat{\mu}$  and the bounds  $\mathbf{x}_k \in T \cap S$ , where  $\mathbf{a}_j$  are the vector coefficients of the quadratic model terms,  $\mathbf{e}(\mathbf{x})$  the constraint function,  $\mu$  and  $\nu$  the limits of the domain  $T = \{\mathbf{x} | \mu_j \leq \mathbf{x}_j \leq \nu_j, j = 1, \dots, N\}$ . Hence, the search for the control variable  $\mathbf{x}$  will terminate if the cost function reaches either a value below the given tolerance or a local minimum or its norm experience a change in norm lower than the specified tolerance. Of course, a maximum iteration should be specified as an escape condition to avoid infinite loops.



# Chapter 2

## The LICIACube mission

### Contents

---

<b>2.1</b>	<b>Introduction</b>	<b>15</b>
<b>2.2</b>	<b>The spacecraft</b>	<b>16</b>
2.2.1	Technical specifications	17
<b>2.3</b>	<b>Science objectives</b>	<b>18</b>
<b>2.4</b>	<b>Navigation objectives</b>	<b>19</b>
<b>2.5</b>	<b>Trajectory design</b>	<b>20</b>
2.5.1	B-plane definition	20
2.5.2	Procedure	21
2.5.3	Orbital maneuvers	22
2.5.4	Reference trajectory	24
<b>2.6</b>	<b>Mission timeline</b>	<b>25</b>
2.6.1	Tracking schedule	25
2.6.2	Optical navigation schedule	27
2.6.3	Maneuvers schedule	29
2.6.4	Data Cut-Offs	30
2.6.5	Attitude	31

---

### 2.1 Introduction

The LICIACube mission is an Italian Space Agency (ASI) project in support of the DART mission. It will be the first full-Italian mission in deep space. The probe has been designed and manufactured by the Italian space company Argotec, with the support of the Mission Analysis (MA) team of Polytecnic of Milan (POLIMI) and OD team of University of Bologna (UNIBO) under the scientific lead of the Istituto Nazionale di Astrofisica (INAF) science team. In addition, a science team is in charge of the impact simulation to generate predictions of the ejecta plume and the crater to prepare the in-situ images acquisition and process the data collected during the mission. The scientific team is composed of people from different institutions to collect all the required expertise, in particular from the INAF astronomic observatories of Padua, Trieste, and Capodimonte, the Institute of Astrophysics and Space Planetology, the Institute of Applied Physics "Nello Carrara" of the National Research Council, and the Parthenope University. The mission objectives and the advances in the design of the S/C platform and the trajectory have been shared

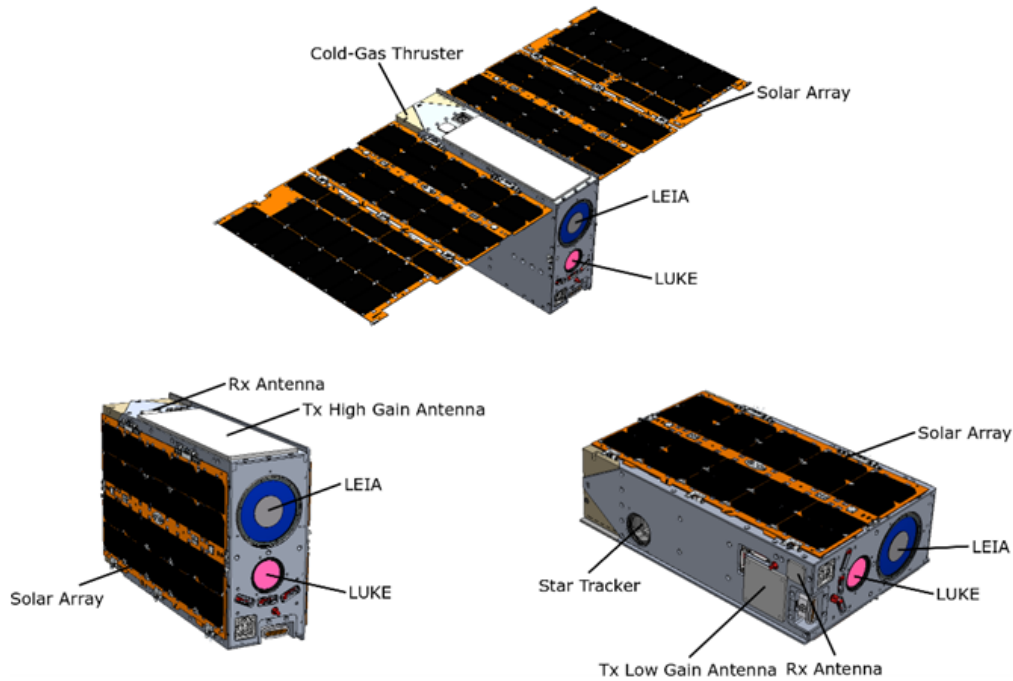


Figure 2.1: LICIAcUBE 3D view, deployed (upper) and stowed (lower). Courtesy of Argotec.

with the larger scientific community represented by the DART investigation team, which groups all the scientists interested in the analysis of the DART and LICIAcUBE results.

LICIAcUBE takes advantage of the DART trajectory to cruise to the Didymos system onboard a piggyback dispenser. A few days before the planned DART impact, the LICIAcUBE will be released, starting its independent navigation toward the asteroids. Its primary goal is to testify the DART impact on Dimorphos, taking images of the impact and the generated ejecta during a single flyby of the system. Thanks to this CubeSat, it will also be possible to obtain some images of the Dimorphos non-impacted hemisphere well in advance with respect to future observations carried by the Hera mission. The whole set of the collected data is expected to be of critical importance to contribute to the deflection effects assessment, otherwise only supported by Earth-based and DART pre-impact observations.

## 2.2 The spacecraft

The LICIAcUBE probe is a 6U CubeSat composed of a central cuboid (main body) and two foldable Solar Array Panels. Once released, the panels irreversibly deploy using pyro-bolts which activate the extension mechanism. The S/C is equipped with an improved ADCS based on the heritage of ArgoMoon [21], an high-performance Propulsion System (PS) and a Star Tracker. The core of the scientific payload is composed of two optical cameras mounted in the front panel (figure 2.1): the narrow field LICIAcUBE Explorer Imaging for Asteroid (LEIA) and the wide field LICIAcUBE Unit Key Explorer (LUKE), named after Star Wars' twins, recalling the meaning of the Didymos target name.

### 2.2.1 Technical specifications

In the following are collected the technical data of the LICIACube S/C of primary interest for this dissertation work.

**Structure** The LICIACube probe is a 6U CubeSat, with a central body roughly  $30 \times 20 \times 10$  cm (a more detailed model is available in table 3.10) and extensible solar panels. The wet weight at the launch is 12.98 kg.

**Telecommunication** LICIACube is equipped with an Iris radio [24] to exchange data with the G/S in deep space X-band, the same model of MarCOs (with software updated to version 2.2). The same radio is capable of coherently transpond X-band Doppler and ranging using the deep space standard protocols supported by the Deep Space Network (DSN). The transmission is performed by two sets of low gain patched antennas (figure 2.1): one on the top side (the normal to the solar arrays) includes a receiving and a higher gain transmitting antennas, while the set on the bottom face is composed of one receiving and one lower gain transmitting antennas. The table 2.1 shows the patched antennas gains.

Table 2.1: LICIACube antenna parameters.

Type	Communication	Side	Gain
Patched	Tx	Top	22 dB
Patched	Rx	Top	6 dB
Patched	Tx	Bottom	12 dB
Patched	Rx	Bottom	6 dB

Moreover, the transponder has been tested to characterize the group delays required to apply the correct range bias. The measured values are reported in table 2.2 for the transponder only, instead the measured antenna delay is below  $\sim 0.9$  ns. Therefore, a conservative value of 15 m is used for the range bias, considering that the tested value of about 9.3 m does not account for harnessing.

Table 2.2: LICIACube measured group delay.

SSPA port	LNA port	Measured value	Variation
J6	J3	6897.3 ns	$\sim \pm 30$ ns
J5	J3	6899.8 ns	
J4	J3	6900.4 ns	
J4	J4	6894.8 ns	

**Payload** The payload of LICIACube is represented by two optical cameras for the collection of the science images during the Closest Approach (C/A). The primary camera, called LEIA is a catadioptric narrow-field camera with a diagonal FOV of  $\pm 2.06^\circ$ , while the secondary, LUKE is a Gecko imager with an RGB Bayer pattern filter, with diagonal FOV of  $\pm 5.00^\circ$ . The cameras technical specifications are listed in table 2.3.

Based on the different FOV and resolution, the usage of the cameras will be different also depending on the phase of the mission. For the scientific observations, the two cameras have different purposes:

Table 2.3: LICIAcUBE cameras parameters [42].

Name	Focal length ( <i>mm</i> )	FOV ( $^{\circ}$ )	Sensor	Sensor's size (px)	Color filter
LEIA	222.45	$\pm 2.06$	CMOS CMV4000	$2048 \times 2048$	Panchromatic (400-900 nm)
LUKE	70.5	$\pm 5.00$	CMOS CMV2000	$2048 \times 1088$	Bayer filter

- **LEIA:** will acquire images from the final approach phase to the system leaving phase, accomplishing multiple requirements;
- **LUKE:** will acquire during the proximity pass of Dimorphos, providing a wider observation thanks to its larger FOV. Moreover, applying different filters may provide additional information about surface properties.

In addition to its scientific tasks, LEIA imager will also serve NAV purposes. In fact, during the 10 days of the system approach, multiple pictures will be acquired pointing to the Didymos system to support the trajectory reconstruction and possibly decrease the probe-to-asteroid relative uncertainty. Furthermore, in the last phase of the approach, some of the LEIA acquisitions will be used by the autonomous imaging and tracking subsystem, inherited from ArgoMoon [22], to support pointing adjustments. After the identification and locking of the asteroid, 200s before the scheduled C/A, the imaging system will keep tracking the target to maintain it in the center of the camera FOV.

**Propulsion system** The LICIAcUBE ADCS relies on a star tracker for attitude determination and stabilizes the spacecraft using the three-axis Reaction Wheel (RW) assembly mounted onboard. For the Orbital Maneuvers (OMs) and the RWs desaturation, the probe mounts a VaCCO monopropellant propulsion system with R-236fa inert fluid. It is similar to the one carried by two MarCOs spacecraft: due to the failure experienced by this latter, particular attention is paid to the calibration and robustness analyses concerning the maneuvers. The LICIAcUBE propulsion system is composed of a propellant tank, a plenum, and six 25mN thrusters: two axial used for the OM main  $\Delta V$ , and a set of four for the attitude control. It is worth noting that the attitude control thrusters are not planar in the rear face; hence some parasitic thrust is also generated during the RWs desaturation maneuvers or during OMs, to maintain the pointing. The embarked fuel (1.236 kg) has a specific impulse of about 40 seconds and can provide a total thrust of 37 m/sec.

## 2.3 Science objectives

The LICIAcUBE opportunity to witness the DART impact with a short delay will represent a unique chance for a detailed characterization of the collision effects. In particular, the information provided by images acquired right after the DART impact will allow retrieving detailed measurements of the evolution of the ejecta plume produced by the impact. It will let us characterize the effect of the collision and make hypotheses about the internal structure and the formation of such celestial bodies. The scientific objectives of the LICIAcUBE mission, negotiated with the DART investigation team, have been formalized below [23]:

**RQ2200.000 Testify DART impact:** Confirm DART impact on Dimorphos by imaging the impact area during the latest part of the approach phase.

**RQ2200.001 DART impact ejecta plume imaging:** Obtain multiple (at least 3) images of the ejecta plume taken over a span of time and phase angle, that, with reasonable expectations concerning the ejecta mass and particle size distribution, can potentially:

- i Allow measurement of the motion of the slow ( $<5$  m/s) ejecta: this requirement aims to acquire images at a spatial scale better than 5 m/px, which gives the chance to distinguish the movements of the slowest particles of the plume by the sequence of images.
- ii Allow estimation of the plume structure, measuring the evolution of the dust distribution.

**RQ2200.002 DART impact crater imaging:** Obtain multiple (at least 3) images of the DART impact site with a sufficient resolution to allow measurements of the size and morphology of the crater. These images will be taken sufficiently late after the impact that the plume can be reasonably expected to have cleared;

**RQ2200.003 Dimorphos non-impacted hemisphere imaging:** Obtain multiple (at least 3) images of Dimorphos showing the non-impact hemisphere, hence increasing the accuracy of the shape and volume determination.

It is worth noting that the original RQ2200.002 requirement also specified the minimum resolution for crater images of 5m/px. Although, MA demonstrated the incompatibility between RQ2200.001 and RQ2200.002 concerning the delay time required for the probe to the flyby of the system [23]. Based on the higher priority of imaging the impact plume rather than the crater, the RQ2200.001 is maintained while RQ2200.002 has been modified, removing the resolution specification.

## 2.4 Navigation objectives

Starting from the high-level scientific requirements, a suitable middle-level of MA requirements have been set [11]. Those are mainly related to the nominal trajectory and the flyby condition to let a full development of the ejecta plume and avoid the saturation of the RWs' speed during the high-rate flyby pointing to Dimorphos. This led to the top level of NAV requirements which summarizes all the other constraints applicable for the flyby phase. The NAV requirements have been formalized in the following list and are valid up to the flyby:

**RQ4100.001 LICIACube trajectory for ejecta plume imaging:** For collecting Payload (PL)1 (LEIA) optical images of the low-speed ejecta particles and the probe safety, the predicted radial distance comprehensive of the uncertainty ( $3\sigma$ ) of the LICIACube trajectory relative to Dimorphos's center of mass at the closest approach, at the time of the last update of the onboard ephemeris and command sequences before the closest approach, shall be larger than 39.9 km and less than 80 km.

**RQ4100.002 Dimorphos pointing accuracy:** To ensure the capability of the autonomous optical pointing system of locking the Dimorphos target in the control loop, the predicted Dimorphos pointing uncertainty due to the LICIAcUBE position uncertainty relative to Dimorphos' center of mass at the PL1 (LEIA) locking time, occurring 200 sec before the closets approach, at the time of the last update of the onboard ephemeris and command sequences before the closest approach, shall be lower than 50.8 mrad, corresponding to half FOV of the PL1 (LEIA) with a confidence higher than 99%.

**RQ4100.003 DSN pointing accuracy:** To ensure the capability of establishing a telecom link with the DSN, the predicted LICIAcUBE pointing uncertainty, due to position uncertainty, relative to Earth's center of mass at each time a ground station contact is scheduled, computed with a data cutoff not closer to 24 hours to the link establishment, shall be lower than 0.30 mrad [38] with a confidence higher than 99%.

**RQ4100.004 LICIAcUBE Closest Approach predicted delay time:** To ensure low speed ejecta observability, the LICIAcUBE flyby epoch relative to Dimorphos shall occur not later than 200 sec after the DART planned impact on Dimorphos with a confidence higher than 99%.

**RQ4100.005 Sun Phase Angle at Closest Approach:** To ensure the correct Sun Phase Angle (SPA), the predicted uncertainty ( $3\sigma$ ) of the LICIAcUBE trajectory relative to Dimorphos' center of mass, shall lead to a SPA between 45 deg and 70 deg for the closest approach epoch, at the time of the last update of the onboard ephemeris and command sequences before the closest approach.

Additional constraints are also demanded during the post-flyby, having the unique goal of downloading the previous-acquired data. Therefore, the only applicable constrain is the DSN pointing accuracy demanded by RQ4100.003.

## 2.5 Trajectory design

The nominal trajectory (also referred to as baseline or reference) has been designed by the joint efforts of MA, OD and science teams. This represent the *ideal* trajectory LICIAcUBE should follow during its cruise starting from the release from DART. This trajectory is designed to fulfill the scientific objectives, providing evidence of those which cannot be achieved due to dynamic or platform limitations. Although the baseline analysis has already been described in [11], a brief hint of the procedure used is reported in paragraph 2.5.2 to highlight the contribution of the OD to this purpose. Before doing that, the B-plane should be introduced, a definition that will be useful hereafter.

### 2.5.1 B-plane definition

For the analysis of the encounter conditions with respect to a body, it is convenient to use the B-plane (Body Plane) [57]. Being normal to the inbound asymptotic velocity of the spacecraft with respect to the target body, it allows for linear analysis of the encounter before the probe trajectory is significantly affected by the flyby body [26]. In figure 2.2 is represented the B-plane with all the applicable parameters. This is defined as a plane normal to the relative asymptotic velocity at infinity,  $\hat{v}_\infty$ , which passes from the center of the flyby planet. The vector  $\hat{S}$  is collinear to  $\hat{v}_\infty$ . The vector  $\hat{B}$  lies on the B-plane and points from the origin to the incoming asymptote projection on the B-plane (called

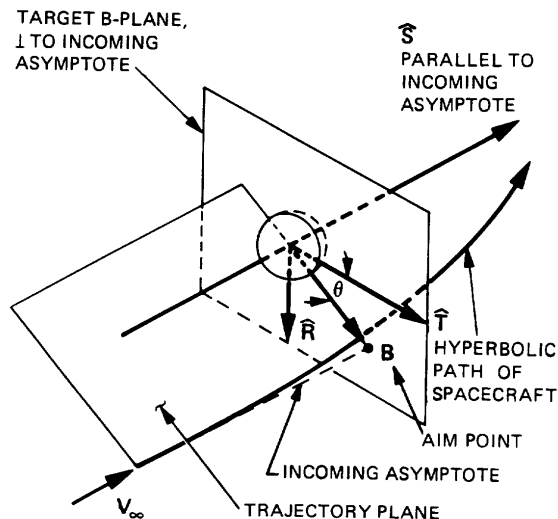


Figure 2.2: Definition of target B-plane coordinates. Source: [57]

aimpoint). This vector is usually given in its B-plane components,  $\hat{\mathbf{B}} \cdot \hat{\mathbf{R}}$  and  $\hat{\mathbf{B}} \cdot \hat{\mathbf{T}}$  where the axes  $\hat{\mathbf{T}}$  and  $\hat{\mathbf{R}}$  forms an orthonormal set with  $\hat{\mathbf{v}}_\infty$ . These two vectors are arbitrarily defined, although  $\hat{\mathbf{T}}$  is usually defined to be parallel to a fundamental plane, such as the ecliptic or the planet's equator. Finally, the clock angle  $\theta$  is the counter-clockwise angle from  $\hat{\mathbf{T}}$  to  $\hat{\mathbf{B}}$ . It is also possible to define the Time of Closest Approach (TCA) as the epoch of the encounter and the Linearized Time of Flight (LTOF), i.e. the correspondent epoch of TCA for the rectilinear approach trajectory along the incoming asymptote [36]. Therefore, for a massless body, the LTOF and the TCA would be coincident. This approximation holds in the case of LICIACube encounter of Dimorphos.

In general,  $\mathbf{v}_\infty$  is intended to be the velocity of the probe far enough away from the central body such that the trajectory becomes almost coincident with the incoming asymptote. Although for most of the planets and moons  $\mathbf{v}_\infty$  is assumed to be the velocity at the boundary of the sphere of influence of the flyby body, a practical consideration will arise in the following, since the tiny mass of the Didymos system has a negligible effect on the deflection of the LICIACube probe, the aimpoint can be considered almost coincident to the trajectory intersection of the B-plane. Note also that, to this work aim,  $\hat{\mathbf{T}}$  is chosen to lie on the ecliptic.

### 2.5.2 Procedure

At first, the C/A aimpoint is set based on the mission constraints, namely the distance from Dimorphos ( $B \simeq R$ ), the B-plane clock angle ( $\theta$ ), and the delay time from the DART impact. Thus, the initial state of LICIACube at deployment (that is the same as DART) and the final conditions required at the aimpoint constrain the reference trajectory. The problem is not fully defined since only the position is constrained at the C/A<sup>1</sup>. Furthermore, additional degrees of freedom are introduced by the release direction and the maneuvers scheduled between the end-points to target the nominal aimpoint.

The adopted iterative procedure for the trajectory design can be summarized as follows:

1. the MA team computes a reference trajectory based on the initial position provided

<sup>1</sup>Fixing the delay time will also have minor effects in constraining the C/A velocity, but it mainly defines the epoch of the C/A.

by the DART trajectory at release, the LICIAcUBE aimpoint at B-plane, and the maneuvers schedule. Additional degrees of freedom are solved by minimizing the propellant mass used.

2. the OD team performs an analysis of the reference trajectory, propagating the uncertainty of the probe and verifying the compliance to all the requirements. Those requirements which are not met are reported, with possible mitigation actions, to the scientific team.
3. the scientific team checks the outcome of the OD, proposing a modification to the reference trajectory whenever required.

### 2.5.3 Orbital maneuvers

The maneuvers scheduled during the mission have different goals:

- to test the propulsion system and characterize its performances;
- to target the C/A aimpoint of the nominal trajectory;
- to correct possible deviations of the trajectory from the nominal one during operations.

Based on the aim of each maneuver, different constraints could be identified for any of them. It is clear that the propulsion system test maneuver should be the first one to be performed, such as having a propulsion system characterization as early as possible. On the other hand, placing the targeting and the corrective maneuvers has been based on the cost-sensitivity function provided by the K-inverse matrix approach.

Defining  $K$  as the matrix of the partials derivatives of the aimpoint (in the form of the b-plane state coordinates) with respect to the spacecraft velocity

$$K = \begin{bmatrix} \frac{\partial B \cdot R(t_{CA})}{\partial DX(t)} & \frac{\partial B \cdot R(t_{CA})}{\partial DY(t)} & \frac{\partial B \cdot R(t_{CA})}{\partial DZ(t)} \\ \frac{\partial B \cdot T(t_{CA})}{\partial DX(t)} & \frac{\partial B \cdot T(t_{CA})}{\partial DY(t)} & \frac{\partial B \cdot T(t_{CA})}{\partial DZ(t)} \\ \frac{\partial LTOF(t_{CA})}{\partial DX(t)} & \frac{\partial LTOF(t_{CA})}{\partial DY(t)} & \frac{\partial LTOF(t_{CA})}{\partial DZ(t)} \end{bmatrix} \quad (2.1)$$

under linearization assumption, the variation of the b-plane encounter coordinates given an impulsive maneuver at the epoch  $t_{OM}$  can be computed as:

$$\Delta \mathbf{x}(t_{CA}) = K \cdot \Delta \mathbf{v}(t_{OM}) \quad (2.2)$$

Hence, the maneuver to correct the miss-targeting in aimpoint can be computed as:

$$\Delta \mathbf{v}(t_{OM}) = K^{-1} \cdot \Delta \mathbf{x}(t_{CA}) \quad (2.3)$$

This imply that, for a general deviation  $\Delta \mathbf{x}$  of the aimpoint, the  $\Delta \mathbf{v}$  can be minimized by the minimization of  $\|K^{-1}\|$ , which therefore represents the cost function. Figure 2.3 clearly shows that the cost of the maneuver is minimum at the release and increases over time, with a steeper rate closer to the C/A epoch. More than that, this approach also provides valuable information about disturbance sensitivity. In general, the lower the cost, the larger the effect of a small acceleration on the aimpoint. Thus, at the earlier stages of the mission, the maneuvers cost less but we are also more sensitive to possible imprecision in maneuvers execution. A reasonable model for the maneuver execution error

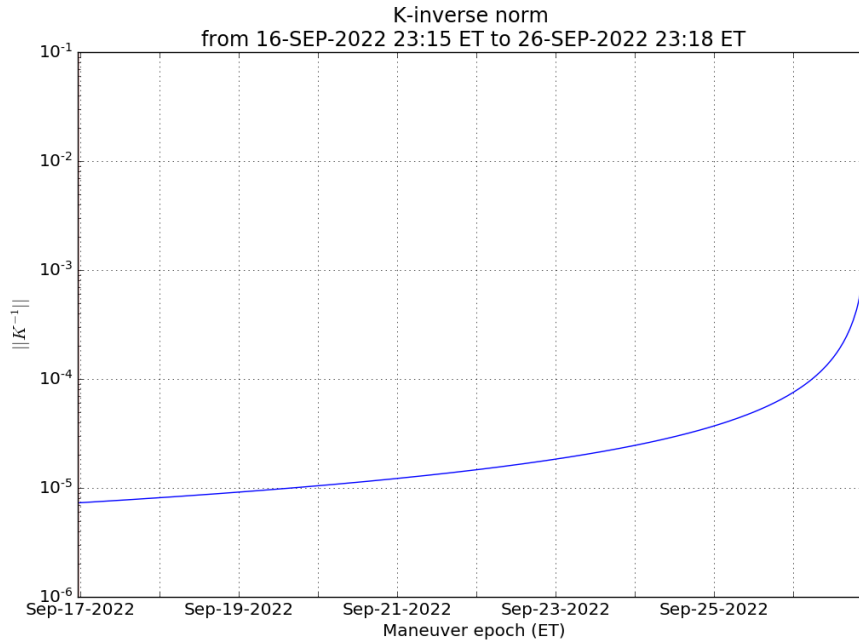


Figure 2.3: LICIACube K-inverse matrix norm as function of the maneuver time.

may include both a fixed and a proportional component (section 4.4). If the model was purely proportional, thus the execution error applied on the equation 2.3 would lead to:

$$\Delta\Delta\mathbf{v}(t_{OM}) = \alpha K^{-1} \cdot \Delta\mathbf{x}(t_{CA}) \quad (2.4)$$

where  $\alpha$  is the proportionality error coefficient. Therefore, the resulting miss-targeting would be:

$$\Delta\Delta\mathbf{x}(t_{CA}) = K \cdot \Delta\Delta\mathbf{v}(t_{OM}) = \alpha K K^{-1} \cdot \Delta\mathbf{x}(t_{CA}) = \alpha \Delta\mathbf{x}(t_{CA}) \quad (2.5)$$

which is independent of the maneuver execution time, as the  $K$  matrix vanished. Conversely, the fixed component contribution is dependent on the execution epoch as the error is always the same, so the earlier the maneuver is performed, the more time its uncertainty acts on the dispersion. This lead to two important conclusions:

- The target maneuver should be placed as earlier as possible, exploiting the lower cost required, although its fixed error component will be integrated over a longer time;
- The correction maneuvers should be placed as close as possible to the C/A in order to have a shorter integration time to the target and thus keep the dispersion low. The larger value of  $\|K^{-1}\|$  does not represent a problem since the correction maneuvers are expected to be small compared to the total available  $\Delta V$ .

The proposed approach drove the maneuvers scheduling baseline and the required processing time. In fact, each of the closed-loop maneuvers<sup>2</sup> shall be computed based on a certain amount of tracking data collected before a fixed epoch called Data Cut-Off (DCO),

<sup>2</sup>A maneuver is considered to be a closed-loop if its *a priori* value should be corrected during the mission based on previous trajectory reconstruction.

which serves as a milestone for the start of the OD computing leading to the maneuver calculation. Despite the allotted time for deep space mission OD reconstruction process is typically in the order of a few days, the very tight LICIAcUBE timeline requires stronger effort, keeping the total amount of OD and maneuver calculation processes closer to 48 hours. Finally, to ensure the reconstruction, the maneuvers are constrained to be placed in the middle of a tracking pass to have sufficient data before and after the maneuver.

After some iterations, the planned maneuvers are:

**propulsion Calibration Maneuver (CAL1)** is a deterministic pre-computed maneuver used to characterize the propulsion system performance. It should be performed in the Earth-radial direction in order to maximize its observability through the Doppler, and it shall have a minimum  $\Delta V$  at least one order larger than its a-posteriori OD uncertainty. Due to time limitations, this cannot be performed in the contingency release case.

**breaking maneuver OM1** is a deterministic and statistical maneuver. Its deterministic value is determined *a priori* to deflect the nominal trajectory and meet the B-plane aimpoint. Its statistical component could be determined during operations to clean any deviation of the estimated trajectory from the reference trajectory. Of course, this will require some computing time during the operations, which implies a minimum separation from CAL1 of at least 24/48 hours. Note that this is not possible for the backup release, and therefore the OM1 is purely deterministic in this case.

**cleanup maneuvers OM2 and OM3** are two purely statistical maneuvers set in the approach to adjust the estimated trajectory, cleaning up the deviation. Being statistical, these are 0-mean. Like the OM1, these maneuvers require some design computation time to be accounted for in the timeline. Due to the tight backup timeline, only OM2 is foreseen.

In addition to proper maneuvers, the deployment acceleration is also included in the maneuvers list, although it is released activated by the compression force of the dispenser springs. Said  $M_{LCC}$  the LICIAcUBE mass,  $M_{DRT}$  the DART one, and the energy of the dispenser springs  $E_{disp}$ , the relative release speed of LICIAcUBE with respect to DART can be computed as:

$$v_r = \sqrt{\frac{E_{disp}}{M_{LCC}}} \quad (2.6)$$

Finally, the inertial  $\Delta V$  acting on LICIAcUBE can be computed by taking the mass scaling of the relative velocity, from the momentum conservation:

$$v_{i,LCC} = \frac{M_{DRT}}{M_{LCC} + M_{DRT}} v_r \quad (2.7)$$

Therefore, considering  $M_{LCC} = 12.98$  kg,  $M_{DRT} = 575$  kg and  $E_{disp} = 18.8 \frac{kg \cdot m^2}{s^2}$  the obtained value for the release is 1.177 m/s. Furthermore, being the dispenser rigidly fixed on the DART structure, the release direction has been optimized by the MA in a restricted range constrained by the DART attitude.

## 2.5.4 Reference trajectory

A reference trajectory was obtained at the end of the mission design loop. This baseline allows a maximization of the scientific return, given the limitations of the dynamical

environment and the S/C capabilities. The reference trajectory data for the nominal release are shown in picture 2.4. In addition, the orbital parameters for the Dimorphos encounter, are reported in table 2.4. It is also worth noting that the asymptotic velocity deflection caused by the Dimorphos flyby is about  $2.02 \cdot 10^{-11}$  degree, so no measurable effect is expected to be observed.

Table 2.4: LICIACube orbital parameters with respect to Dimorphos at the encounter epoch, in Earth Mean Equator at J2000 (EME2000).

Parameter	Value	Units
Distance	51.2	km
Speed	6.1	km/s
$v_\infty$	6.1	km/s
$i$	44.2	deg
$t_{CA}$	26-SEP-2022 23:18:14.2503 ET	
$t_{CA} - T_0$	167.0	sec

## 2.6 Mission timeline

The LICIACube mission timeline has been designed to achieve the scientific objectives, taking into account the platform specifications and the orbit reconstruction capability. The mission schedule starts with the LICIACube release. Two possible deployment epochs have been foreseen for LICIACube: a nominal opportunity is scheduled ten days before the expected DART impact date, whereas a backup chance is planned six days before the impact date. The large time span between the two windows should guarantee enough time to solve any possible release problem. The entire mission is divided into three parts:

- Approach phase: starts from the deployment from the DART piggyback dispenser occurring either ten (nominal) or six (contingency) days before DART scheduled impact. This period is the most complex part from the navigation point of view, where all the maneuvers shall be performed to prepare for the flyby. All the requirements stated in section 2.4 apply to the approach phase.
- Science phase: starts from 20 minutes before to 5 minutes after the predicted C/A epoch. Most of the science data will be acquired and stored onboard during this period while every other activity (maneuvers, optical navigation acquisitions, tracking) is inhibited. The S/C will rely on the autonomous pointing system to maintain the target in the camera FOV during this phase.
- Leaving phase: starts at the end of the previous phase up to the end of the mission. During this part the data acquired in the science phase are download to the Earth, therefore the requirement RQ4100.003 is applicable. The foreseen duration is limited to a maximum of 6 months, but this will be reviewed depending on actual data rate available.

Table 2.5 summarizes the main events.

### 2.6.1 Tracking schedule

In the following, the tracking schedule is presented for the different phases, except for the science one where the tracking is not active. It is worth noting that the assumed passes

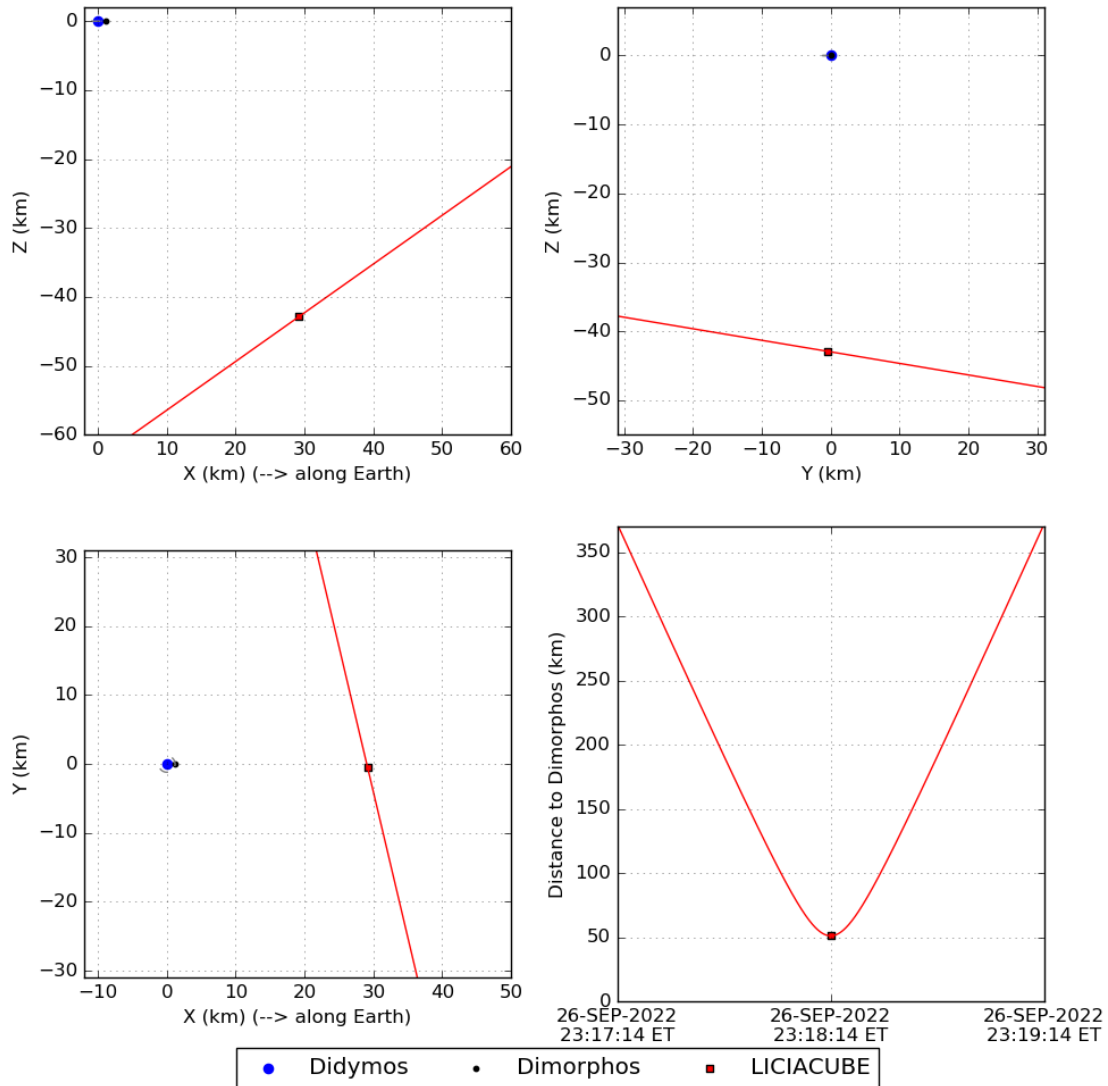


Figure 2.4: LICIACube trajectory in the Dimorphos orbital plane.  $+Z$  is the pole of Didymos primary,  $+X$  is the normal to  $+Z$ , toward Earth.

Table 2.5: LICIACube mission main events.

Event	Date	Epoch wrt $T_0$
Release (nominal)	16-SEP-2022 23:15:27.2931 ET	$T_0 - 10$ days
Release (backup)	20-SEP-2022 23:15:27.2931 ET	$T_0 - 6$ days
Start of Science Phase	26-SEP-2022 22:55:27.2931 ET	$T_0 - 20$ min
DART impact on Dimorphos	26-SEP-2022 23:15:27.2931 ET	$T_0$
LICIACube C/A to Dimorphos	26-SEP-2022 23:18:14.2503 ET	$T_0 + 167$ sec
End of Science Phase	26-SEP-2022 23:23:14.2503 ET	$T_0 + 467$ sec
End of Mission	26-MAR-2023 23:15:27.2931 ET	$T_0 + 6$ months

yet account for the extra time required by the DSN, thus the pass is split into:

- ground station setup, considered to its maximum value of 30 min;
- carrier locking assumed to its maximum value of 15 min, although the sweep typically lasts no more than 5 minutes;
- useful tracking duration of 90 min;
- teardown time is not included as it is usually instantaneous at the end of the pass.

**Approach phase** Although the approaching timeline slightly differs for the maneuvers placing and possible optical acquisition scheduling depending on the release case (nominal or contingency), the radio-tracking observables timeline is fixed due to the antennas' availability constraints. The DSN dedicated a single antenna to the DART and LICIACube missions, therefore the timeline has to be negotiated with the DART team. Due to the higher priority of the DART mission to downlink acquired data (DART mission will cease with the impact and all data shall be downloaded before that date), LICIACube required the minimum ground station time to ensure a safe NAV with adequate margins. This, combined with the power budget limitation of LICIACube, results in two passes per day, with a total antenna time of 4h30min, equally distributed. Due to the power budget limitations, the probe needs a minimum of 3 hours to guarantee a full charge between two passes. Hence, the passes are arranged in the timeline with a constant daily frequency but separated by different time spans (about 12 and 6 hours) because of DART scheduled activities. Few adjustments to this general distribution have been required, namely:

- the delay of 15 minutes for the first tracking pass after each release opportunity to account for deployment operations;
- the last tracking pass before the flyby, anticipated of about 9 hours to be compliant with the DART request of clearance for the last 12 hours of the mission, to download data at the fastest data rate.

A full view of the approach phase timelines is shown in figures 2.5 and 2.6, for nominal and backup releases, respectively.

**Leaving phase** The ground station time availability for the leaving phase is limited to 2h15min per day, starting 8h after the flyby. Although NAV requirements are much less stringent in this phase, the need for a download connection led to the demand for daily coverage.

### 2.6.2 Optical navigation schedule

The availability of Optical Navigation (OPNAV) is strongly subjected to the time required for the effective data rate and the requirement, from the science team, to acquire payloads calibration images. The current proposal for the OPNAV images is to use the primary payload LEIA to acquire pictures of the Didymos system. The proposed schedule is to have two images (three acquisitions per image, at different shutter times) per day, separated by about 12 hours, starting from 7 up to 3 days before the flyby.

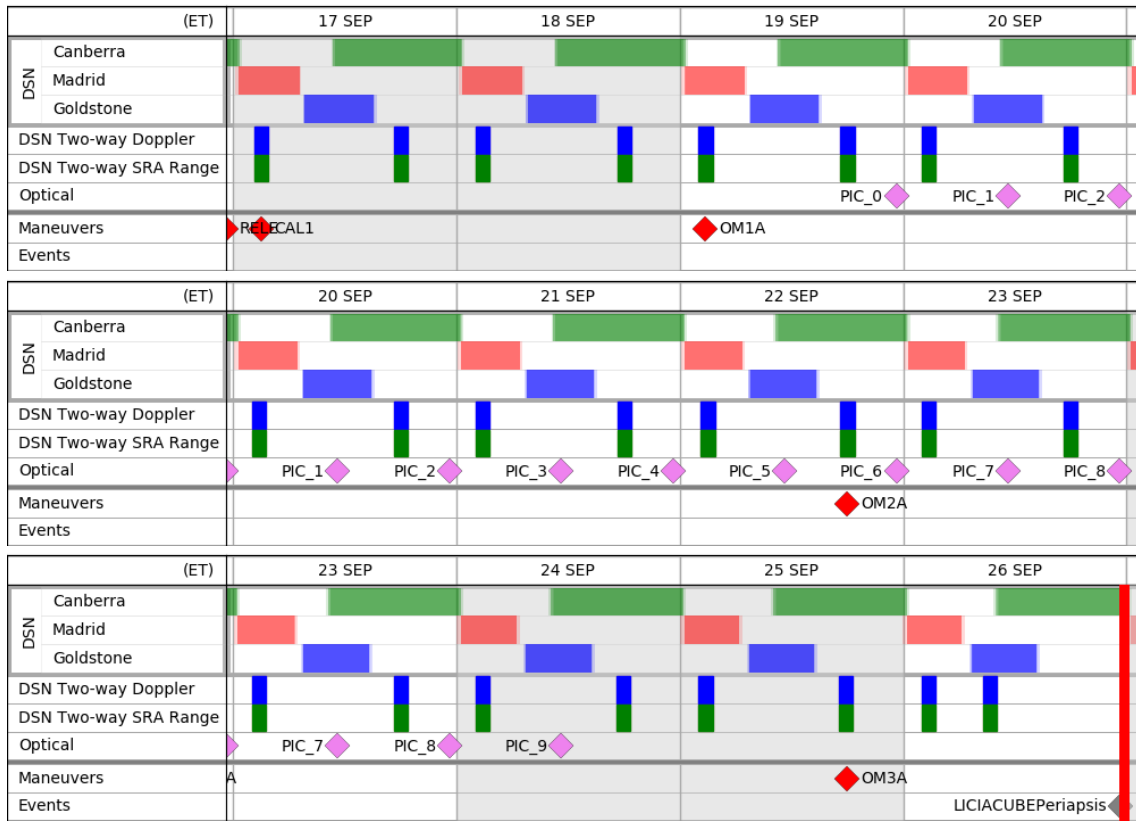


Figure 2.5: LICIAcUBE approach phase timeline for nominal release.

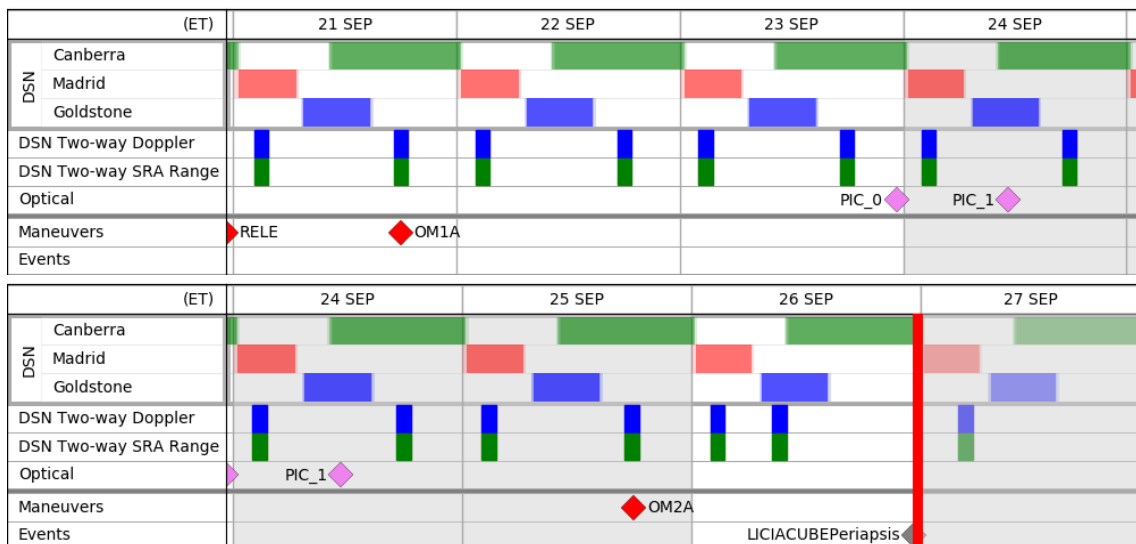


Figure 2.6: LICIAcUBE approach phase timeline for contingency release.

### 2.6.3 Maneuvers schedule

Based on the maneuvers list and the need for coverage during their execution, the maneuvers were placed following the hereafter conditions, for the nominal release:

- the propulsion Calibration Maneuver (CAL1) is set in the middle of the first tracking pass for the nominal release condition;
- the aimpoint targeting maneuver (OM1), also referred to as braking since it decreases the speed relative to the asteroid, is placed in the middle of the fifth tracking pass (OM1A), about 48 hours after the CM1, to allow for the OD run and the closed-loop maneuver calculation;
- the first cleanup maneuver (OM2) is placed in the middle of the last tracking pass (OM2A) before the Delivery DCO, to allow for its reconstruction at the last ephemeris update onboard the probe prior to the C/A;
- the second and last cleanup maneuver (OM3) set in the third-to-last tracking pass (OM3A) before the C/A, to reset possible deviation from the reference trajectory computed at the delivery DCO.

In addition, all the closed-loop maneuvers have a backup option (OM1B, OM2B, OM3B) in the passes following the nominal slot to ensure each maneuver will be executed. Of course, more work is required during the operations to generate two different maneuvers for the nominal and backup options.

On the other hand, due to the tighter timeline in the backup release case, the maneuver schedule has been modified as follows:

- the propulsion Calibration Maneuver is not foreseen;
- the OM1A, is performed as open-loop maneuver, in the middle of the second pass;
- the first and only cleanup maneuver (OM2) is placed in the middle of the third-to-last tracking pass (OM2A), with a backup in the second-to-last pass (OM2B).

The final maneuvers schedules are reported in tables 2.6 and 2.7 for nominal and backup releases, respectively.

Table 2.6: LICIACube maneuvers schedule for nominal release. Right ascension and declination are in EMO2000.

	<b>Time</b>	<b>DV</b> (m/s)	<b>RA</b> (deg)	<b>DEC</b> (deg)
<b>RELE</b>	16-SEP-2022 23:15:27.2931 ET	1.1769	83.9381	-64.4202
<b>CAL1</b>	17-SEP-2022 03:00:27.2931 ET	0.0020	216.2084	46.1048
<b>OM1A</b>	19-SEP-2022 02:45:27.2931 ET	1.7251	148.8277	53.2146
<b>OM2A</b>	22-SEP-2022 18:00:27.2931 ET	0.0	-	-
<b>OM3A</b>	25-SEP-2022 18:00:27.2931 ET	0.0	-	-

Table 2.7: LICIAcUBE maneuvers schedule for backup release. Right ascension and declination are in EMO2000.

	<b>Time</b>	<b>DV</b> (m/s)	<b>RA</b> (deg)	<b>DEC</b> (deg)
<b>RELE</b>	20-SEP-2022 23:15:27.2931 ET	1.1769	86.1511	-65.8234
<b>OM1A</b>	21-SEP-2022 18:00:27.2931 ET	2.0365	137.9787	35.3964
<b>OM2A</b>	25-SEP-2022 18:00:27.2931 ET	0.0	-	-

#### 2.6.4 Data Cut-Offs

In the OD process, the DCO is used as milestones to stop the data gathering for the beginning of a reconstruction process. Of course, data acquisition may continue as a parallel process, but new measurements will not be included in the released solution. Thus, it is essential to select relevant epochs at which the deliveries are required from the OD and, for each one, choose a suitable DCO which allows enough data to perform the reconstruction but also to leave time to obtain and validate the results. In principle, the events requiring reconstruction of the probe's trajectory are:

- maneuvers, for the computation of the  $\Delta\mathbf{v}$  required to correct the orbit;
- science observation, for the update of the foreseen events epoch (e.g. flyby) and the pointing direction to collect relevant data;
- periodical S/C-Earth pointing, to guarantee the contact with the ground segment.

The very compressed timeline of LICIAcUBE requires a major effort for the approach phase. For this reason, the first ten days of the mission present a limited computation time, from one to two days for the complete trajectory reconstruction and maneuver calculation processes. This time span is not excessively tight, although personnel turns and daily working hours could be extended for these ten days in case of off-nominal flight conditions. As expected, the leaving phase does not represent a critical phase due to loosen requirements, allowing a more relaxed timeline and thus a more conservative computation time allotted. A full list of the approach phase DCOs is presented in tables 2.8 and 2.9 for nominal and contingency release, respectively.

Table 2.8: LICIAcUBE Data Cut-Offs schedule during approach phase, nominal release case.

	<b>Execution</b>	<b>Delivery</b>	<b>DCO</b>	<b>Delivery-DCO</b>
<b>OM1</b>	19-SEP-2022 02:45:27.2931 ET	19-SEP-2022 01:45 UTC	17-SEP-2022 18:50 UTC	26h 30min
<b>OM2</b>	22-SEP-2022 18:00:27.2931 ET	22-SEP-2022 17:00 UTC	20-SEP-2022 18:50 UTC	46h 10min
<b>OM3</b>	25-SEP-2022 18:00:27.2931 ET	25-SEP-2022 16:45 UTC	23-SEP-2022 18:50 UTC	45h55min
<b>Delivery</b>	-	26-SEP-2022 08:15 UTC	23-SEP-2022 18:50 UTC	61h25min

As one may notice, the DCOs have been placed well in advance with respect to the maneuvers, to account for the complete maneuver design loop. The delivery DCO represents

Table 2.9: LICIACube Data Cut-Offs schedule during approach phase, backup release case.

	<b>Execution</b>	<b>Delivery</b>	<b>DCO</b>	<b>Delivery-DCO</b>
<b>OM2</b>	25-SEP-2022 18:00:27.2931 ET	25-SEP-2022 16:45 UTC	23-SEP-2022 18:50 UTC	45h55min
<b>Delivery</b>	-	26-SEP-2022 08:15 UTC	24-SEP-2022 03:50 UTC	52h25min

the final assessment of the trajectory before the encounter and shall be used to update the onboard pointing schedule to perform a correct imaging sequence. For the contingency release case, the delivery DCO is shifted to include an additional tracking pass compared to the nominal release schedule and tear down the uncertainty without compromising the reconstruction allotted time, still greater than two days.

### 2.6.5 Attitude

The probe's attitude in operations will follow the mission schedule. In particular, during tracking passes, the higher gain antenna will point to the Earth, while during battery recharge the solar panels will point to the Sun, with only a few exceptions due to calibrations of instruments and functionality tests not reported in figures 2.5 or 2.6. Although pointing profiles are not yet available, a constant Sun-pointing attitude has been assumed, providing a good guess of the predicted accelerations. In fact, the OD uses the attitude only for the calculation of the SRP, and the expected pointing will be toward the Sun for about twenty hours per day.



# Chapter 3

## Navigation model

### Contents

---

<b>3.1</b>	<b>Rotational models</b>	<b>33</b>
3.1.1	Didymos primary	33
3.1.2	Didymos secondary	34
<b>3.2</b>	<b>Didymos dynamical model</b>	<b>35</b>
3.2.1	Didymos system	35
3.2.2	Dimorphos	36
<b>3.3</b>	<b>Shape models</b>	<b>38</b>
<b>3.4</b>	<b>Gravitational models</b>	<b>38</b>
3.4.1	Didymos primary	39
3.4.2	Didymos secondary	40
<b>3.5</b>	<b>LICIACube spacecraft models</b>	<b>41</b>
3.5.1	Initial conditions	41
3.5.2	Forces	42
3.5.3	Shape	43
3.5.4	Solar Radiation Pressure	44
3.5.5	Maneuvers	45
3.5.6	Stochastics	45

---

### 3.1 Rotational models

The rotational model of Didymos primary and secondary influence the gravitational accelerations acting both on Dimorphos and on the S/C. The model implemented and described in the following paragraphs has been adapted from the Design Reference Asteroid (DRA) rev 3.11 [18].

#### 3.1.1 Didymos primary

The pole orientation of Didymos with respect to the Earth Mean Orbit at J2000 (EMO2000) is given in spherical coordinates described by the right ascension  $\alpha$  and declination  $\delta$ , as a function of the time  $t$  past the reference epoch  $t_0 = J2000$  (January, 1<sup>st</sup>, 2000 12:00 ET):

$$\alpha = \alpha_0 + \alpha_1(t - t_0) \tag{3.1}$$

$$\delta = \delta_0 + \delta_1(t - t_0) \quad (3.2)$$

The orientation of the prime meridian with respect to the node is also described by the angle  $w$  as a linear function of time past the reference epoch J2000.

$$w = w_0 + w_1(t - t_0) \quad (3.3)$$

The latest numerical values for the Didymos rotational model are collected in table 3.1 with their correspondent uncertainties [56].

Table 3.1: Rotational model of Didymos primary: *a priori* values and uncertainties. The reference frame is EMO2000. The reference time is J2000.

Parameter	Value	Units	Comments
$\alpha_0$	$320.6 \pm 13.7$	deg	Pole solution.
$\alpha_1$	0.0	deg/century	Not measured, assumed zero.
$\delta_0$	$-78.6 \pm 1.8$	deg	Pole solution.
$\delta_1$	0.0	deg/century	Not measured, assumed zero.
$w_0$	0.0	deg	Prime meridian, assumed zero.
$w_1$	$159.29 \pm 0.007$	deg/h	Computed from rotation period.

### 3.1.2 Didymos secondary

Data about the Dimorphos rotational state are mainly still unknown. Nonetheless, within the known population of NEA binary systems, the secondary almost always rotates synchronously, namely, its rotational period is synchronized to the mutual orbital period. Therefore, the same rotational model can be assumed for the Didymos system.

The adopted rotational state of Didymos secondary consists of three subsequent steps: first, Dimorphos is integrated using a dynamical body-fixed frame generated assuming a synchronous rotation around the primary, which implies that the pole of Dimorphos is perpendicular to its orbital plane about the primary. Finally, the dynamical frame is fitted through a least-square fit to a kinematic model, where the pole orientation of Dimorphos is given - as for Didymos primary - in spherical coordinates described by the right ascension  $\alpha$  and declination  $\delta$ , as a function of the time  $t$  past the reference epoch  $t_0 = J2000$  (January, 1<sup>st</sup>, 2000 12:00 ET):

$$\alpha = \alpha_0 + \alpha_1(t - t_0) \quad (3.4)$$

$$\delta = \delta_0 + \delta_1(t - t_0) \quad (3.5)$$

The orientation of the prime meridian with respect to the node is described by the angle  $w$  as a linear function of time past the reference epoch J2000. In addition, it is considered a libration motion with amplitude  $w_a$  and period equal to the orbital one, which may be present as natural effect and/or induced by the DART impact:

$$w = w_0 + w_1(t - t_0) + w_a \sin(\omega t + \varphi) \quad (3.6)$$

The latest numerical values for the Dimorphos rotational model are collected in 3.2 with their correspondent uncertainties. Note that all the values except the libration ones are equal to table 3.1 as a consequence of the above assumptions.

Table 3.2: Rotational model of Didymos secondary: *a priori* values and uncertainties. The reference frame is EMO2000. The reference time is J2000.

Parameter	Value	Units	Comments
$\alpha_0$	$320.6 \pm 13.7$	deg	Assumed from primary.
$\alpha_1$	0.0	deg/century	Assumed from primary.
$\delta_0$	$-78.6 \pm 1.8$	deg	Assumed from primary.
$\delta_1$	0.0	deg/century	Assumed from primary.
$w_0$	0.0	deg	Assumed from primary.
$w_1$	$159.29 \pm 0.007$	deg/h	Assumed from primary.
$w_a$	0.0	deg	Assumed zero.
$\omega$	$30.20 \pm 7e - 6$	deg/h	From input average orbital period.
$\varphi$	6.71	deg	Fitted to a dynamical synchronous model.

## 3.2 Didymos dynamical model

In order to perform a realistic OD assessment, all of the LICIACube, Didymos system and Dimorphos trajectory should be modeled and estimated together. Nevertheless, their dynamics can be decoupled as follows:

1. the Didymos Barycenter motion with respect to the the Solar System Barycenter;
2. the relative orbit of Dimorphos about the Didymos Barycenter;
3. the trajectory of the S/C, influenced by the Didymos System.

Therefore, it is necessary to provide an adequate model for the Didymos System dynamics to apply to the asteroids propagation. The dynamical models for Didymos primary and secondary are presented in the following paragraphs.

### 3.2.1 Didymos system

In order to integrate the ephemerides of the Didymos system, the following approach was used:

1. At first, the state of both Didymos Barycenter is retrieved from JPL Solar System Dynamics team's spice kernel<sup>1</sup> [14, 47] at the DART scheduled impact date  $T_0$ . As reference, its state at the DART nominal impact time from the current most updated ephemerides is provided in table 3.3.
2. The Didymos Barycenter ephemeris is numerically integrated, including point-mass relativistic gravitational accelerations due to the Sun, all planets of the Solar System (including Pluto and the Moon). Their position and masses are retrieved from JPL's planetary ephemerides DE430.

The heliocentric orbit of the Didymos system is one of the parameters estimated during the OD process, whose *a priori* covariance (in the form of the full covariance matrix, table 3.4) is given in Brouwer-Clemence set III parameters coming from the DART JPL NAV's from the estimation filter for DART probe [41]. In fact, as part of the DART NAV, the Didymos system must be estimated to target the impact site correctly. The information

<sup>1</sup>[ftp://ssd.jpl.nasa.gov/pub/eph/small\\_bodies/dart/didymos/](ftp://ssd.jpl.nasa.gov/pub/eph/small_bodies/dart/didymos/)

Table 3.3: Didymos Barycenter state at DART nominal impact time in EME2000 from JPL Solar System Dynamics team’s spice kernel [14].

Body	Center	Parameter	Value	Unit
Didymos Barycenter	Sun	Position	1.556582810868216e+08	km
			1.581386951421298e+07	km
			-2.558931837509143e+06	km
		Velocity	-7.322747786998602e+00	km/s
			3.006402988694760e+01	km/s
			1.411538767083852e+01	km/s

about the Didymos-S/C relative position comes from optical navigation. During pre-operation NAV analysis of the DART team, OD simulations were performed, providing the full estimated covariance matrix of the solve-for parameters at different DCO. Therefore, the considered covariance matrix is a subset of the full one, only including the parameters of interest. To be conservative, the DCO used for the LICIACube analyses is 2 days prior to the CubeSat release.

Table 3.4: Didymos barycenter state uncertainty on October 1st, 2022 at 00:00 ET, computed from DART NAV team using  $\text{DCO}=T_0 - 12$  days [41], expressed as covariance matrix of Brouwer-Clemence set III parameters (lower triangular representation of the full matrix). For clarity, values are reported rounded to the third decimal. DMW, DP, DQ, and EDW are expressed in *rad*.

	DMW	DP	DQ	EDW	DA	DE
DMW	1.560e-16					
DP	2.775e-17	9.232e-17				
DQ	-2.135e-17	-5.808e-18	4.835e-17			
EDW	1.326e-16	4.841e-17	-4.677e-17	1.967e-16		
DA	-1.998e-17	-1.713e-18	1.891e-19	-6.391e-18	9.381e-18	
DE	-2.346e-17	-1.542e-17	1.578e-17	-4.567e-17	-2.696e-18	1.335e-17

### 3.2.2 Dimorphos

Once obtained the system barycenter’s trajectory, the orbit of Dimorphos is computed numerically integrating the equations of motion, starting from the state at the DART nominal impact time shown in table 3.5 (as for Didymos Barycenter, retrieved from JPL Solar System Dynamics team’s spice kernel). The model includes the point mass and

Table 3.5: Dimorphos state at DART nominal impact time, in EME2000 [47].

Body	Center	Parameter	Value	Unit
Dimorphos	Didymos Barycenter	Position	-8.351478968100919e-01	km
			-7.723021340271040e-01	km
			-3.546674166293227e-01	km
		Velocity	-1.217785645358754e-04	km/s
			1.236717440128706e-04	km/s
			1.745624204506784e-05	km/s

spherical harmonics accelerations due to Didymos. Moreover, the model includes point-

masses accelerations due to the Sun and all planets of the Solar System (including Pluto and the Moon), whose position and masses are retrieved from JPL’s planetary ephemerides DE430. On the other hand, the following accelerations are neglected:

- relativistic perturbations, due to low Didymos mass;
- Dimorphos’ spherical harmonics induced acceleration (indirect oblateness), since it is usually small,
- non-gravitational accelerations due to SRP, albedo and thermal emissions. These are expected to be several orders lower than the gravity terms, thus their effects to LICIACube will be negligible.

Based on the above mentioned conditions, the resulting orbit of the secondary about the primary, integrated for the entire time span of the LICIACube mission, is shown in figure 3.1. Some considerations are worth to be made concerning the average orbital parameters

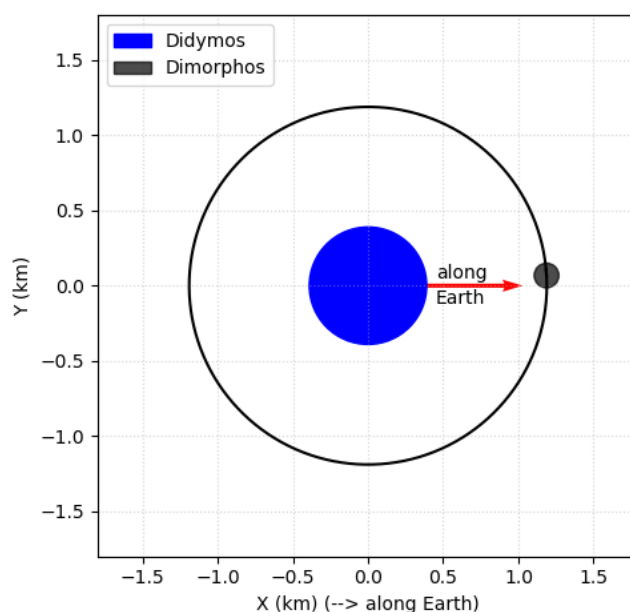


Figure 3.1: Dimorphos orbit around Didymos primary during LICIACube mission (XY plane). +Z is the pole of Didymos primary, +X is the normal to +Z, toward Earth. The position of Dimorphos is specified at DART nominal impact time.

changes from the input nominal value because of the orbital perturbations acting on the secondary, mainly the primary’s spherical harmonics and the Sun tide. In particular, the average semi-major axis and eccentricity are nearly constants to their nominal values, respectively 1.2 km and 0. On the contrary, the argument of pericenter has a large variation rate, although the effects are limited, being the orbit nearly circular. Finally, the inclination is bounded below 0.04 deg.

Regarding the initial uncertainty of Dimorphos, a rough estimation of a diagonal covariance has been performed, as no covariance has been ever released for the JPL’s ephemeris. Dimorphos position uncertainty could be directly assessed by the semi-major axis uncertainty, being about 0.03 km [18]. To get the uncertainty for the speed components, a little manipulation is required. Assuming a perfectly round orbit speed  $v = \sqrt{GM_{Dimorphos}/a}$  and the relation about speed and semi-major axis uncertainty  $\sigma_v/v = \sigma_a/2a$ , thus we

obtain the final relation  $\sigma_v = GM_{Dimorphos}\sigma_a/2a^2 \approx 2.2mm/s$ , rounded to a value of 3.0 mm/s to be conservative.

### 3.3 Shape models

The shape models of the asteroids are not perfectly known. Although detailed shape has been estimated for the primary, this does not directly affect the trajectory of the S/C, but only the generation of optical observables. Thus, the shape model [48] implemented in the filter is based on simpler assumptions considering Didymos primary as a sphere of radius of  $390m \pm 15m$ , and the secondary as a tri-axial body aligned with the body-reference frame, with semi-principal axes  $a = 103m \pm 16m$ ,  $b = 80m \pm 10m$  and  $c = 67m \pm 8m$  [54].

### 3.4 Gravitational models

In general, large celestial bodies such as planets, dwarf planets, and natural satellites are big enough to reach a condition near the hydrostatic equilibrium, namely the equilibrium between the self-gravity compression and the internal pressure. Under this assumption, their shape is nearly spherical with radially symmetric density. Although, corrections can be applied to the gravity field to account for their rotation about a spin axis and tidal forces due to other celestial bodies. Thus, the gravity potential  $U$  of these bodies can be represented by a spherical harmonics expansion, which represents functions with small deviations from the spherical symmetry condition [7]:

$$U(r, \lambda, \phi) = \frac{GM}{r} \sum_{l=0}^{\infty} \sum_{m=0}^{\infty} \left(\frac{R}{r}\right)^l \bar{P}_{lm}(\cos \lambda) (\bar{C}_{lm} \cos m\phi + \bar{S}_{lm} \sin m\phi) \quad (3.7)$$

where:

- $(r, \lambda, \phi)$  is the evaluation point in spherical coordinates (radius, latitude, longitude), in the body-fixed frame;
- $GM$  is the gravitational parameter of the body;
- $R$  is the surface radius
- $l$  and  $m$  are respectively the *degree* and the *order* of the expansion;
- $\bar{P}_{lm}$  is the associated Legendre function of degree  $l$  and order  $m$ ;
- $\bar{C}_{lm}$  and  $\bar{S}_{lm}$  are the experimental Stoke's coefficients of degree  $l$  and order  $m$ , which define the field.

According to the MacCullagh's formula, the un-normalized degree-2 coefficients have a direct physical meaning as they are related to the moments of inertia [7]:

$$\begin{cases} C_{20} = \frac{I_{yy} + I_{xx} - 2I_{zz}}{2MR^2} \\ C_{22} = \frac{I_{yy} - I_{xx}}{4MR^2} \\ C_{21} = -\frac{I_{xz}}{MR^2} \\ S_{21} = -\frac{I_{yz}}{MR^2} \\ S_{22} = -\frac{I_{xy}}{2MR^2} \end{cases} \quad (3.8)$$

Note that if the body-fixed axes are principal axes, thus the matrix of inertia is diagonal and only terms  $C_{20}$  and  $C_{22}$  are not zero. However, if a misalignment exists between the body-fixed frame and the principal axes, all the degree-2 terms are not zero. Hence, the shift can be modeled as a sequence of small rotations 1-2-3 of the Euler angles  $(\theta_1, \theta_2, \theta_3)$  and neglecting the second-order terms, the previous equation can be rewritten as [7]:

$$\begin{cases} C_{20} = \frac{I_{yy} + I_{xx} - 2I_{zz}}{2MR^2} \\ C_{22} = \frac{I_{yy} - I_{xx}}{4MR^2} \\ C_{21} = (2C_{22} - C_{20})\theta_2 \\ S_{21} = (2C_{22} + C_{20})\theta_1 \\ S_{22} = -2C_{22}\theta_3 \end{cases} \quad (3.9)$$

The magnitude of the spherical harmonics coefficients decreases with the degree corresponding to the shape and density deviations decreasing in amplitude with their characteristic length scale. This fact is well described by the empirical rule of Kaula, followed by the Earth and other terrestrial planets:

$$RMS(l) = \sqrt{\frac{1}{2l+1} \sum_{m=0}^l (\bar{C}_{lm}^2 + \bar{S}_{lm}^2)} \approx \frac{K}{l^2} \quad (3.10)$$

where  $RMS(l)$  is the degree Root Mean Square (RMS) of the gravity field and  $K$  is an experimental coefficient (about  $8.17 \cdot 10^{-6}$  for the Earth). Nonetheless, when dealing with smaller bodies such as small natural satellites, asteroids or comets, the shape may be quite different than a spherical object and the model may suffer because of local irregularities. Therefore, additional formulations are usually employed to overcome the issue and describe the gravity potential of small, irregular bodies. The main models [68, 69, 49, 34] are:

**Spherical harmonics expansion** This model is widely used in geodesy and it is already implemented in OD codes. Although it is uniformly convergent only outside the Brillouin sphere, the sphere with the minimum radius which encloses the body. It can diverge near the body's surface, and Kaula's rule is not applicable.

**Ellipsoidal harmonics** Similarly to the previous method, the model is uniformly convergent only outside the Brillouin ellipsoid, with the minimum axes to enclose the body. Thus, it can approximate irregular bodies better than a spherical model, as the field is more convergent and requires fewer coefficients to converge to the same precision. The drawbacks are represented by the increasing complexity of the base functions and that it is not implemented in MONTE.

**Polyhedron gravity** This method is the most accurate and provides an exact solution outside the body, surface included. It is available in MONTE but is applicable only for uniform density. Moreover, it is computationally intensive and cannot be used to estimate the gravity field.

Since the LICIAcube spacecraft is always outside the Brillouin sphere, the spherical harmonics method is applied.

### 3.4.1 Didymos primary

Didymos primary is modeled using a spherical harmonics expansion, whose coefficients were obtained from the available polyhedron shape. To retrieve the coefficients the poly-

hedron was represented as a spherical harmonics expansion of degree 20 in the form [51]:

$$r(\lambda, \phi) = \sum_{l=0}^L \sum_{m=0}^l \bar{P}_{lm}(\cos \lambda) \left( \bar{C}_{lm}^r \cos m\phi + \bar{S}_{lm}^r \sin m\phi \right) \quad (3.11)$$

Then, the shape coefficients were obtained through a least-square fit of the polyhedron vertices, with the maximum degree chosen to obtain a resolution comparable to the polyhedron representation. The obtained fit RMS of the vertices is about 2.2 m. Finally, the shape coefficients  $\bar{C}_{lm}^r$  and  $\bar{S}_{lm}^r$  were converted to the gravity ones  $\bar{C}_{lm}$   $\bar{S}_{lm}$ , assuming a uniform density, using the following relation [51]:

$$\bar{C}_{lm} = \frac{4\pi\rho R^3}{M(2l+1)} \sum_{n=1}^{l+3} \frac{\bar{C}_{lm}^{r^n}}{R^n n!} \frac{\prod_{j=1}^n (l+4-j)}{l+3} \quad (3.12)$$

being  $\rho$  the averaged density of the body,  $R$  the gravity reference radius, and  $\bar{C}_{lm}^{r^n}$  the coefficients of degree  $l$  and order  $m$  of the spherical harmonics expansion of the  $n$ -th power of the topography  $r^n$  computed previously.

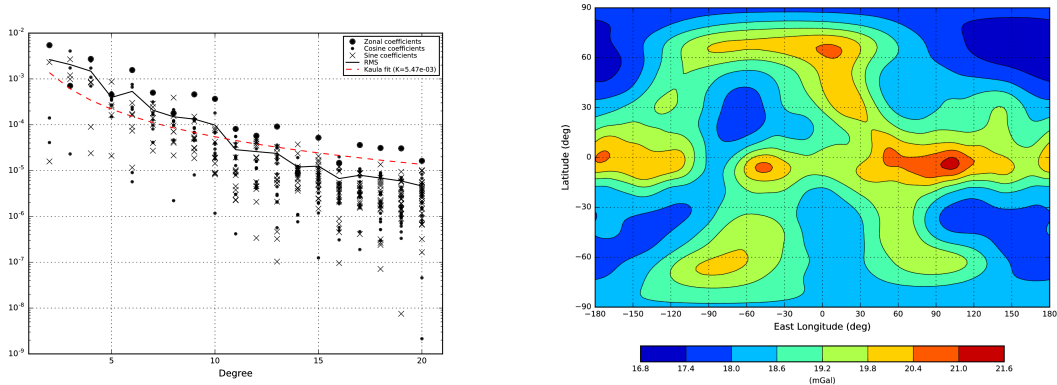
The resulting normalized gravity coefficients of Didymos primary are shown in table 3.6. Degree-1 terms were neglected to constrain the center of mass to the center of the body-fixed frame. The resulting gravity field is represented in figure 3.2.

Table 3.6: Gravitational model for Didymos primary: spherical harmonics normalized coefficients up to degree 5. A full 20-degree model was used in the simulations. Reference values are  $R = 0.43$  km and  $GM = 3.4903 \cdot 10^{-8}$  km<sup>3</sup>/s<sup>2</sup>.

$l$	$m$	$C_{lm}$	$S_{lm}$
2	0	-5.4414743136e-03	0.0000000000e+00
2	1	4.0945217287e-05	-1.5829601825e-05
2	2	-1.4073608724e-04	2.3099303443e-03
3	0	-7.0532572456e-04	0.0000000000e+00
3	1	4.0687288743e-03	-2.6785924152e-03
3	2	1.7340065845e-03	1.1971981967e-03
3	3	-2.3043108965e-05	-9.8570889912e-04
4	0	2.7263334618e-03	0.0000000000e+00
4	1	1.7223989051e-03	-8.2930089864e-04
4	2	-6.9755159206e-04	-8.9908646031e-05
4	3	2.4652971978e-03	8.5964834954e-04
4	4	-1.0879867359e-03	-2.3902478262e-05
5	0	-4.5151098907e-04	0.0000000000e+00
5	1	2.6954652211e-04	-2.6710658041e-04
5	2	5.0066410994e-04	-2.0987585438e-05
5	3	1.4888455908e-04	8.6630282872e-04
5	4	3.4400583810e-04	1.6293396449e-04
5	5	-3.7237737755e-04	2.4437301598e-04

### 3.4.2 Didymos secondary

Dimorphos is modeled as a homogeneous tri-axial ellipsoid aligned with the body-fixed axes. Due to the larger uncertainty related to its shape knowledge, the computation was



(a) Absolute value of spherical harmonics normalized coefficients up to degree 20, RMS of coefficients for each degree and fit of RMS using Kaula's rule. (b) Norm of gravity acceleration vector on the reference sphere.

Figure 3.2: Gravitational model of Didymos primary.

limited to degree-2 un-normalized gravity coefficients by the equations [10]:

$$C_{20} = \frac{2c^2 - (a^2 + b^2)}{10R^2} \quad (3.13)$$

$$C_{22} = \frac{a^2 + b^2}{20R^2} \quad (3.14)$$

with all the other degree-2 coefficients are zero.

The resulting un-normalized gravity coefficients of Dimorphos are shown in table 3.7. Degree-1 terms are assumed to zero to constrain the center of mass to the center of the body-fixed frame. The center of mass portion is updated estimating its orbit with respect to Didymos primary.

Table 3.7: Gravitational model for Didymos secondary: spherical harmonics un-normalized coefficients of degree 2. Reference values are  $R = 0.103$  km and  $GM = 3.23 \cdot 10^{-10}$  km<sup>3</sup>/s<sup>2</sup>.

$l$	$m$	$C_{lm}$	$S_{lm}$
2	0	-7.6708455085e-02	0.0000000000e+00
2	1	0.0000000000e+00	0.0000000000e+00
2	2	2.0586294655e-02	0.0000000000e+00

## 3.5 LICIAcUBE spacecraft models

Once the celestial bodies' environment has been implemented, it is necessary to provide a model for the spacecraft to compute its trajectory. It requires a complete definition of the accelerations acting on the spacecraft itself and the probe's characteristics.

### 3.5.1 Initial conditions

Since the release of LICIAcUBE occurs from the piggyback dispenser mounted on DART, the CubeSat initial condition is assumed coincident to the DART one. Therefore, the

unperturbed DART state coming from the released APL’s reference kernel<sup>2</sup>, is used as *a priori* for LICIACube, as summarized in table 3.8. The LICIACube *a priori* uncertainty is assumed by scaling the DART covariance matrix [41] by a safety factor of 2. The resulting covariance matrix is shown in table 3.9 with respect to Didymos Barycenter, as we are mostly interested in the probe’s state estimation with this reference. The above conditions do not take into account the instantaneous variation of the S/C velocity at the release epoch, as the deployment effects are modeled by following application of a force as described in the section 2.6.3.

Table 3.8: LICIACube state (assumed coincident to DART) at release epoch, in EME2000.

Body	Center	Parameter	Value	Unit
LICIACube	Solar System Barycenter	Position	1.555300269613551e+08	km
			-6.128945233180023e+06	km
			-1.298219543793794e+07	km
	Velocity	8.889916735941847e-01	km/s	
		2.555337253400575e+01	km/s	
			1.202091952644832e+01	km/s

Table 3.9: LICIACube uncertainty with respect to Didymos Barycenter at release epoch in EME2000, computed using  $\text{DCO}=T_0 - 12$  hours (lower triangular representation of the full matrix). For clarity, values are reported rounded to third decimal. Positions are expressed in *km*, velocities in *km/s*.

	X	Y	Z	$V_x$	$V_y$	$V_z$
X	3.305e+01					
Y	-3.093e+01	5.298e+01				
Z	-2.963e+00	1.765e+01	2.274e+01			
$V_x$	2.385e-05	-1.123e-05	9.469e-06	6.193e-11		
$V_y$	-8.485e-06	1.111e-05	-1.151e-07	-1.068e-11	3.548e-11	
$V_z$	1.108e-05	-1.924e-06	1.314e-05	2.064e-11	-3.052e-12	4.758e-11

### 3.5.2 Forces

To correctly estimate the trajectory of LICIACube keeping the computational requirement as low as possible, one should assess the major forces the probe experiences. Main accelerations acting on the S/C are related to the Solar System bodies (including Pluto and the Moon) and Didymos gravity. Then, a simple evaluation of the secondary accelerations acting on the probe at different distances from the Didymos system could be done to compute the magnitude of each one. All those forces were estimated using simplified formulations in an early phase of the work and were the base for the forces implemented in the model. The magnitude of each acceleration is shown in figure 3.3. Considering the Didymos flyby distance, this result suggested that other than gravitational forces, the SRP should also be included, being about one order larger than every other acceleration. Although asteroids GM’s are also negligible compared to SRP, they were considered as well since these could provide relevant information with a different type of observables and

<sup>2</sup>DART kernel released on 26th April, 2021 on DART SOC (<https://dart.jhuapl.edu/>), under restricted access.

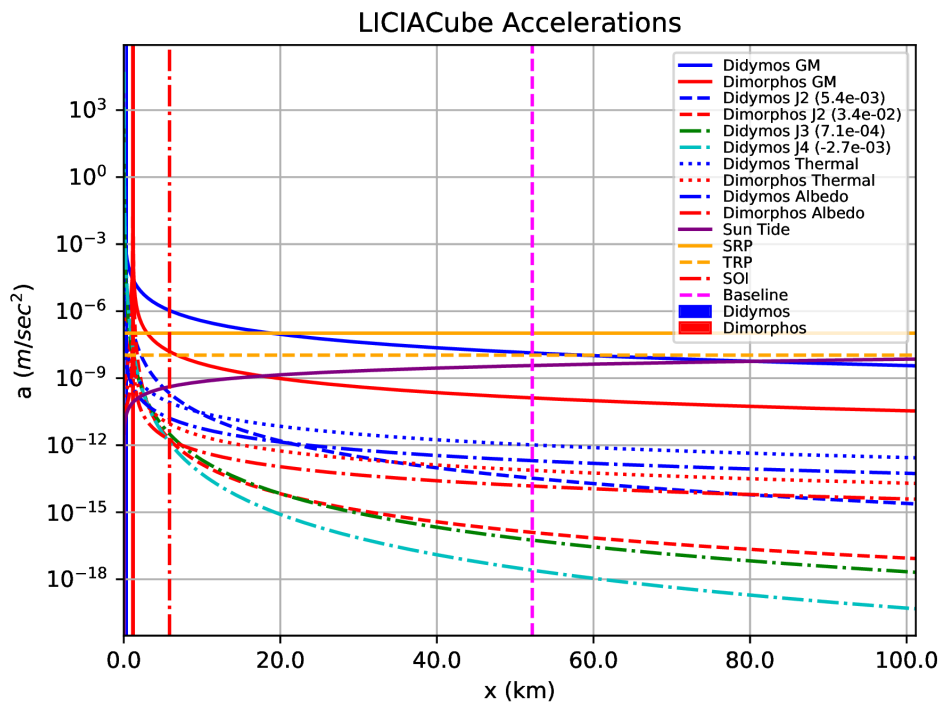


Figure 3.3: LICIAcUBE accelerations near to the C/A.

during post-flyby reconstruction. At the end of this preliminary assessment of the forces, the model includes:

- Newtonian point-mass accelerations given due to the Sun, all the planets of the Solar System, and Pluto;
- relativistic perturbations given by Sun, Jupiter and Earth;
- main gravitational accelerations given by the point-mass gravity of the asteroids;
- SRP acceleration using a simple shape model of the spacecraft (par 3.5.3).

All other forces are neglected, including the spherical harmonics, relativistic perturbation and albedo of the Didymos asteroids, and the thermal recoil pressure of the S/C. Therefore, a stochastic noise is accounted for in the estimation process, as described in paragraph 3.5.6.

### 3.5.3 Shape

The S/C-fixed frame origin is set on the back face  $1U \times 2U$  midpoint, i.e., the side opposite to the cameras pointing. The  $z$ -axis is assumed in the same direction as the nominal cameras pointing, along with the  $3U \times 2U$  side, while the  $x$ -axis is toward the  $1U \times 3U$  face opposite to the Solar Arrays. The  $y$ -axis completes the ortho-normal frame. The assumed LICIAcUBE shape is a simplified set of plates, easier to implement into the software setup. The S/C shape is depicted in figure 3.4 with the attached S/C Frame. The implemented data for the plates area, orientation, and optical properties are in table 3.10.

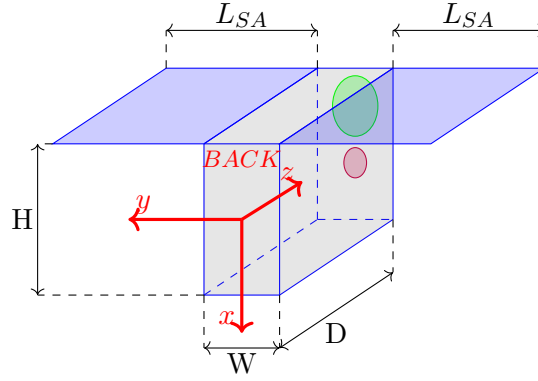


Figure 3.4: LICIACube shape.

Table 3.10: LICIACube geometrical [42] and optical properties [16] by panels. Orientation is intended as the versor normal to the panel, in the S/C Frame

Component name	Sides	Area ( $m^2$ )	Orientation S/C Frame	Reflection coefficients	
				Specular	Diffusive
Bus top	$W \times D$	0.038	(-1,0,0)	0.0	$0.75 \pm 0.02$
Bus bottom	$W \times D$	0.038	(+1,0,0)	0.0	$0.75 \pm 0.02$
Bus side (Y+)	$H \times D$	0.087	(0,+1,0)	0.0	$0.75 \pm 0.02$
Bus side (Y-)	$H \times D$	0.087	(0,-1,0)	0.0	$0.75 \pm 0.02$
Bus front	$W \times H$	0.025	(0,0,+1)	0.0	$0.75 \pm 0.02$
Bus back	$W \times H$	0.025	(0,0,-1)	0.0	$0.75 \pm 0.02$
Solar Arrays front	$2L_{SA} \times D$	0.286	(-1,0,0)	$0.23 \pm 0.01$	0.0
Solar Arrays back	$2L_{SA} \times D$	0.286	(+1,0,0)	0.0	$0.75 \pm 0.02$

### 3.5.4 Solar Radiation Pressure

The SRP is related to the radiation coming from the Sun, mostly as visible light as a photons flux  $\Phi_s$ . Assuming a point light source centered in the Sun, whose intensity is proportional to the distance squared, the total momentum carried by the photons in the solar flux can be estimated as  $\Phi_s/c$ , being  $c$  the light speed. The model of momentum transfer related to the impact of the photons on the probe surfaces is a combination of three contributions:

- absorption, as the S/C acts as a black body;
- reflection, as the photons bounce on the S/C surface with specular angle;
- diffusion, as the photons are re-emitted with decreasing relative intensity as the  $\cos(\theta)$  from the normal to the surface (Lambert's law).

These three contribution are related to three positive constant, such that:

$$\alpha + \delta + \gamma = 1 \quad (3.15)$$

constraining the fraction of light absorbed ( $\alpha$ ), reflected ( $\delta$ ) and diffused ( $\gamma$ ).

Under these assumptions, the force applied by the SRP on a generic element of the external surface of the S/C can be split into two contribution: one along the surface normal

direction, one along the direction to Sun. The overall contribution of the illuminated surface ( $S$ ) can be expressed as:

$$\mathbf{F} = -\frac{\Phi_S}{c} \int_S [(1 - \rho) \cos \beta \hat{\mathbf{s}} + \left(\frac{2}{3}\delta + 2\rho \cos \beta\right) \cos \beta \hat{\mathbf{n}}] dS \quad (3.16)$$

where  $\mathbf{F}$  is the direct radiation pressure force acting on the S/C, being  $\Phi_S = C_1/r_{sp}^2$  the solar flux at the S/C distance,  $C_1$  the solar flux constant at 1 AU,  $r_{sp}$  is the Sun-spacecraft distance,  $\beta_i$  the angle between the Sun direction  $\hat{\mathbf{s}}$  and the normal to the surface  $\hat{\mathbf{n}}_i$ .

The MONTE software relies on a more detailed model for the SRP, where the overall force due to SRP is computed as independent contributions on each surface of the S/C. For LICIAcUBE, a parallelepiped-shape S/C has been modeled using flat plates. Based on that, the total acceleration is computed as:

$$\ddot{\mathbf{r}} = -\frac{\Phi_S}{mc} \sum_{S_i} [(1 - \rho_i) \cos \beta_i \hat{\mathbf{s}} + \left(\frac{2}{3}\delta_i + 2\rho_i \cos \beta_i\right) \cos \beta_i \hat{\mathbf{n}}_i] S_i \quad (3.17)$$

being  $m$  the spacecraft mass. Thus, the SRP force acting on each of the S/C component is a function of its orientation with respect to the Sun, shape, and its surface properties, namely the specular ( $\rho$ ) and diffusive ( $\delta$ ) reflectivity coefficients. These two latter data can be found in table 3.10.

Note that this simplified model only considers a static illumination condition, neglecting all the effects related to self-shadowing of the S/C surfaces, variability of thermal conditions, and the surface degradation. In order to account for these effects, a scale factor is introduced in the estimation process as a bias constant representing the average value of the SRP. The *a priori* uncertainty assumed for this parameter is 3% of the nominal computed SRP value.

### 3.5.5 Maneuvers

All the maneuvers of the mission are planned to be performed before the C/A to target the given aimpoint with the highest possible accuracy. In particular, the deterministic maneuver OM1 is used for the main targeting, providing the required nominal aimpoint and the arrival epoch by a slight deceleration. On the other hand, the statistical maneuvers aim at reducing the dispersion, thus controlling possible deviations from reference trajectory during operations. Considering the  $\Delta V$  scheduled in section 2.6.3, the duration of the maneuvers is expected in the order of a few minutes at most. Thus, it allowed modeling maneuvers as impulsive burns, an instantaneous variation of the spacecraft velocity components. Analyses were performed in section 4.7.3 to test the correctness of this assumption.

The release, formally not a proper maneuver, also represents a quasi-instantaneous variation of the probe's speed. Therefore, it has been inserted into the maneuvers list and implemented as an impulsive burn with a zero-mass variation.

### 3.5.6 Stochastics

The overall set of the implemented accelerations discussed is due to some known physical effects. In addition, some stochastic acceleration has been included to account for any unmodeled effect or mismodeling. This *virtual* acceleration does not have an actual physical meaning but serves to absorb the model's error during the estimation phase. The stochastic acceleration is modeled as a 24 hours time-batched white random noise with

a standard deviation of  $1.0 \cdot 10^{-11} km/s^2$  (the order of the largest neglected acceleration, corresponding to a conservative value of 20 times with respect to [5]). Hence, the value is reset to the nominal value of zero at the end of each time batch, and each batch is assumed uncorrelated from the others. Different batch lengths and *a priori* standard deviations were investigated (section 4.7.1) to verify the behavior of stochastics in the reconstruction process.

# Chapter 4

## Orbit Determination simulations

### Contents

---

<b>4.1</b>	<b>Introduction</b>	<b>47</b>
<b>4.2</b>	<b>Procedure</b>	<b>47</b>
4.2.1	Requirements verification	49
<b>4.3</b>	<b>Measurements</b>	<b>51</b>
4.3.1	Radio-tracking	53
4.3.2	Optical measurements	54
<b>4.4</b>	<b>Maneuvers execution</b>	<b>56</b>
<b>4.5</b>	<b>Parameters</b>	<b>57</b>
<b>4.6</b>	<b>Baseline results</b>	<b>58</b>
<b>4.7</b>	<b>Robustness analysis</b>	<b>67</b>
4.7.1	A-priori covariance	68
4.7.2	Observables	76
4.7.3	Maneuver model	82

---

### 4.1 Introduction

A pre-operation simulation campaign has been performed to assess the expected performance of the LICIACube, and to support the MA in designing the optimal trajectory and its verification against the constraints. Along with the nominal trajectory propagated using the model presented in chapter 3, covariance analyses have been used to compute the expected formal uncertainties throughout the whole mission to check the navigation requirements under different operations assumptions.

In addition, extensive robustness analyses have been performed to investigate the sensitivity of the solutions to all major parameters and design the best operations timeline for the mission. These investigations regarded, among the other parameters, the maneuvers positioning and the tracking passes, so that the system have been verified to be suitable for the mission's goals.

### 4.2 Procedure

The OD of LICIACube could be seen as part of the more general process of NAV. Hence, it is necessary to estimate the trajectory of the spacecraft to compute the corrective maneuvers to adjust the computed trajectory to the reference one. The reference trajectory,

outcome of the preliminary MA, is designed as a trade-off between the maximization of the scientific return and the probe safety and navigability. In the earlier phase of the MA, OD simulations allow inferring the attainable accuracy of the spacecraft in any part of its baseline trajectory even before the mission starts. This analysis to check the viability of the orbital control and the fulfillment of the mission requirements is done through the so-called *covariance analysis*, namely a numerical simulation of the OD process with a procedure similar to the one used for the analysis of real data, but using simulated data, generated by the same software. Moreover, controlling the dynamical model used to generate the simulated measurements may provide a better understanding of the main design parameters which affect the performances of the OD and their effects on the achievable results. It is also worth noting that this kind of analysis does not account for any model error: the results are aligned in their mean values, just corrupted with different stochastic processes. For this reason, the *a priori* values used are often conservative enough to provide robustness of the model against possible errors which may be found during the real operations. For instance, in this work, the following assumptions were made:

- the implemented Doppler measurement noise is larger than expected by a factor 4;
- the implemented Range measurement noise is larger than expected by a factor 10;
- the *a priori* uncertainty related to the DART spacecraft at release is larger than expected by a factor of 2.

The simulation procedure adopted for the study is thus divided into three subsequent steps:

- 1 setup of the dynamical model;
- 2 generation of the *simulated observed* measurements:
  - i computation of Didymos system trajectory in the Solar System, by numerical integration;
  - ii computation of Dimorphos and Didymos trajectories around the common center of mass, by numerical integration;
  - iii computation spacecraft's trajectory, by numerical integration;
  - iv computation of the noiseless measurements given the measurements model;
  - v computation of the simulated observed measurements (*observed observables*,  $\tilde{z}$ ) adding the assumed noise levels.
- 3 perform Orbit Determination:
  - i computation of the simulated measurements (*computed observables*,  $\hat{z}$ ) following the same procedure at point 2iv;
  - ii generation of the pre-fit residuals as  $r_{prefit} = \tilde{z} - \hat{z}$ . Because the model adopted in the two sets of measurements is the same, the residuals are the sum of the simulated and the numerical noises (this latter is usually negligible);
  - iii apply the observation schedule by cutting the simulated observables;
  - iv set the filter by defining *a priori* covariances, stochastic properties, and parameters;
  - v run the least-squares filter to estimate the values and covariance matrix of the set of the solve-for parameters and perform the mappings.

### 4.2.1 Requirements verification

Due to the uncertainty sources (initial conditions, maneuvers errors, dynamical parameters, etc...), the probe's state at a given epoch may result in a range of stochastic realizations, given the statistics of the sources and their evolution in time. Given the dynamics of the environment, the evolution of all the possible positions of the S/C, known as its dispersion, would require non-linear propagation of a sufficiently large batch of trajectories, as if each one would represent a different behavior of the same spacecraft, subject to slightly different conditions. In general, the requirements should be verified against the dispersion. Nonetheless, during the mission, the OD provides a significant contribution to state knowledge to determine both its nominal value and uncertainty. For this reason, in the pre-operations analyses, the dispersion computation should start from the last useful knowledge update, intended as the DCO which can have effects on the requirement itself. Thus, two different cases are identified:

- **flyby**: the requirements shall be verified on the dispersion starting from the conditions obtained at the DCO corresponding to the last maneuver calculation before the C/A. It would let to correct the nominal value during the operations, thus the interest is in the trajectory deviations occurring since this last maneuver.
- **pointing**: the requirements shall be verified on the dispersion starting from the conditions obtained at the DCO corresponding to the last useful pointing sequence upload. Since there is no way to control the nominal state of the S/C after that point, the pointing sequence can be updated based on the last propagated trajectory. It is valid both for camera and DSN pointing, comparing the angular uncertainty respectively to the FOV or the antenna beamwidth.

It is worth noting that if the problem is almost linear, the non-linear dispersion could be approximated by the linearized propagation obtained by the OD without considering any further data following the selected DCO. This approach is advantageous since, given an OD run corresponding to a specific DCO, the dispersion after the last acquired data can be obtained by propagating the state from the DCO itself, with the conditions reconstructed by the OD. Therefore, the navigation requirements can be verified directly on the results of the OD instead of using a non-linear dispersion (e.g., mapping the uncertainties obtained with the corresponding DCO).

The figure 4.1 depicts an ideal scenario to show how the verification of the OD results provides consistent information for the operations phase. The trajectory propagated for pre-operation analyses (referred to as *pre*) is coincident with the reference one considering its nominal value, while the red one is associated with operations reconstructed trajectory (referred to as *ops*).

Let us assume an initial dispersion given by the *a priori* covariance matrix at release epoch,  $P(t_{rel}|t_{rel})$ . The uncontrolled trajectory would evolve into a final dispersion at C/A given by  $P(t_{CA}|t_{rel})$ . Although, at the maneuver DCO we would have a certain a-posteriori OD covariance  $P(t_{DCO,OM}|t_{DCO,OM})$ , which should be equal between *pre* and *ops* cases, even though a bias in the nominal state may exists, since the *ops* trajectory will deviate, in general, from the nominal one. This uncertainty will be mapped forward to the maneuver epoch,  $t_{OM}$ . Thanks to the maneuver, at the  $t_{OM}$  the nominal *ops* trajectory will be, theoretically, realigned with the reference one. However, due to the maneuver execution and OD error, the two points of *ops* and reference trajectories will not be the same, and the dispersion of the possible point may be larger than the one mapped from the DCO, due to possible variation of the computed maneuver. From this epoch, there is

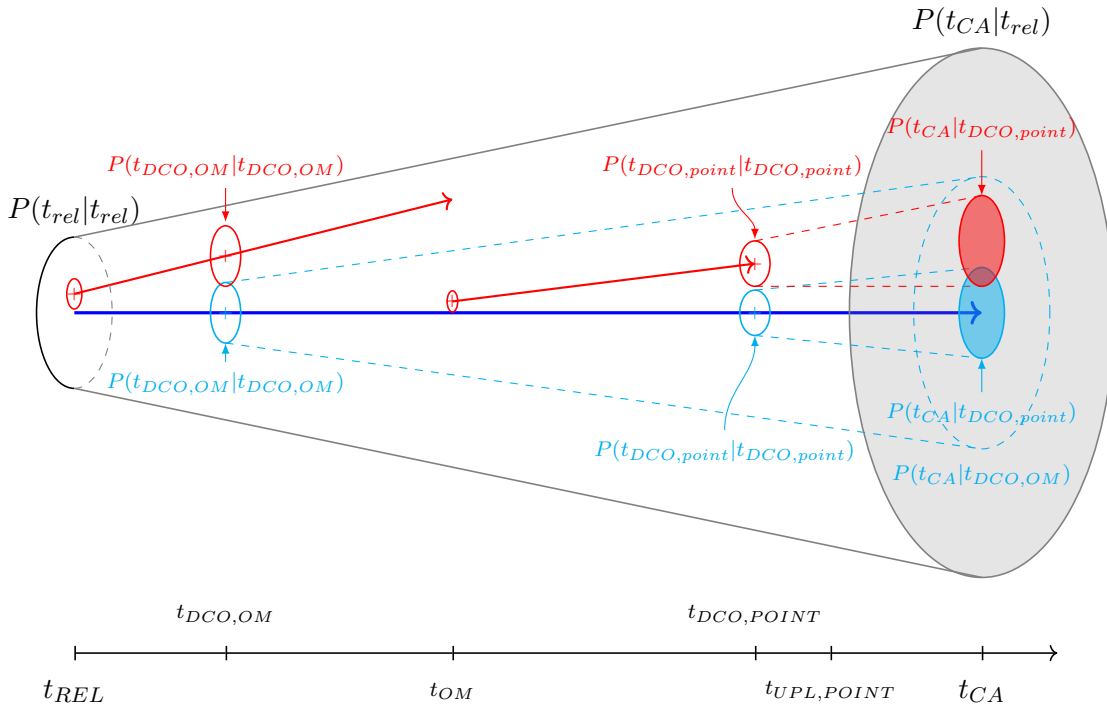


Figure 4.1: LICIACube dispersion verification. Covariance matrix notation:  $P(\text{time}|DCO)$

no more chance to correct the trajectory, thus the dispersion can be mapped to the C/A to obtain  $P(t_{CA}|t_{DCO,OM})$ . This covariance will be used to verify the requirements of the trajectory. Once again, a successive OD will be able to reconstruct the trajectory at the pointing DCO with an accuracy  $P(t_{DCO,point}|t_{DCO,point})$ . Since the last maneuver has already passed, deviation in trajectory cannot be corrected, although the pointing bias can be adjusted in the nominal pointing commanded. Nonetheless, given a small deviation, the uncertainty evolution will be similar for the two cases, therefore it will provide similar uncertainties at C/A, namely  $P(t_{CA}|t_{DCO,point})$ . All these considerations hold if, and only if, the dispersion from a specific epoch set as DCO can be approximated by the OD forward projection without further data from the DCO itself. A proof of this is given for the LICIACube trajectory in the next paragraph.

**Dispersion and covariance analysis** Generally speaking, the non-linear dispersion is different from the OD propagation. Although both are based on the same dynamical and observables model and assumptions, the former can be computed from a batch of independent propagations based on the same non-linear model but using randomly distributed realization for any uncertainty sources. Instead, the covariance analysis performs a unique propagation of the nominal value along with its partials derivatives. By taking the partials of the parameters vector  $\mathbf{x}$ , one could obtain the so-called State Transition Matrix (STM) as:

$$\Phi(t_0, t) = \frac{\partial \mathbf{x}(t)}{\partial \mathbf{x}(t_0)} \quad (4.1)$$

which expresses the sensitivity of the state parameter to their variation along time, between two epochs. Hence, given a generic DCO at  $t_1$ , the linearized approach of the covariance analysis consists of exploiting the STM to linearly mapping the uncertainty  $P(t_0|t_1)$  at an

epoch  $t_0$ , to  $P(t_0|t_2)$  at a different epoch  $t_2$ , still having the same DCO.

$$P(t_2|t_1) = \Phi(t_0, t_2)P(t_0|t_1)\Phi^T(t_0, t_2) \quad (4.2)$$

Linear approaches are often convenient to reduce the computational effort, but represent only an approximation, making this method usually suitable only for small branches of trajectory. Nonetheless, under sufficient linearity conditions, the non-linear dispersion and the covariance analysis will provide the same results.

The results consistency is proved by comparing the dispersion against the OD propagation. The former is performed through a Monte Carlo analysis, where 1000 trajectories were integrated using the full, non-linear model, whose initial conditions were chosen as *a priori* parameters random realizations. Instead, the latter is computed by a single OD propagation without any data, thus mapping the DCO coincident to the initial propagation epoch up to the encounter.

Two cases were considered in figure 4.2 for this aim: 4.2a includes the initial dispersion of the spacecraft provided by the full *a priori* state covariance matrix without any further maneuver, 4.2b also accounts for the targeting maneuver OM1. It is worth noting that, even though the two cases provide different nominal results in terms of B-plane arrival point, the linearity of the problem is demonstrated by the matching of the Monte Carlo distribution with the projected OD covariance on the B-plane.

Based on this result, it is correct to assume the LICIACube pre-flyby trajectory as a quasi-linear problem, and the OD propagation can be used instead of the dispersion for the requirements verification. This powerful tool allows checking the mission constraints related to the trajectory dispersion using a single linearized propagation along with the covariance mapping instead of performing a more complex and resource-consuming series of non-linear propagations.

**Pointing** The evaluation of the pointing navigation requirements, both to ground and Dimorphos, only accounts for the OD knowledge uncertainty of the LICIACube probe with respect to the target. A nominal nadir pointing is assumed to the target, and the covariance matrix of the relative position in spherical coordinates is computed at the relevant epoch(s). The corresponding geometric representation is depicted in figure 4.3.

For the antenna pointing, the check is done comparing the Earth-LICIACube angular uncertainty against the 3 dB power cone for the ground link. For the camera pointing, the Dimorphos-LICIACube angular uncertainty was conservatively compared to the FOV, because the roll angle (plane-of-sky orientation) is unknown. In both cases, a unique angle ( $\vartheta$ ) should be investigated as the angular deviation from the nominal pointing. It would be nicely verified by a z-pointing verification of the colatitude uncertainty, but a singularity may arise in the code as the nominal pointing is assumed at zero-angle colatitude. Thus, a nominal x-pointing is assumed from the spacecraft to the target, and a unique angular uncertainty  $\sigma_\vartheta$  is computed as:

$$\sigma_\vartheta = \sqrt{J_{\alpha,\delta} P_{\alpha,\delta} J_{\alpha,\delta}^T} \simeq \sqrt{\sigma_\alpha^2 + \sigma_\delta^2} \quad (4.3)$$

being  $\alpha$  and  $\delta$  the latitude and longitude of the target, and  $J_{\alpha,\delta} = [\partial\vartheta/\partial\alpha, \partial\vartheta/\partial\delta]$  the  $1 \times 2$  partials matrix of the angle respect to the latitude and longitude components.

### 4.3 Measurements

The measurements used for the LICIACube mission are aimed at trajectory reconstruction without any additional hardware requirements to the payloads already set by other subsys-

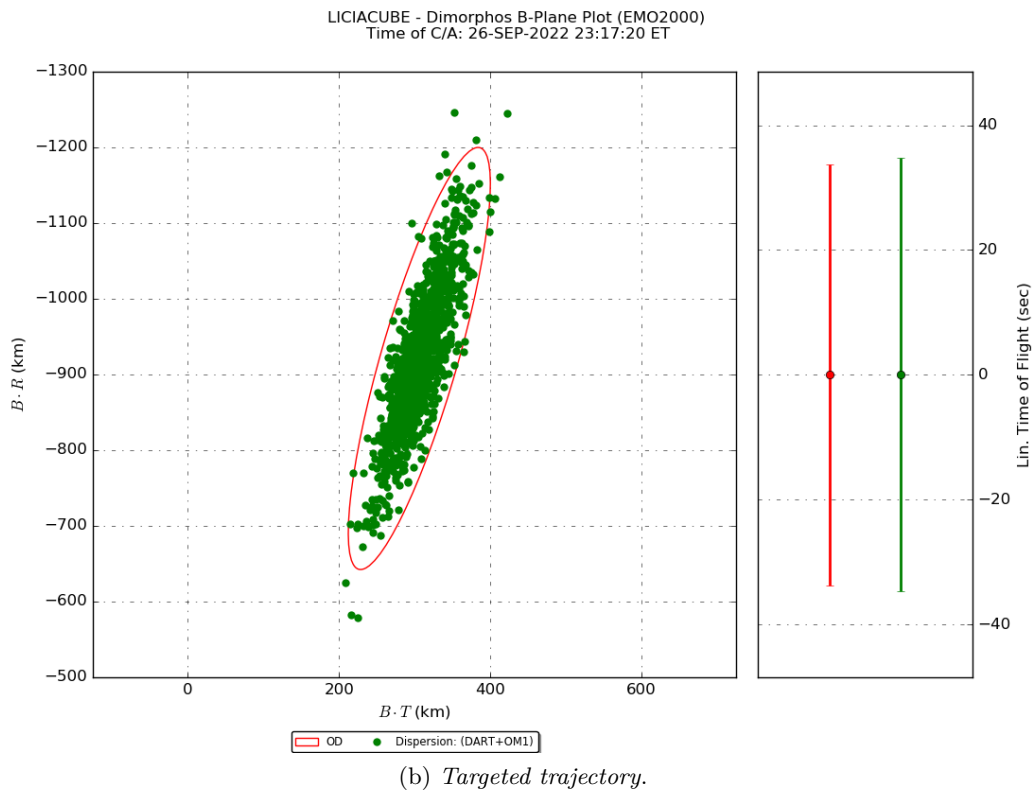
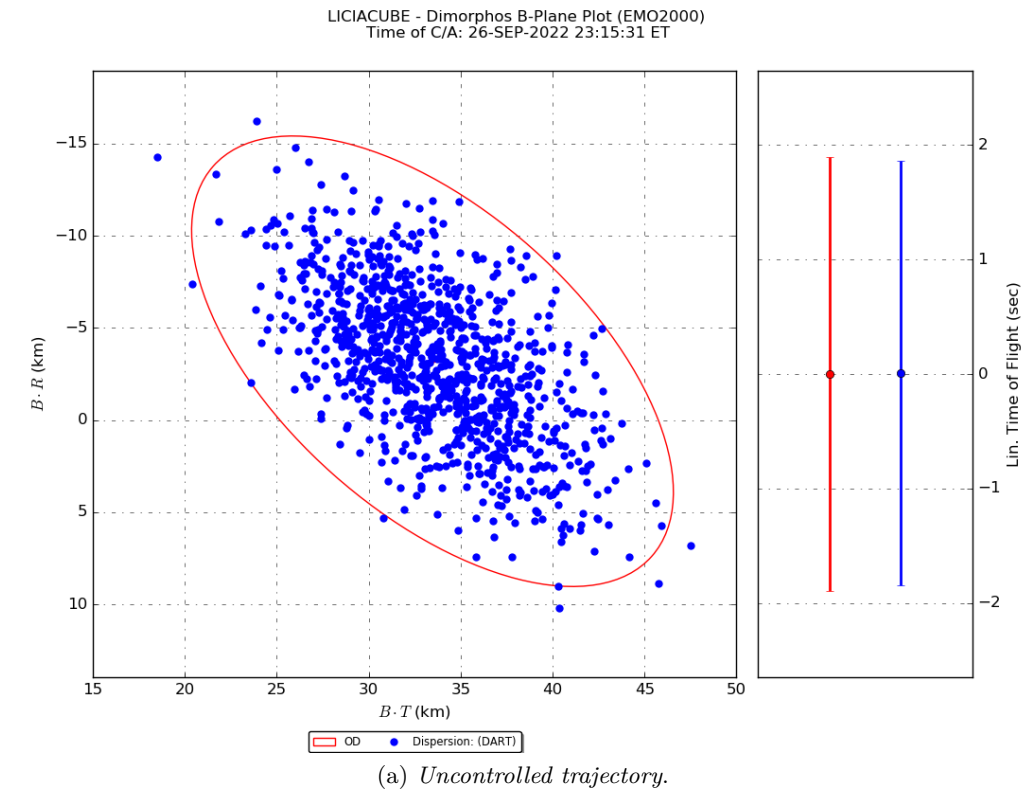


Figure 4.2: Comparison of B-plane dispersion and OD covariance propagations in the cases of uncontrolled (a) and targeted (b) trajectories.

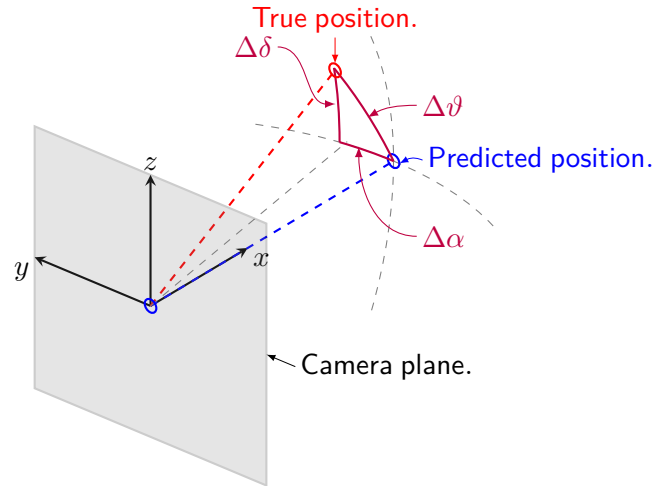


Figure 4.3: Pointing angle computation.

tems. In particular, the IRIS radio employed for telecommand upload and data download is also used to retrieve radiometric measurements, whilst primary optical payload is used, if possible, to have some OPNAV.

### 4.3.1 Radio-tracking

Based on the observation schedule described in section 2.6.1, measurements are simulated both for two-way Doppler and ranging between LICIA Cube and Earth ground stations with a count time of 60 seconds. During real operations, the DSN will provide 1 second count time Doppler data for a quick look evaluation and will be then compressed to 60 seconds by the OD operator before starting the process. The sampling time of ranging measurements is still to be defined. However, it is usually larger than 60 s. For simplicity, we used the same count time as Doppler data, adopting a conservative noise value. The simulated observables generation also accounts for a white Gaussian noise added to the measurements. Therefore, data are weighted during the filtering using the input noise level.

The typical performances of ranging measurements for deep space missions operated by the DSN are 0.5 m for random errors (noise) and 2-3 m for systematic errors (bias). Being LICIA a CubeSat mission, we considered a safety factor of 10 on noise, resulting in 5 m, and 15 m in the bias, to take into account possible variations of the transponder group delay, as reported in table 2.2. Conversely, the noise levels expected on the Doppler observables were computed using a simplified model for the main noise sources [35], namely:

- plasma noise;
- tropospheric noise;
- antenna mechanical noise and ground station electronics;
- spacecraft electronics.

The plasma noise implemented model is mainly a function of two contributions, specifically the carrier frequency at the X/X band and the Sun-Earth-Probe (SEP) angle. This latter provides maximum noise contribution during conjunctions (i.e.  $SEP=0^\circ$ ) and minimum during oppositions, where  $SEP=180^\circ$ . The SEP angle during the LICIA Cube mission is

represented in figure 4.4a. The antenna mechanical noise was assumed from typical values for DSN at 0.005 mm/s [35]. The spacecraft electronics noise typical values are increased by a factor of 10.

Also, tropospheric noise depends on two main parameters: the time, larger in summer and lower in winter, and calibration adopted. We assumed a standard GNSS-based calibration, which may calibrate up to 10-20% of the tropospheric noise. The overall expected noise contribution by source is shown in figure 4.4b, whereas the overall noise during the LICIACube mission is represented in figure 4.4c.

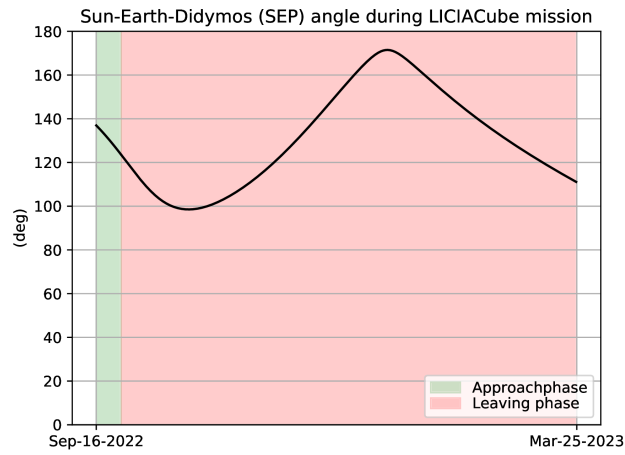
### 4.3.2 Optical measurements

At the moment, the baseline navigation does not include OPNAV, but only radiometric observables. However, these latter provide information with respect to the Earth, so the relative trajectory with respect to Didymos is computed relying on its ephemerides. Instead, OPNAV may offer several advantages and increased robustness because it provides direct information content relative to Didymos. Hence, the possible use of OPNAV was studied from an operational point of view.

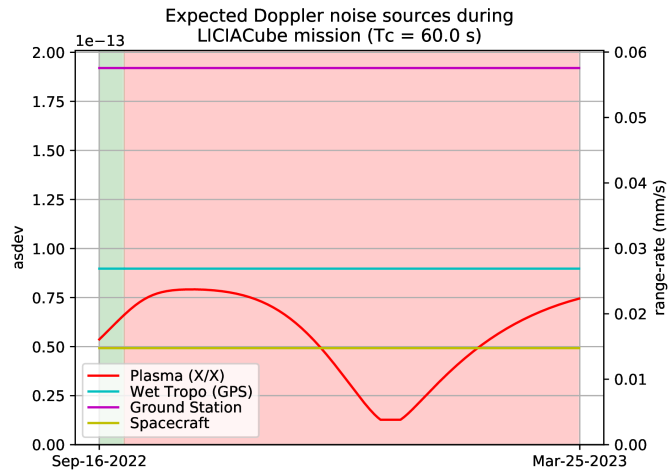
The OPNAV availability is given by the observation timeline of section 2.6.1. Since the distance to the image target, Didymos, is still very large at the epochs the images will be taken, 7 to 3 days before the C/A, the asteroids will not be resolved in any of the images, as they will have sub-pixel size. Additional images will be available during the post-flyby reconstruction, which will also use the scientific observations obtained by pointing the cameras to Dimorphos. In any case, the LEIA pictures are the most relevant to trajectory reconstruction since they provide higher ground resolution. Therefore, the uncertainty level shall be tuned based on the asteroid distance, where the asteroid is said to be resolved if it is larger than a few pixels (e.g. [4] assumed 7 pixels). The pictures provide an angular position of a body relative to the S/C in the camera frame, eventually translated into an inertial frame using attitude. The attitude represents a dominant source of error, about 0.02 deg [58]. To reduce the error, one can use stars in the picture, whose inertial angular position is known very accurately, to get the pointing. However, if the light conditions (due to the albedo or illumination angle) are different between the Didymos and Dimorphos foreground and the background of the stars, they are not visible in the same picture. In this case, one can take multiple images at different exposure to perform the calibration, even though the attitude stability between the acquisitions will degrade the results.

Thus, from the raw images, it will be possible to extract relevant information about Didymos or Dimorphos centroid position and camera attitude. This process involves complex algorithms from external routines and depends on the size of the target on the sensor. The considered error is assumed from the Deep Space 1 mission [8]. For the unresolved asteroids, the centroid-finding algorithms have a typical accuracy of up to 0.1 pixels. However, in the simulations, a conservative value of 0.5 pixels was assumed to consider the lower performance of a camera typical of CubeSats and the larger integration time required for Didymos to be clearly visible. On the other hand, the center finding is no more feasible with the same algorithm for fully resolved asteroid images. Therefore, other algorithms are employed for shapes reconstruction, such as limb fitting or landmarks for closer pictures where the asteroid boundary is not in the image. The uncertainty related to resolved asteroid should account for the distance and the SPA, but the overall contribution can be experimentally determined by the equation [8]:

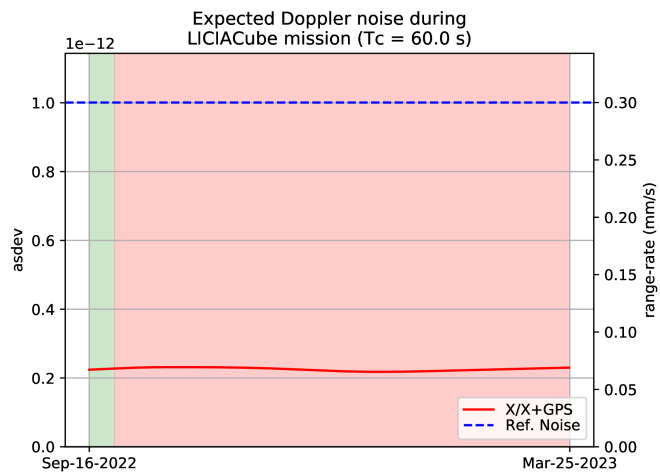
$$\sigma_0 = \frac{\tan^{-1}(R/\rho)}{\alpha} \quad (4.4)$$



(a) LICIAcube mission SEP.



(b) Doppler noise by source during LICIAcube mission.



(c) Doppler noise during LICIAcube mission.

Figure 4.4: LICIAcube mission Doppler noise evaluation.

where  $R$  is the assumed radius of the asteroid,  $\rho$  its range, and  $\alpha = FOV/N_{pxline}$  being FOV the Field of View of the camera, in this case LEIA, and  $N_{pxline}$  the number of pixels in a stripe. All those data are collected in table 2.3.

#### 4.4 Maneuvers execution

Given the lesson learned by the MarCO mission, one of the main concerns for deep space CubeSats is the performance of the propulsion system. The thruster system mounted on LICIACube is from the same manufacturer as the MARCO spacecrafts, and detailed experimental characterization of the execution error and the system reliability is not available. Furthermore, one should also consider that the one-year cruise with the systems off in the DART piggyback dispenser may affect the nominal thruster behavior. The maneuver schedule from table 2.6 is considered to target the C/A conditions and achieve the mission goals.

The maneuver execution of LICIACube spacecraft is not provided only by the axial thrusters. In fact, the Reaction Control System (RCS) thrusters demanded to keep the correct pointing have an unbalanced axial contribution. Therefore, anytime the cold gas RCS is activated, a parasite thrust is generated. The Guidance, Navigation and Control (GNC) takes into account this contribution when computing the thrust time, decreasing the total amount of time required by the axial thrusters by the amount provided by the RCS axial contribution. For this reason, a very detailed propulsion and attitude control systems characterization are required for an accurate maneuver calculation.

The maneuvers are not perfectly performed, so they are estimated as part of the OD process. However, due to limited observability, not all components can be estimated. Thus, it is important to start the estimation from the expected most accurate values, either from *a priori* models or telemetry. Moreover, accurate *a priori* uncertainties must be used to limit the unobservability issue. In order to provide consistent and robust results, a conservative maneuver execution error model has been adopted in the form of the so-called Gates model [63]. This latter accounts for magnitude and pointing errors, each composed of a fixed and a proportional part. The contribution to errors has been considered step-wise since a fixed contribution is applied only to maneuvers under a minimum  $\Delta V$ . Thus, the pointing error can be summarized as:

$$\alpha = \sqrt{\sigma_\alpha^2 + \rho_\alpha^2 |\Delta \mathbf{v}|^2} \quad (4.5)$$

and the magnitude error as:

$$\beta = \sqrt{\sigma_\beta^2 + \rho_\beta^2 |\Delta \mathbf{v}|^2} \quad (4.6)$$

where  $\alpha$  and  $\beta$  are the pointing and magnitude error sigmas respectively, while  $\sigma$  and  $\rho$  represent the fixed and proportional magnitude error contribution of their subscript components. The defined execution error may be projected in the three components, as depicted in figure 4.5. Given three independent random realization  $\zeta_1$ ,  $\zeta_2$ , and  $\zeta_3$ , of a normal distribution  $N(0, 1)$ , the maneuver error can be described as:

$$\mathbf{e} = \alpha \cdot \zeta_1 \cdot \hat{\mathbf{e}}_x + \alpha \cdot \zeta_2 \cdot \hat{\mathbf{e}}_y + \beta \cdot \zeta_3 \cdot \hat{\mathbf{e}}_z \quad (4.7)$$

being  $\hat{\mathbf{e}}_z$  in the nominal maneuver direction,  $\hat{\mathbf{e}}_x$  and  $\hat{\mathbf{e}}_y$  perpendicular to the nominal maneuver.

For the LICIACube mission, Gates model coefficients have been set conservative values, and an additional time execution error is also assumed. The values used for the

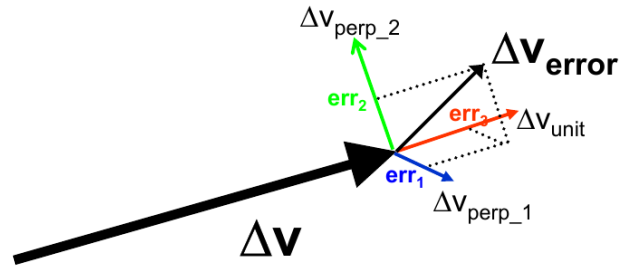


Figure 4.5: Gates error representation. Source: Monte 149 help guide - JPL, Caltech.

Table 4.1: Gates and time execution error model  $1\sigma$  coefficients.

$\Delta V = 0.0$ m/s	Time	(sec)	3.0
	Magnitude	Proportional (%)	0
		Fixed(m/s)	0.011
	Pointing	Proportional (%)	0
Fixed(deg)		spherical	
$\Delta V > 0.0$ m/s	Time	(sec)	3.0
	Magnitude	Proportional (%)	10
		Fixed(m/s)	0
	Pointing	Proportional (%)	0
Fixed(deg)		1.1	

maneuvers errors are reported in table 4.1. Since the release have been modeled as an impulsive maneuver, also its uncertainty have been computed with a similar model. These coefficients retrieved from the dispenser manufacturer are in table 4.2. In this case, the

Table 4.2: Gates and time release error model  $1\sigma$  coefficients.

Release	Time	(sec)	30.0
	Magnitude	Proportional (%)	0
		Fixed(m/s)	0.07
	Pointing	Proportional (%)	0
Fixed(deg)		2.0	

time uncertainty does not come from any hardware specification but has been assumed from practical consideration of possible DART timeline shift which may delay or anticipate the release of LICIAcube. Nonetheless, the a-posteriori reconstructed date of release will be affected by a lower time uncertainty level (in the order of 1 second), thus the assumed value provides conservative results.

## 4.5 Parameters

The OD filter setup uses a set of parameters that includes the spacecraft state, the asteroids state and gravity, the maneuvers, and observables additional data. The full set of parameters is reported in tables 4.3, 4.4 and 4.5, respectively for estimated (nominal and backup releases), and considered parameters. The *a priori* uncertainties of the estimated

parameters were already described in the previous chapter. Note that full covariance matrices are used for both the spacecraft and the Didymos Barycenter states. Regarding the considered parameters, their assumed *a priori* uncertainties come from [5]. The stochastic was already described in section 3.5.6 and its value is assumed high to account for the general lower performance of CubeSats.

## 4.6 Baseline results

At first, the estimation of the baseline selected to achieve the LICIACube mission goals has been assessed. This process was iteratively done for each proposed baseline to corroborate the MA propagation and to validate the selected trajectory. The validation was performed by retrieving the attainable OD accuracy and includes the check of the requirements compliance and the analysis of the propellant required. This section presents the results for the two selected scenarios, nominal and contingency probe release.

The baseline trajectory shows a flyby occurring at 51.1 km from Dimorphos, 166.9 seconds after the DART impact, with a minimal variation between the nominal and backup release cases. Tables 4.6 and 4.7 summarize the expected  $3\sigma$  uncertainties in the B-plane coordinates obtained using the delivery DCO, for nominal and backup releases. The results satisfy the C/A distance and time requirements because the coordinates are within the required limits, taking into account the  $3\sigma$  uncertainty. In addition, the results are reported also in the Dimorphos RTN frame, centered in Dimorphos and defined as:

$$\begin{aligned}\hat{\mathbf{R}} &= \frac{\mathbf{r}}{|\mathbf{r}|} \\ \hat{\mathbf{N}} &= \frac{\mathbf{r} \times \mathbf{v}}{|\mathbf{r} \times \mathbf{v}|} \\ \hat{\mathbf{T}} &= \hat{\mathbf{N}} \times \hat{\mathbf{R}}\end{aligned}\tag{4.8}$$

where  $\mathbf{r}$  and  $\mathbf{v}$  are the spacecraft radial position and relative velocity with respect to Dimorphos, respectively.

Nonetheless, more immediate and clearer information are provided by the figures generated by the OD report tool developed for this dissertation and useful to support OD approval process described in chapter 6. First, from the spacecraft uncertainty in the B-plane (figure 4.6) it is immediate to verify the distance requirement compliance and the ellipse parameters evolution. After the OM1 DCO, the semi-minor axis of the uncertainty drops, and becomes almost aligned with the radial direction, thus providing robustness for the distance verification. In particular, the OM2 DCO provides a dramatic improvement of the S/C uncertainty. This could be better seen in figure 4.7 depicting the continuous evolution of the B-plane ellipses parameters. It shows a dramatically decreasing uncertainty in the occurrence of the maneuvers, precisely at the following pass, when data acquired managed to tear down the maneuver execution error. Hence, it is of primary importance to provide trajectory reconstructions including post-maneuver data.

The verification of the entire mission pointing from DSN toward the spacecraft is presented in figure 4.8. The picture shows the evolution of the DSN to probe pointing uncertainty versus the mission time (x-axis), subject to monthly updates of the trajectory based on their respective DCOs (dashed vertical cyan lines). The sawtooth behavior is due to the uncertainty propagation increasing between periodical OD updates, which tear down the uncertainty. During the leaving phase the DCO is assumed one week before the correspondent delivery.

Table 4.3: Filter nominal setup for estimated parameters, for nominal release.

Parameter	Unit	A-priori $1\sigma$ uncertainty	Comments
<i>Spacecraft state</i>			
Position	km	4.9 / 7.2 / 3.9	Full covariance matrix in EME2000.
Velocity	mm/sec	4.1 / 3.1 / 3.5	
<i>Didymos Barycenter state</i>			
DMW	rad	7.2e-7	Full covariance matrix in Brouwer-Clemence set III parameters.
DP	rad	5.5e-7	
DQ	rad	4.0e-7	
EDW	rad	8.0e-7	
DA	-	3.1e-9	
DE	-	3.7e-9	
<i>Dimorphos state</i>			
Position	km	4.0e-2	
Velocity	mm/sec	6.0	
<i>Didymos Asteroid GMs</i>			
Didymos	km <sup>3</sup> /sec <sup>2</sup>	2.8e-9	
Dimorphos	km <sup>3</sup> /sec <sup>2</sup>	5.5e-11	
<i>Release maneuver</i>			
$\Delta V$	m/s	0.07	
Ra	deg	2.0	
Dec	deg	2.0	
$\Delta t$	sec	30.0	
<i>Deterministic burns (CM1, OM1)</i>			
$\Delta V$	m/s	10%	
Ra	deg	1.1	
Dec	deg	1.1	
$\Delta t$	sec	3.0	
<i>Statistical burns (OM2, OM3)</i>			
$\Delta V_x / \Delta V_y / \Delta V_z$	m/s	0.011	
$\Delta t$	sec	3.0	
<i>Observables bias</i>			
Range bias	m	15	Constant per pass
<i>Stochastic accelerations</i>			
Sigma	km/sec <sup>2</sup>	1.e-11	Stochastic, assumed from [5] $\times 20$
Time batch	sec	24 hours	

Table 4.4: Filter nominal setup for estimated parameters, for backup release, for spacecraft and Didymos Barycenter state only. All other parameters are assumed equal to table 4.3.

Parameter	Unit	A-priori $1\sigma$ uncertainty	Comments
<i>Spacecraft state</i>			
Position	km	8.8 / 10.1 / 7.1	Full covariance matrix in EME2000.
Velocity	mm/sec	21.5 / 21.7 / 20.1	
<i>Didymos Barycenter state</i>			
DMW	rad	6.9e-7	Full covariance matrix in Brouwer-Clemence set III parameters.
DP	rad	4.9e-7	
DQ	rad	3.8e-7	
EDW	rad	8.0e-7	
DA	-	3.1e-9	
DE	-	3.6e-9	

Table 4.5: Filter nominal setup for considered parameters.

Parameter	Unit	A-priori $1\sigma$ uncertainty	Comments
<i>SRP</i>			
Scale Factor	-	3%	
<i>Station locations</i>			
DSN station locations	cm	2-5	Assumed from [5]
<i>Troposphere path delay</i>			
Wet	cm	1.0	Assumed from [5]
Dry	cm	1.0	
<i>Ionosphere path delay X-band</i>			
Day	cm	5.0	Assumed from [5]
Night	cm	1.0	
<i>Earth Orientation Parameters</i>			
Motion	cm	10.0	Assumed from [5]
UT1 Bias	sec	2.5e-4	

Table 4.6: Expected accuracy of the LICIAcube state with respect to Dimorphos at C/A, for nominal release. Results are computed at delivery DCO, both in B-plane and Dimorphos RTN reference frames. All uncertainties are at  $3\sigma$ .

Parameter	Nominal value	$3\sigma$ unc.	Normalized unc.
B.R	-42.1 km	9.5 km	22.6%
B.T	29.1 km	10.5 km	36.1%
LTOF	0.0 sec	3.3 s	-
R	51.2 km	4.7 km	9.1%
T	0.0 km	20.5 km	-
N	0.0 km	13.4 km	-

Table 4.7: Expected accuracy of the LICIACube state with respect to Dimorphos at C/A, for backup release. Results are computed at delivery DCO, both in B-plane and Dimorphos RTN reference frames. All uncertainties are at  $3\sigma$ .

Parameter	Nominal value	$3\sigma$ unc.	Normalized unc.
B.R	-42.1 km	12.0 km	28.6%
B.T	29.1 km	13.9 km	47.5%
LTOF	0.0 sec	5.6 s	-
R	51.2 km	4.5 km	8.8%
T	0.0 km	34.4 km	-
N	0.0 km	17.8 km	-

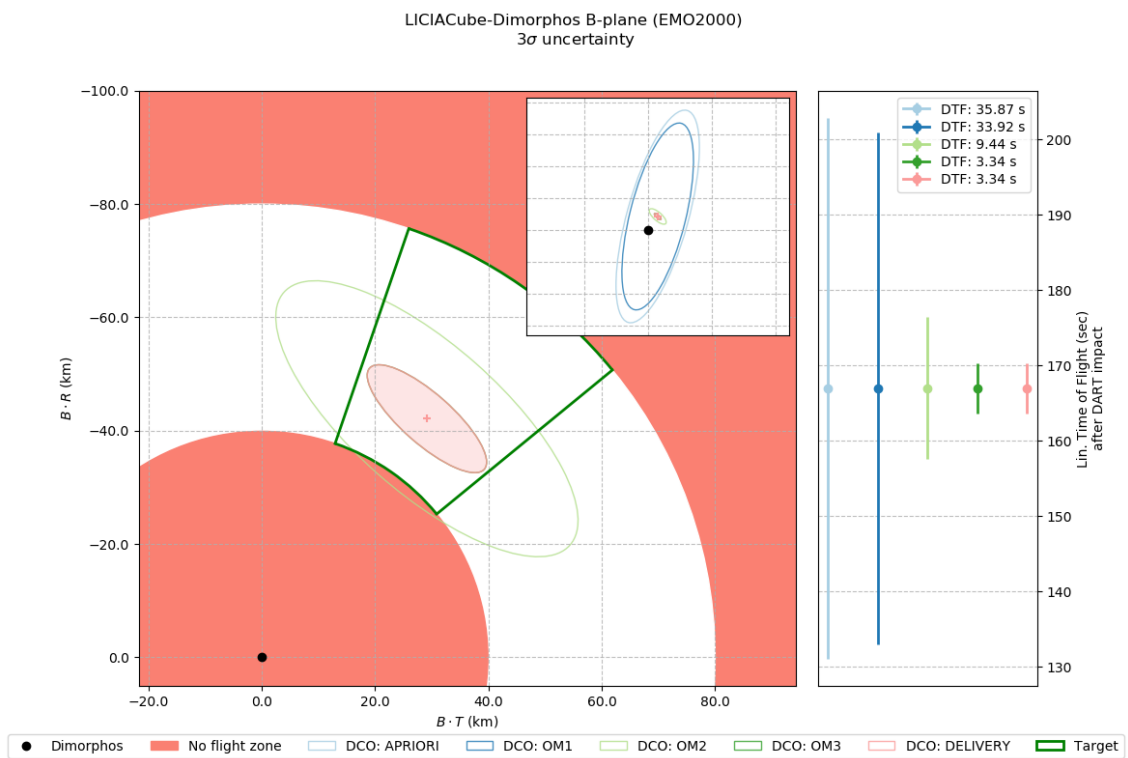


Figure 4.6: Expected spacecraft B-plane uncertainty ( $3\sigma$ ) against DCO, for baseline setup assuming nominal release.

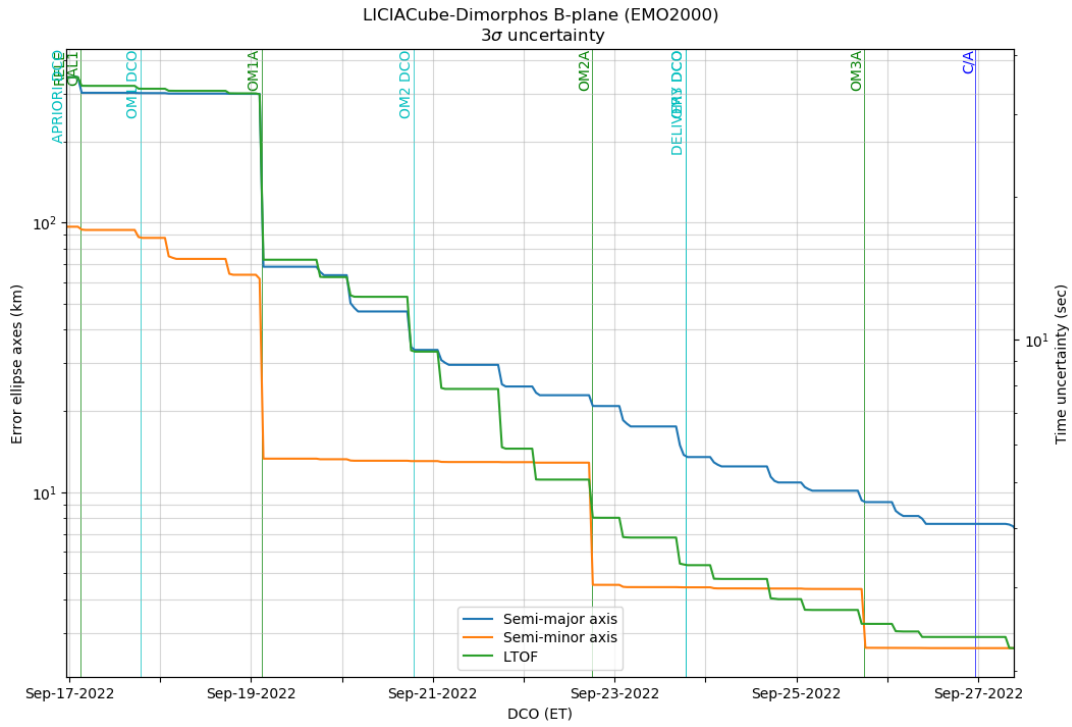


Figure 4.7: Expected B-plane parameters uncertainty evolution ( $3\sigma$ ) with respect to DCO, for baseline setup assuming nominal release.

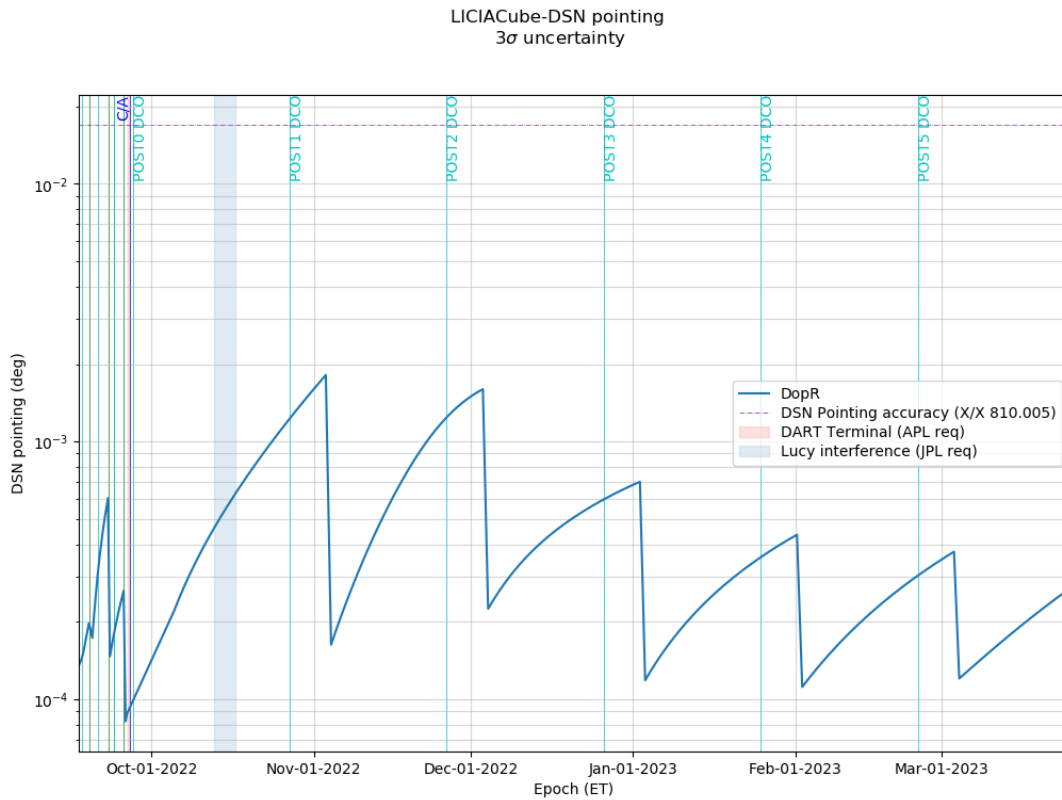


Figure 4.8: Expected DSN pointing uncertainty ( $3\sigma$ ), for baseline setup assuming nominal release.

The SPA analysis is presented in figure 4.9. This angle uncertainty at  $3\sigma$  is slightly out of the boundaries at the C/A predicted epoch. Also, one may note the steepness of the SPA variation in the neighborhood of the C/A, caused by the high angular velocity of the flyby because of the high velocity and the radius variation. Although, only a little can be done to correct the C/A value of the SPA, which strongly depends on the system dynamics and the flyby distance. Increasing the distance would reduce the variability of the SPA (namely the slope of the curve at the flyby), but the science team decided to prioritize the ground resolution, accepting a violation of the requirement.

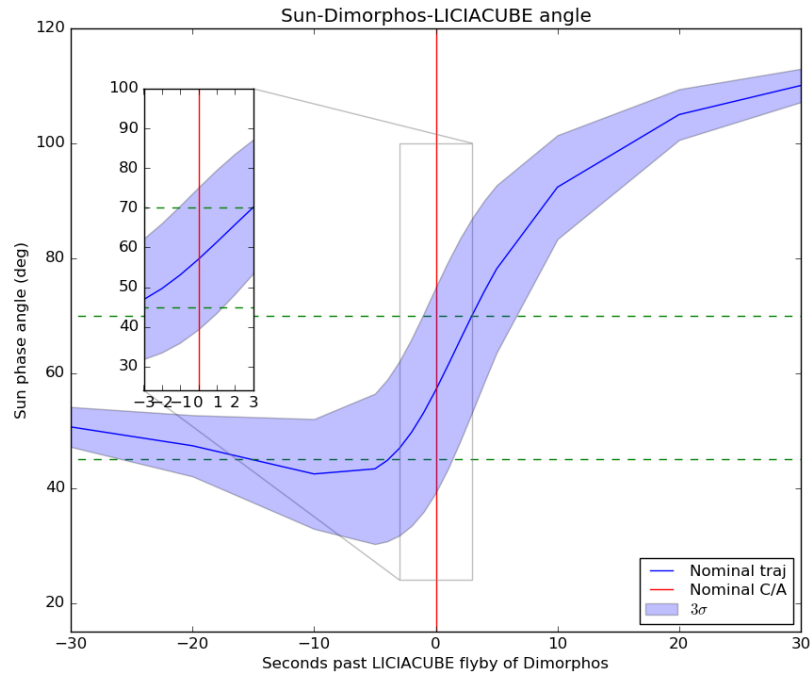


Figure 4.9: Expected SPA uncertainty ( $3\sigma$ ) at delivery DCO, for baseline setup assuming nominal release.

Finally, the LEIA pointing uncertainty result in figure 4.10 provides a straightforward proof of the compliance to the requirement RQ4100.002, as the delivery DCO used for the update of the camera pointing for the final acquisition produces an uncertainty ellipse fully inside the camera FOV.

Similar considerations could be made on the contingency release case. Once again, the B-plane results in figure 4.11 bring to the conclusion that the correct distance can be achieved from Dimorphos. Also, the time uncertainty is still in the limit of 200 s from DART impact, with a large margin.

The same comments about the B-plane parameters evolution of the nominal release case hold for the backup one, reported in figure 4.12.

Moreover, the verification of the DSN pointing toward the spacecraft is reported in figure 4.13 restricted to the approach phase, which presents a pointing uncertainty larger than the nominal case, although widely below the limit.

The SPA in figure 4.14 shows a much larger amplitude of the uncertainty, thus a wider range of possible values outside the limits. Nonetheless, the project accepted the non-compliance, preferring to keep the same flyby distance at the C/A.

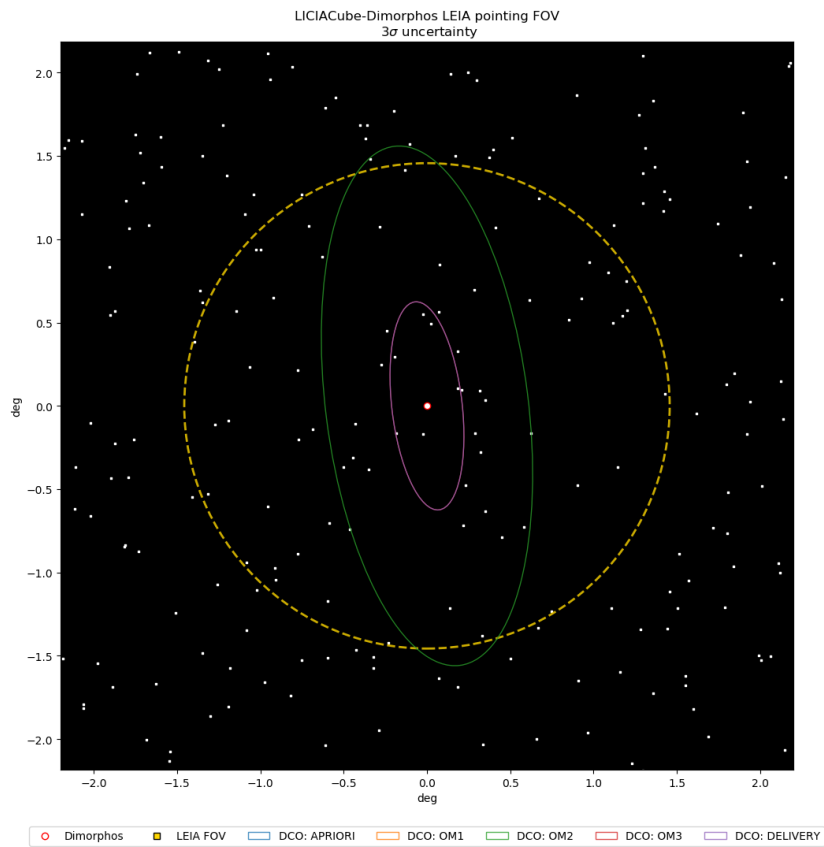


Figure 4.10: Expected LEIA camera locking FOV uncertainty ( $3\sigma$ ), for baseline setup assuming nominal release. To be conservative, the FOV is assumed circular as the roll angle is unknown.

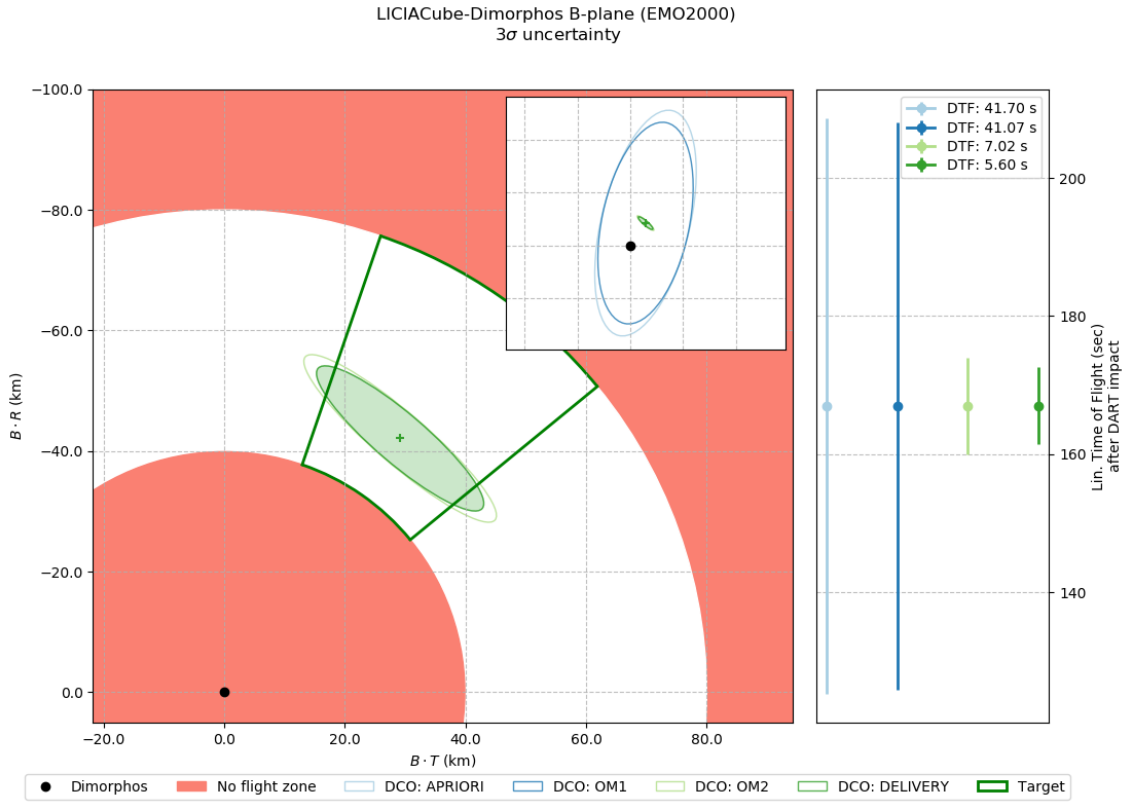


Figure 4.11: Expected spacecraft B-plane formal uncertainty ( $3\sigma$ ) against DCO, for baseline setup assuming backup release.

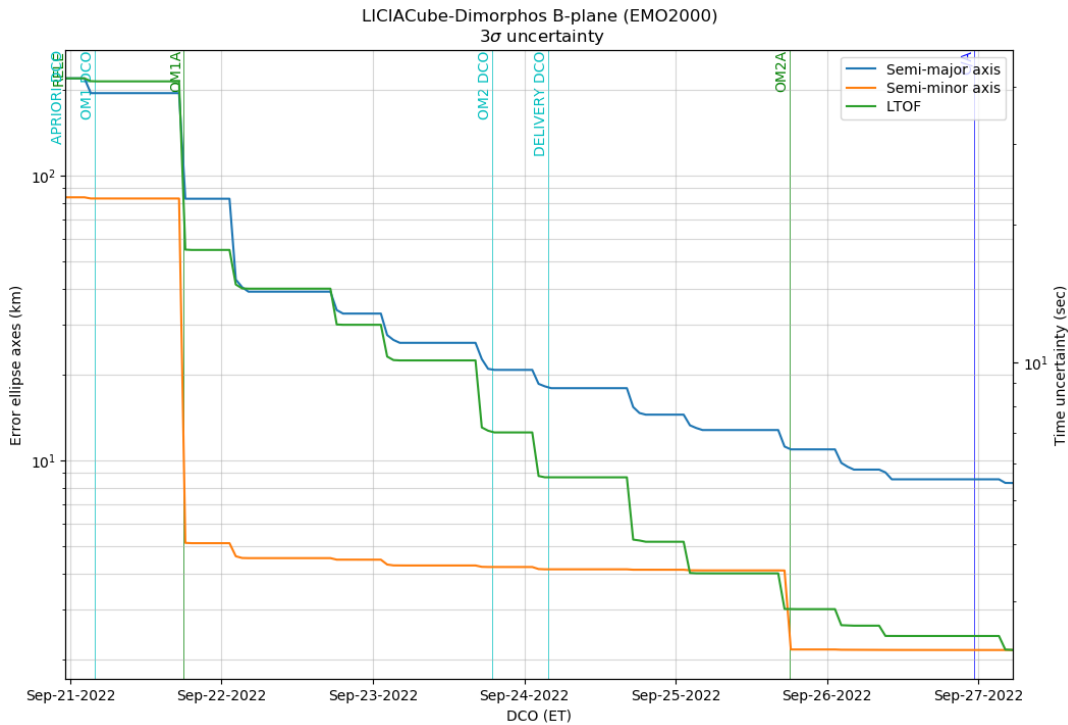


Figure 4.12: Expected B-plane parameters uncertainty evolution ( $3\sigma$ ) with respect to DCO, for baseline setup assuming backup release.

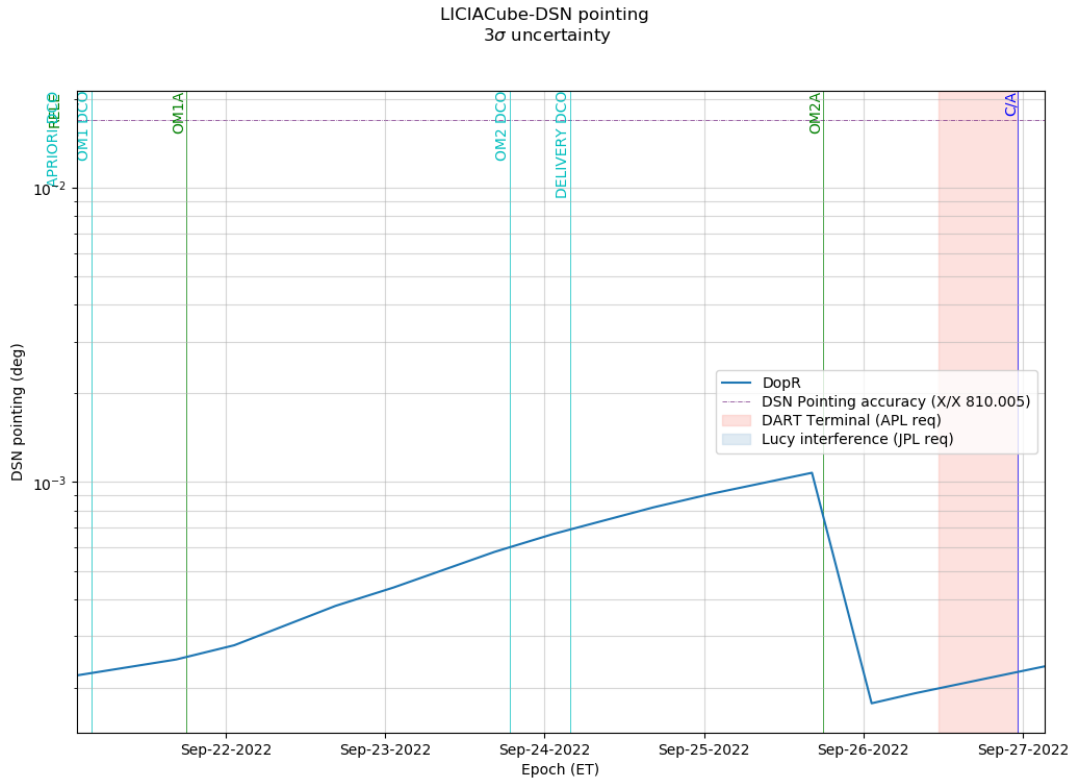


Figure 4.13: Expected DSN pointing uncertainty ( $3\sigma$ ), for baseline setup assuming backup release.

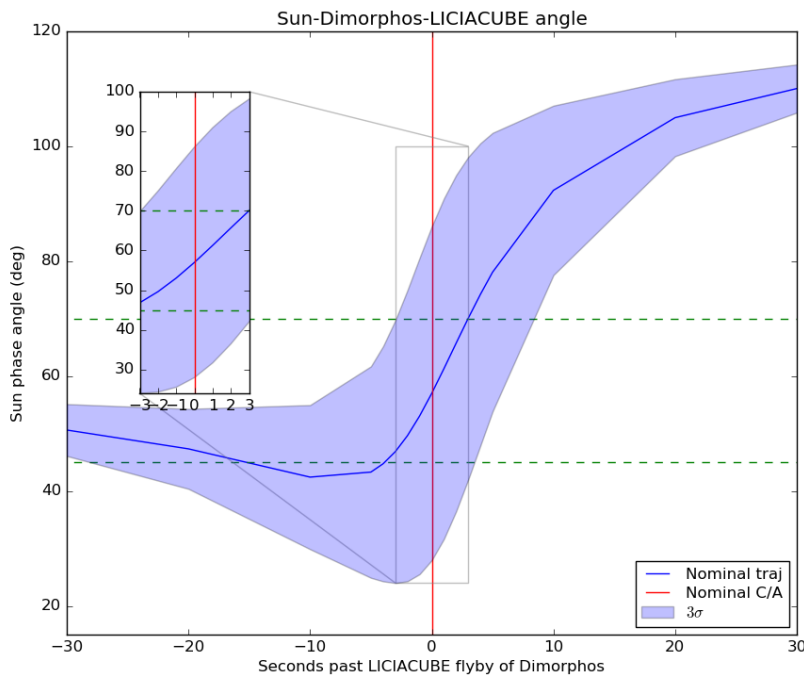


Figure 4.14: Expected SPA uncertainty ( $3\sigma$ ) at delivery DCO, for baseline setup assuming backup release.

The camera pointing in figure 4.15 shows compliance with the requirements occurring for the last two DCOs (OM2 and delivery). It is worth recalling that these DCOs are different in the backup case.

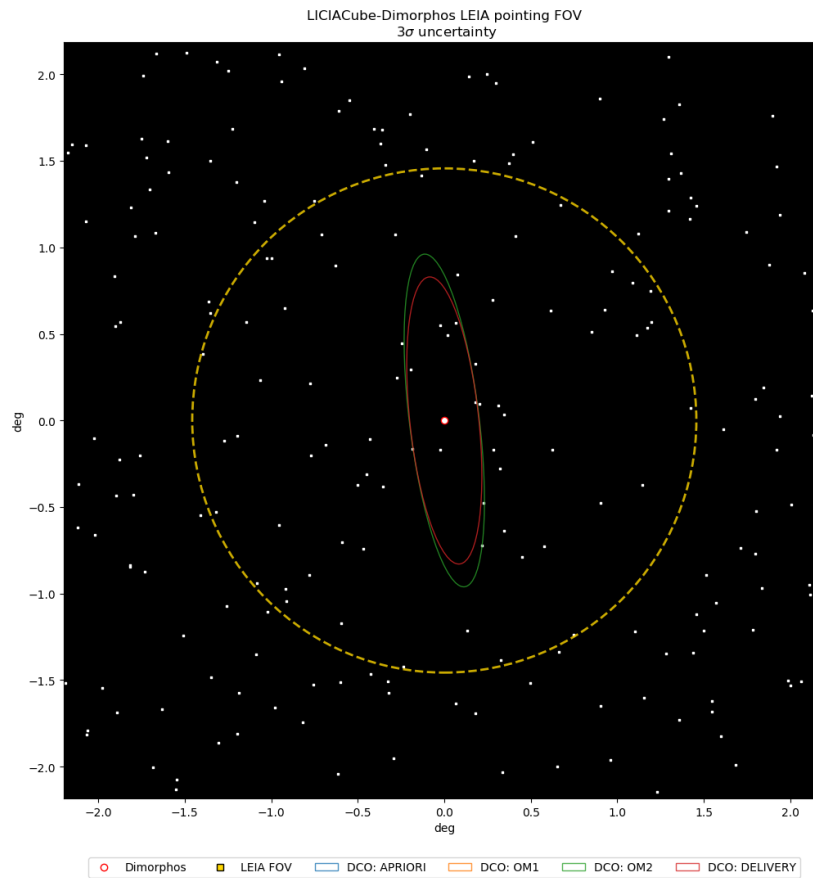


Figure 4.15: Expected LEIA camera locking FOV uncertainty ( $3\sigma$ ), for baseline setup assuming backup release. To be conservative, the FOV is assumed circular as the roll angle is unknown.

In general, one may notice that the performances for backup release are worse than the nominal one, still being within limits, except for the SPA. Considerations shall be made on this observation. First, the backup release only represents a contingency condition, thus a second (and last) chance to deploy the CubeSat before DART, and everything in it - including LICIACube, if not released - goes destroyed in the impact. Therefore it may be concluded that worse performance can be accepted for contingency release, still fulfilling most of the requirements. Furthermore, the decrease in performance does not represent a harmful condition since the safety requirements for the spacecraft are still verified with margins. The worsening of the results may be attributed to the shorter approach phase, which provides less radio-tracking data collected to reconstruct the trajectory, thus increasing the reconstruction uncertainty.

## 4.7 Robustness analysis

The robustness analysis is an extended evaluation of the achievable performances in case of modified assumptions of the values of the parameters. This analysis is of primary

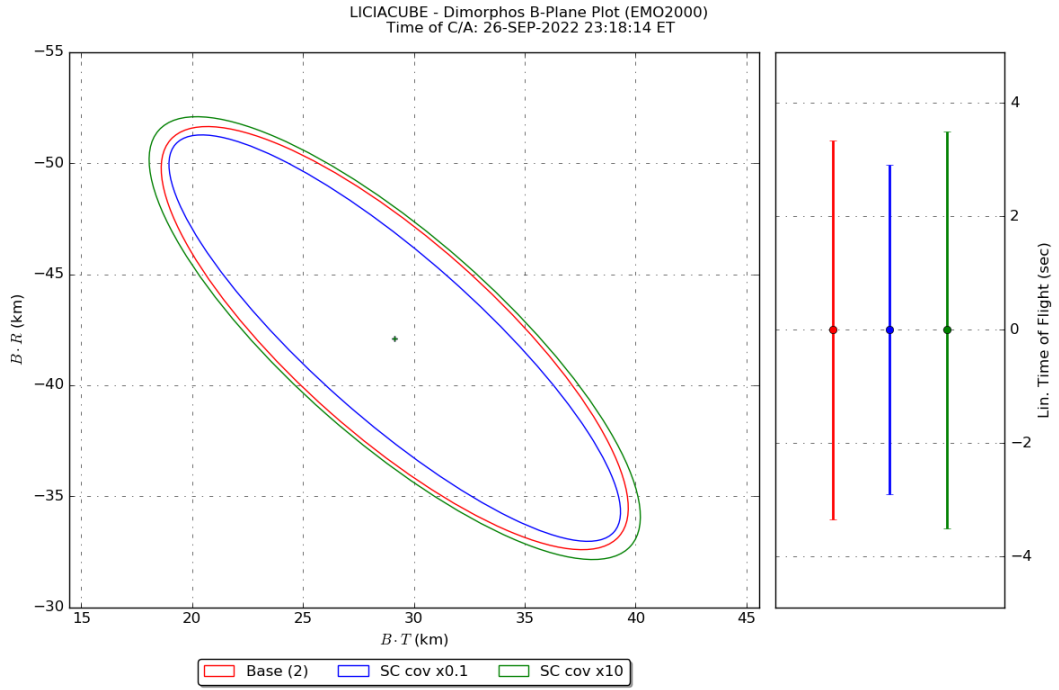
importance to test the sensitivity of the results to the different parameters. During the mission analysis, a high sensitivity to the component-related parameters may be solved requiring to the manufacturer a deeper characterization of hardware components. Instead, pre-operations robustness analysis investigates possible divergence sources if nominal values or uncertainties are computed to be different from the assumed ones. In general, each parameter may have a different effect on the final results, and its influence could be recognized during operations in case of particular signatures of data or an unexpected variation in the obtained reconstruction. In the following, the sensitivity to the main parameters is analyzed and the results are discussed.

#### 4.7.1 A-priori covariance

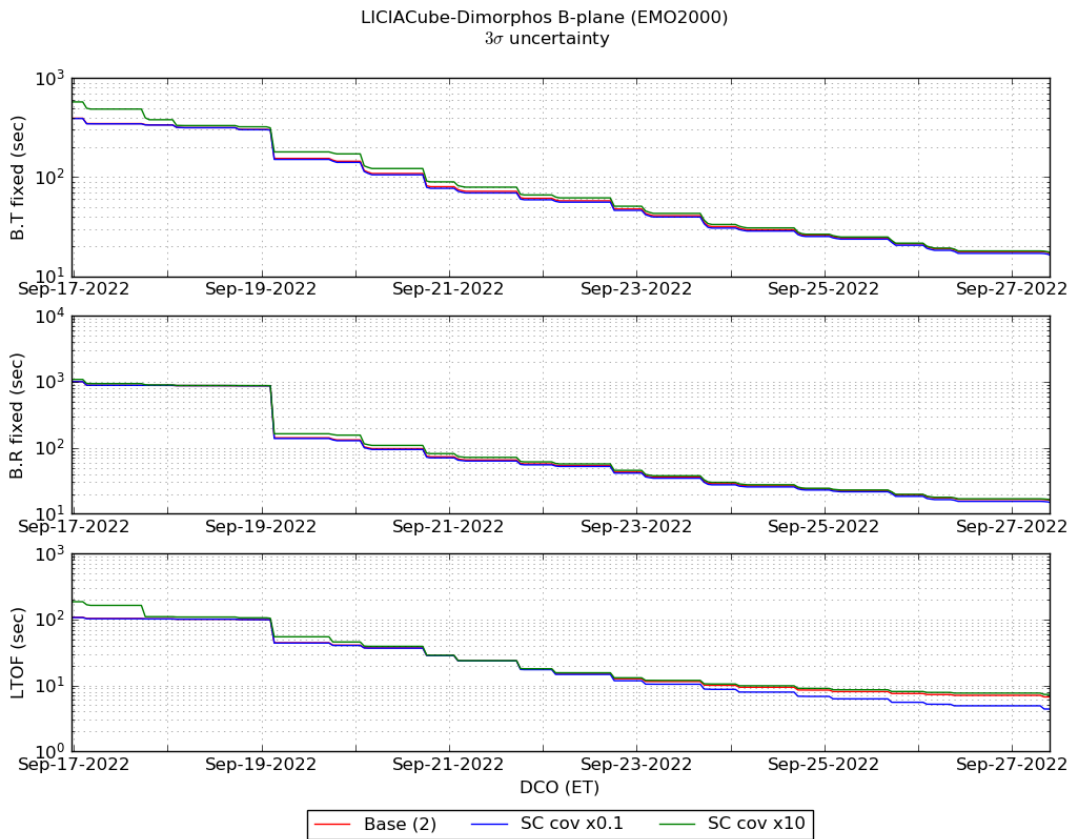
**Spacecraft** The nominal *a priori* uncertainty comes from the simulations of the Jet Propulsion Laboratory (JPL) DART NAV team, as a full covariance matrix. The covariance matrix scaled by a safety factor of 2, is considered for LICIACube before the release, as it is rigidly fixed on the main probe. The robustness analyses account for scaling of this base factor both downward and upward of a factor of 10, namely obtaining 0.2 and 20 times the values provided by the DART team. The results are presented in figure 4.16 as B-plane ellipses computed at the delivery DCO, and the evolution of the B-plane parameters. The main contribution of inflating the S/C initial uncertainty is to weakly scale its B-plane uncertainty at the C/A, both for the in-plane and time components. It is also worth noting that reducing the scale factor provides a more significant effect only on the time, meaning that inflating the uncertainty over a specific limit is well absorbed by the filter estimation provided by data collection during the first part of the mission. This behavior is clear from the figure 4.16b, where the initial larger uncertainty quickly converges to the nominal value.

**Didymos Barycenter** As the radiometric observables provide information with respect to the Earth, the position relative to Didymos is computed from its ephemerides. Hence, the effects of the ephemerides uncertainties are evaluated on the delivery DCO formal uncertainty of the probe. As expected, it shows a considerable effect on the B-plane results, as shown in figure 4.17. Since the available observables do not allow us to estimate Didymos, we cannot improve its *a priori* uncertainty. Accumulating measurements, the uncertainty in the relative position decreases reaching a plateau, and the Didymos Barycenter covariance becomes dominant. Figure 4.17b shows that by increasing the covariance, the uncertainties increase significantly, whereas by reducing it, the decrease in the uncertainties is much limited in  $B \cdot R$  and  $B \cdot T$ , larger in LTOF. It can be concluded that the LTOF is always dominated by the Didymos covariance, while the effects on  $B \cdot R$  and  $B \cdot T$  are significant but not dominant.

**Maneuvers** Some relevant information could be also provided by the analysis of the time uncertainty and the Gates model applied to the maneuvers execution error, for all the maneuvers. A study has been performed by scaling, by a factor of 10 and 0.1, the set of maneuvers error. The sensitivity to these parameters is presented in figure 4.18. Once again, deflating the uncertainty does not significantly improve the B-plane results because other effects are dominant (most likely the Didymos covariance). Conversely, inflating all the maneuvers errors will result in considerably larger final uncertainty in both in-plane and time, which becomes not compliant with the mission requirements. From the B-plane ellipse parameters evolution in figure 4.18b it is straightforward to notice that the larger

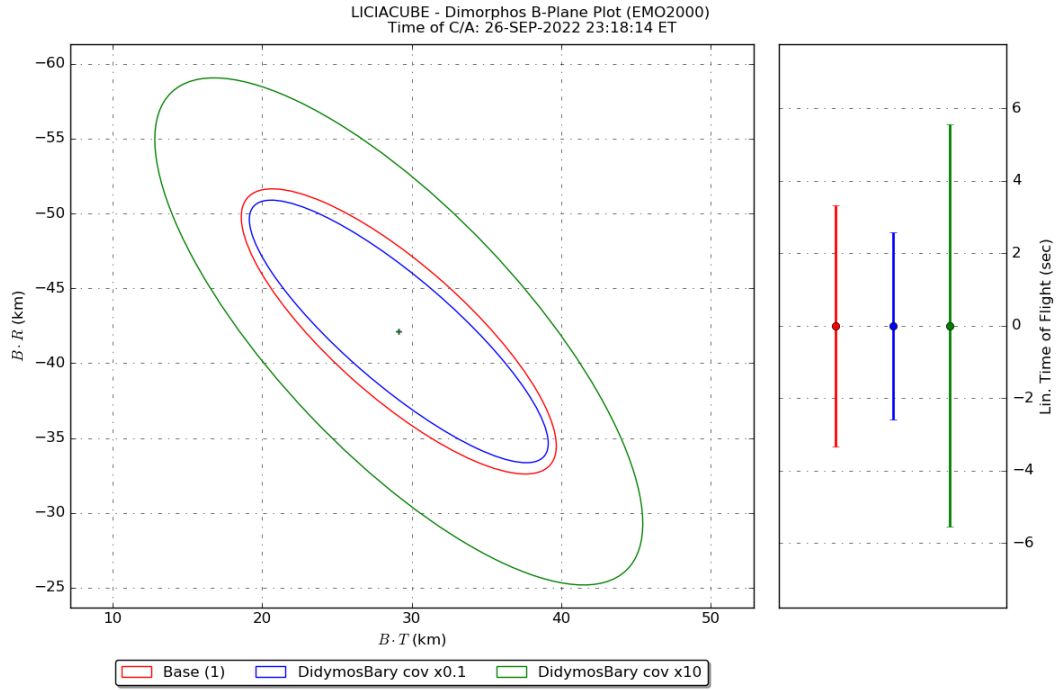


(a) *S/C B-plane uncertainty at delivery DCO.*

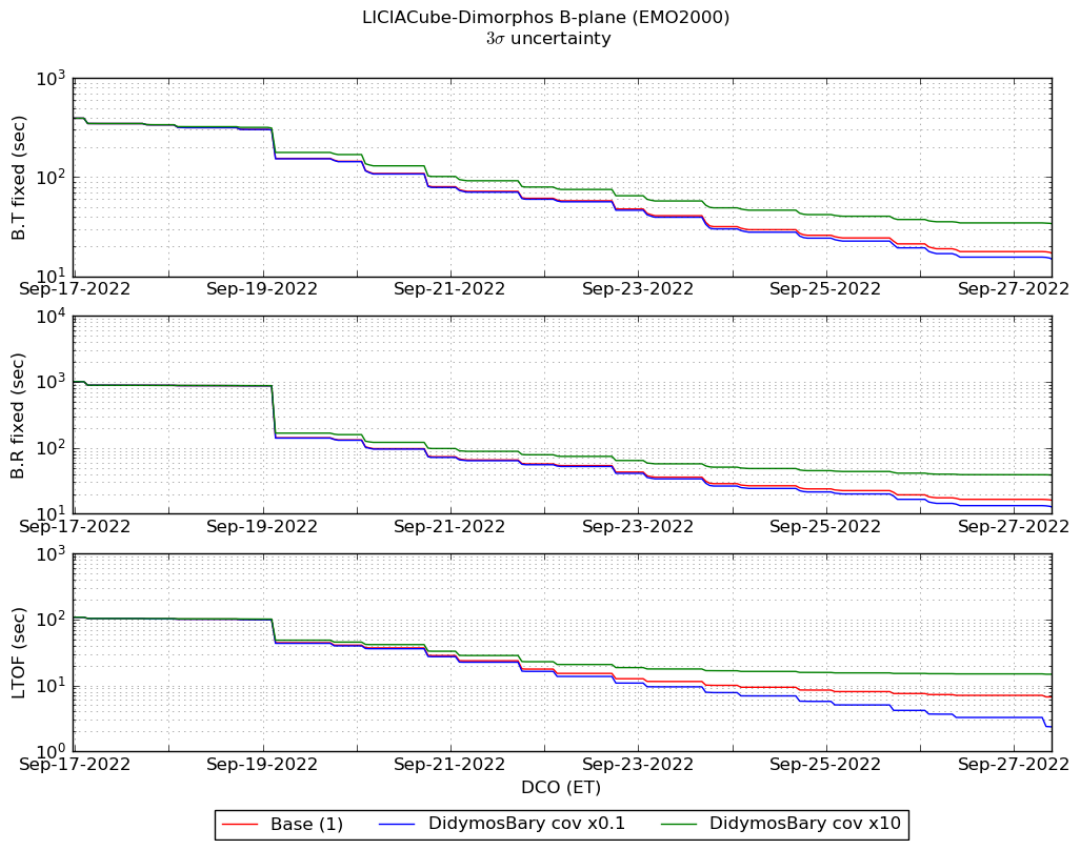


(b) *B-plane parameters evolution.*

Figure 4.16: OD results against the DART probe's covariance scale factor.

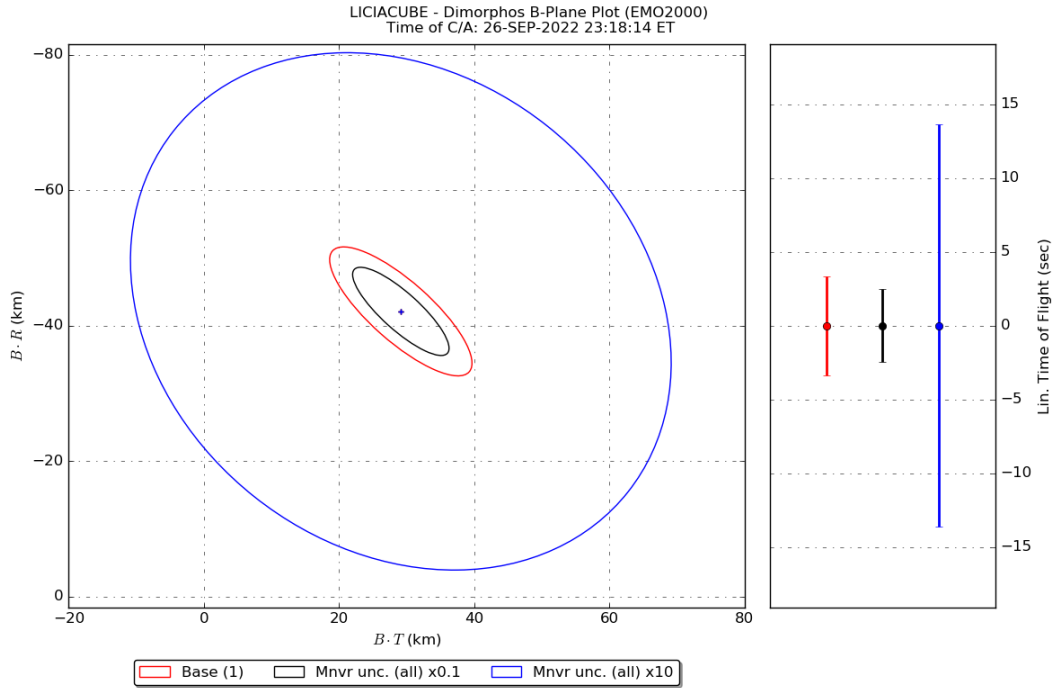


(a) *S/C B-plane uncertainty at delivery DCO.*

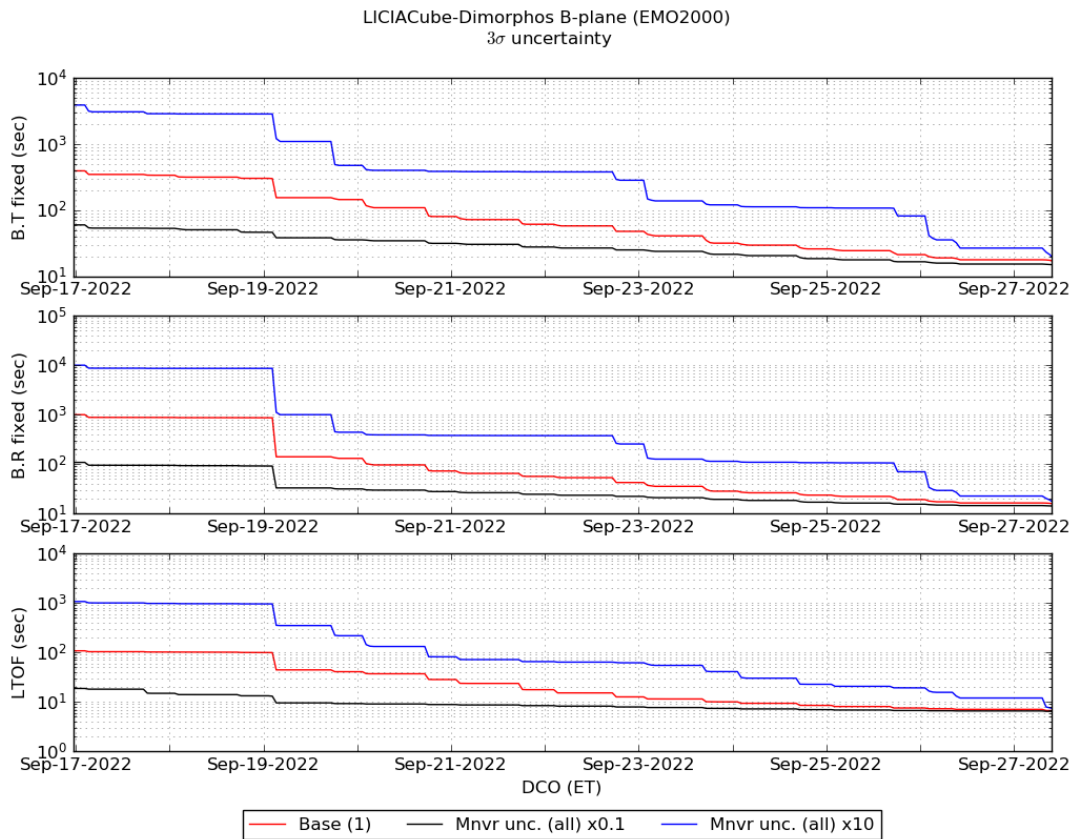


(b) *B-plane parameters evolution.*

Figure 4.17: OD results against the Didymos Barycenter covariance scale factor.



(a) S/C B-plane uncertainty at delivery DCO.



(b) B-plane parameters evolution.

Figure 4.18: OD results against the maneuvers execution error scale factor.

initial deviation of the three compared cases, due to maneuvers, is absorbed gradually in time, thanks to the data received after each maneuver is performed. Thus, the inflated uncertainty of a maneuver is mainly visible at DCO occurring before the maneuver itself but is reduced by the post-execution data acquisition. The B-plane parameters gradually converge to their base case values over time. Unfortunately, inflating too much the model uncertainty, the OD is not able to guarantee that the uncertainty drops to the base value at the delivery DCO.

Therefore, a deeper insight may be beneficial to understand which maneuvers may be more critical to the OD achievable performance. To this investigation, only one maneuver execution error is changed at any time, while the others are kept fixed to the nominal values. The obtained results are presented in figure 4.19. As one may expect, in the beginning, the largest contribution is provided by inflating either the release or the OM1 uncertainties, which are more relevant due to their larger value. Nonetheless, as already explained, the uncertainty dramatically drops after the post-maneuver acquisitions, thus providing results similar to the base case.

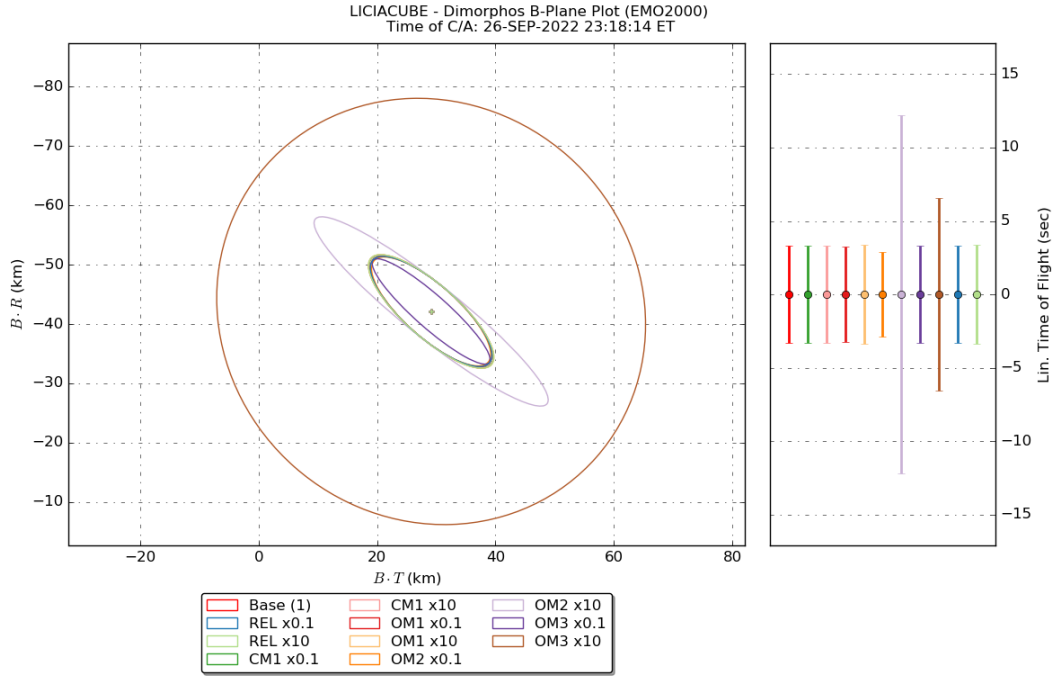
Conversely, the stochastic maneuvers OM2 and OM3 are much closer to the final delivery DCO. As a result, from the B-plane it is clear that, should the *a priori* uncertainty of those maneuvers be increased, the acquired data will not be able to drive the spacecraft uncertainty to converge to the base case before the delivery DCO both for OM2 and OM3. OM2 strongly affects the transversal component and the time uncertainties. On the other hand, inflating OM3 provides almost a spherical uncertainty, as the maneuver execution error will dominate the base uncertainty.

**Summary** To conclude the robustness analysis results with respect to the *a priori* covariances, table 4.8 is filled with the obtained values for the flyby uncertainty of LICIACube with respect to Dimorphos. Each test has been obtained dividing or multiplying the base result by a scale factor of ten.

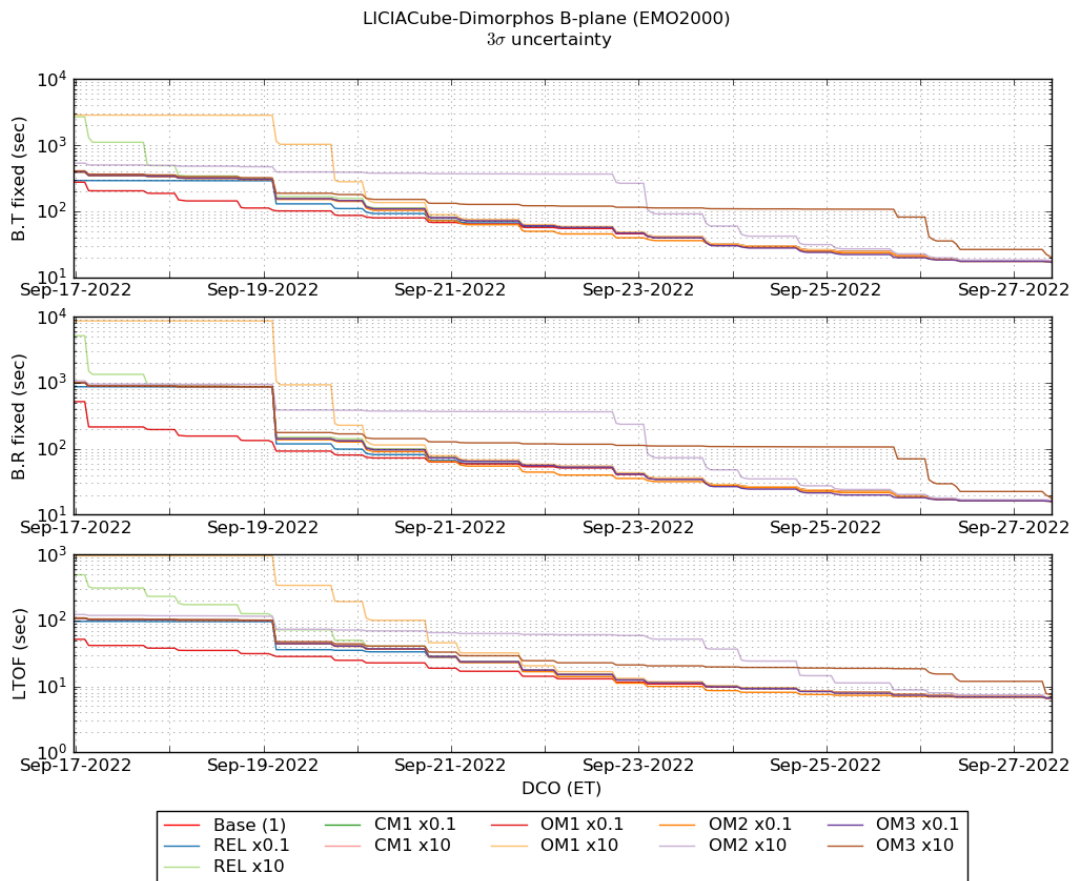
By comparing each case to the base one, the following conclusions could be reached:

- the initial S/C covariance and the maneuvers uncertainty of the release, CM1, and OM1 have limited effects on the final B-plane uncertainty;
- the Didymos Barycenter *a priori* covariance significantly affects the reconstructed trajectory achievable accuracy, especially in time. Possible mitigation actions include the implementation of the optical observables to constrain the asteroids' state directly to the spacecraft;
- the OM2 and OM3 maneuvers provide the largest contribution to the B-plane uncertainty since a low amount of radio-tracking is collected between their execution and the last DCO (OM3 is even after the delivery DCO). Thus, inflating their *a priori* uncertainty can be barely mitigated by OD reconstruction before the flyby. However, the baseline execution error model is deemed sufficiently conservative.

Additional observations can be done considering the RTN components' uncertainties. The B-plane  $\hat{r}$  is the radial vector joining Dimorphos to the spacecraft,  $\hat{t}$  is aligned with the probe's velocity, thus perpendicular to the B-plane, and  $\hat{n}$  can be seen on the B-plane as the direction perpendicular to the radius. Hence, R provides information on the C/A distance, T is related to the LTOF, and N is geometrically scaled with the radial distance to obtain the clock angle excursion. To provide a comprehensive view of the requirements' compliance, figure 4.20 depicts the computed data compared to the constraints. Given that the SPA constraint is exceeded even in the nominal case, it is straightforward to



(a) S/C B-plane uncertainty at delivery DCO.



(b) B-plane parameters evolution.

Figure 4.19: OD results against the decoupled maneuvers execution error scale factor.

Table 4.8: Robustness analysis results, with uncertainties comparison computed at delivery DCO, both in B-plane and Dimorphos RTN reference frames. Scale factors are respect to the base case. The cases where at least one requirement (in addition to SPA) is not fulfilled are highlighted in red.

Case	scale	$3\sigma$ uncertainty					
		B.T (km)	B.R (km)	LTOF (s)	R (km)	T (km)	N (km)
Base		10.5	9.5	3.3	4.7	20.5	13.4
S/C cov	0.1	10.2	9.2	2.9	4.0	17.8	13.1
	10	11.1	10.0	3.5	4.9	21.5	14.1
Didymos Barycenter cov	0.1	10.0	8.8	2.6	3.8	15.9	12.7
	10	16.3	16.9	5.6	9.2	34.1	21.7
Mnvr all	0.1	7.1	6.5	2.5	3.0	15.1	9.2
	10	40.0	38.2	13.6	35.0	83.7	42.9
REL cov	0.1	10.3	9.3	3.3	4.7	20.4	13.0
	10	10.6	9.6	3.3	4.7	20.6	13.5
CM1 cov	0.1	10.5	9.5	3.3	4.7	20.5	13.4
	10	10.5	9.5	3.3	4.7	20.5	13.4
OM1 cov	0.1	10.3	9.3	3.3	4.7	20.0	13.0
	10	10.6	9.6	3.4	4.7	20.7	13.5
OM2 cov	0.1	10.1	9.2	2.9	4.7	17.6	12.8
	10	19.8	16.0	12.2	4.8	75.1	24.9
OM3 cov	0.1	9.9	8.9	3.3	3.1	20.2	13.0
	10	36.2	35.9	6.6	34.9	40.2	37.1

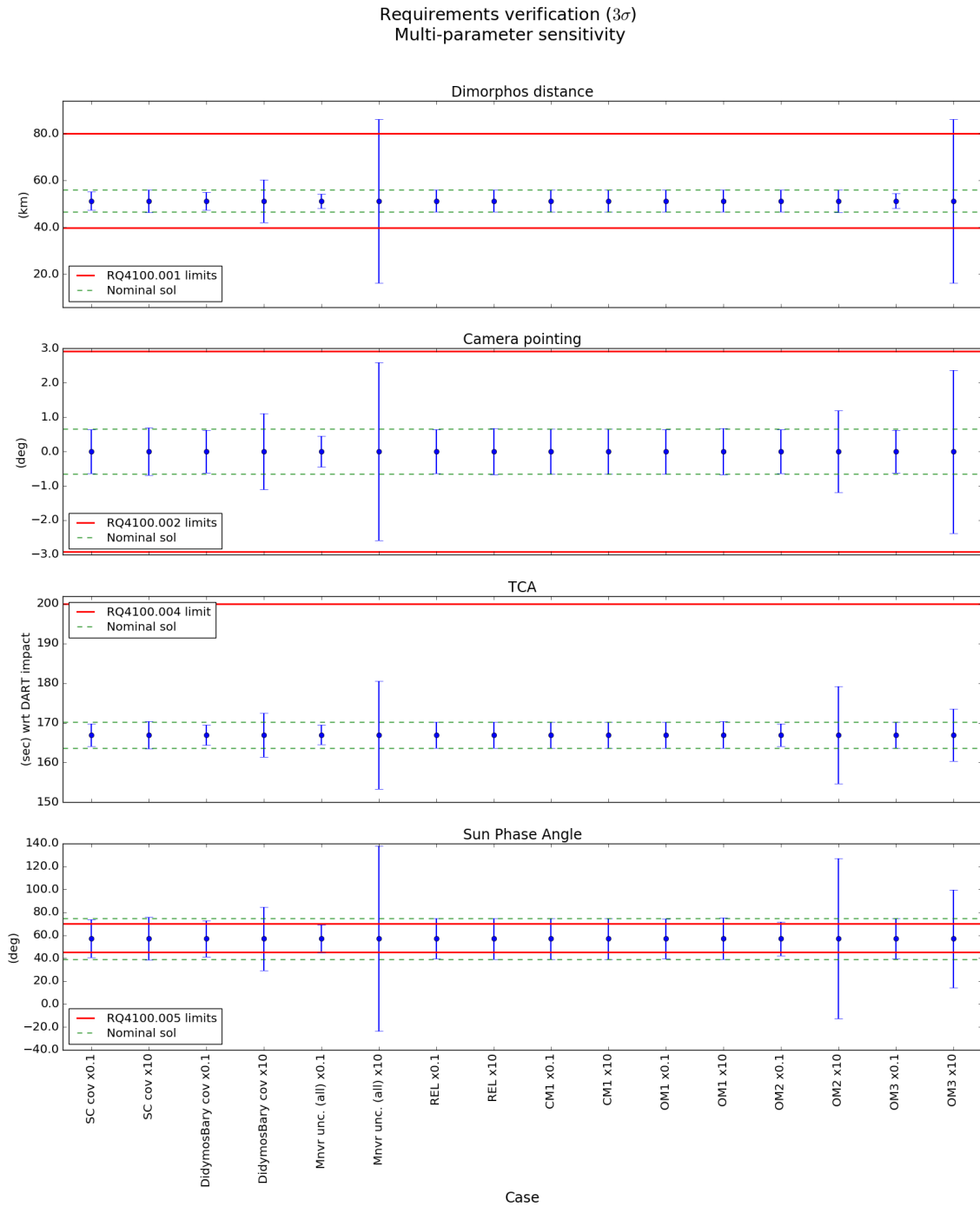


Figure 4.20: OD robustness results analysis requirements verification.

find out that two cases are not compliant also with the range requirement, namely the larger OM3 uncertainty and, as a consequence, the case considering the inflation of all the maneuvers' uncertainties. Moreover, this latter case can be studied as a superposition of the effect mainly due to OM2 and OM3. A larger OM2 uncertainty provides a major contribution to the LTOF and SPA uncertainties, whereas the Dimorphos radial distance and the camera pointing uncertainties are mainly related to the OM3. It is interesting to note that inflating the OM2 uncertainty, the time uncertainty increases a lot, but is still verified. On the other hand, the SPA uncertainty, which was already slightly out of the boundaries of about 5 degree, now overcomes the limits of about 50 degree. However, the requirement on the flyby time is still verified, because the tracking data collected after the maneuver execution allow to partially compensate this effect.

A last case of interest is the Didymos Barycenter uncertainty inflation, which shows a significant increase in all the investigated uncertainties, almost reaching the lower limit of the Dimorphos distance. However, a scale factor of 10 is very unlikely to be applied, being the input covariance yet from a conservative simulation provided by the DART NAV team.

#### 4.7.2 Observables

**Observables type** An analysis was performed to study the influence of the different types of observables. This study is critical to understand which kind of measurement contributes more to tearing down the uncertainty, thus which one can be sacrificed or added in case of contingency. The analysis explored various cases either using a single observable type or a combination of them. The measurements types are the ones presented in section 1.4.1, under the baseline noise assumptions. Note that the base case includes Doppler and ranging observables (DopR). Table 4.9 provides a numerical comparison of the B-plane uncertainties at the C/A, while figure 4.21 depicts those results. Noticeably, the contribution of the two types of radiometric observables is complementary since the Doppler manages to increase accuracy in normal direction (equivalent to the B-plane clock angle), while the ranging provides a significant contribution in the radial direction and in the LTOF. Thus, a combination of the two maximizes the achievable accuracy. Instead, the optical observables seem to provide a negligible contribution.

Table 4.9: OD results comparison with different observables types. Uncertainties are computed at delivery DCO, both in B-plane and Dimorphos RTN reference frames. Cases includes ranging (Rng, or R when associated to Doppler), Doppler (Dop) and optical (Opt) observables.

Case	$3\sigma$ uncertainty					
	B.T (km)	B.R (km)	LTOF (s)	R (km)	T (km)	N (km)
Rng	35.4	30.9	5.2	6.8	32.1	46.5
Dop	12.6	11.4	8.6	8.1	52.8	14.9
DopR (Base)	10.5	9.5	3.3	4.7	20.5	13.4
DopROpt	10.5	9.5	3.3	4.7	20.5	13.4

**Observables noise** Additional consideration about the assumed noise may be inferred for each observable. Figure 4.22 reports the effects of a variation of the Doppler noise. It

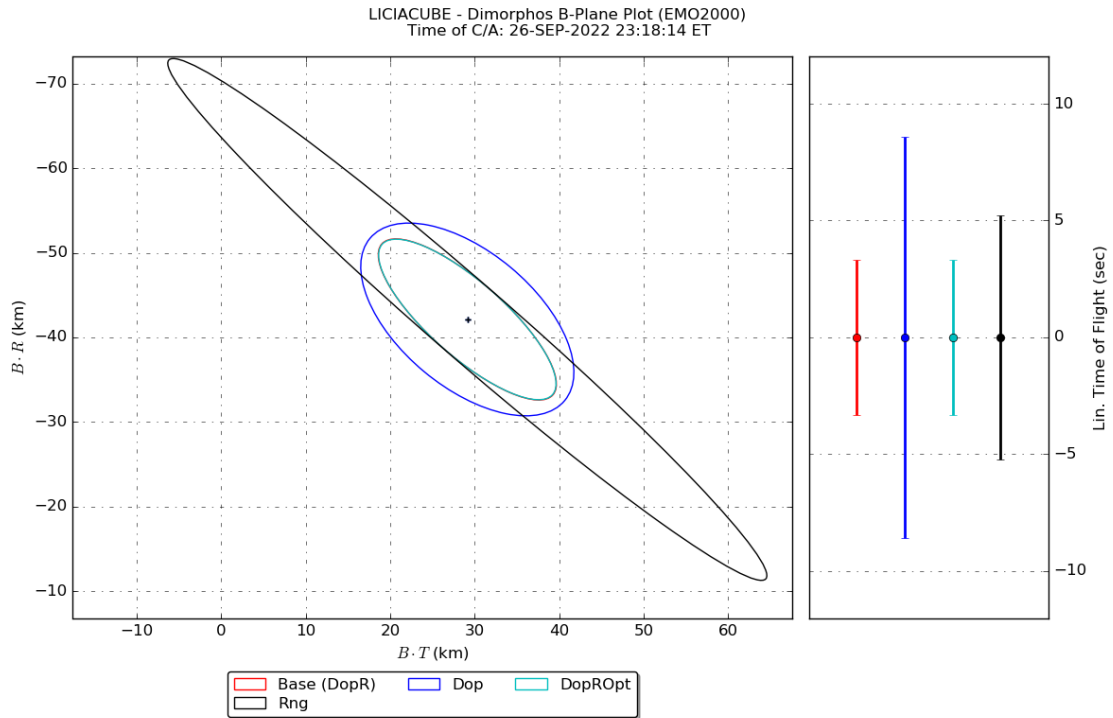


Figure 4.21: OD B-plane results comparison with different observables types.

is straightforward that the Doppler mainly affects the clock angle and the LTOF uncertainties. The radial direction is almost unchanged by a variation of this noise as the range observables probably constrain it.

On the other hand, the variation of the range bias shown in figure 4.23 let us provide some interesting conclusions. First, one may notice that the LTOF uncertainty is almost constant and thus does not depend on the range bias variation. As in the previous case, also the range bias mainly affects the B-plane uncertainty in the clock-angle direction, even though the contribution is much lower than the Doppler. Moreover, notice that inflating the uncertainty above the base value of 15 m does not provide any appreciable variation: it implies that the assumed base value for the range bias does not constrain the final results since some other parameter dominates.

Finally, the range noise analysis does not provide any significant variation of the results, and therefore it is not reported.

**Tracking passes loss** The robustness against the tracking data amount has been assessed by assuming the loss of one or more consequent passes. Thus, exploiting the baseline simulation, the data of the relevant tracking passes have been erased, and the reconstruction capability has been compared to the reference case. In particular, the comparisons take into account the uncertainties of the B-plane radial direction and time, the pointing accuracy at autonomous pointing algorithm locking, and the SPA angle. The requirement of the DSN to S/C pointing is not shown because always verified with large margins. The results are shown in figures 4.24 and 4.25 for the loss of one and two consecutive passes, respectively. Minimum variation is shown in most cases and against most of the requirements. The most significant variation can be observed for passes 12 to 14 on the SPA (clock angle) and Dimorphos camera pointing. The loss of these passes may cause an

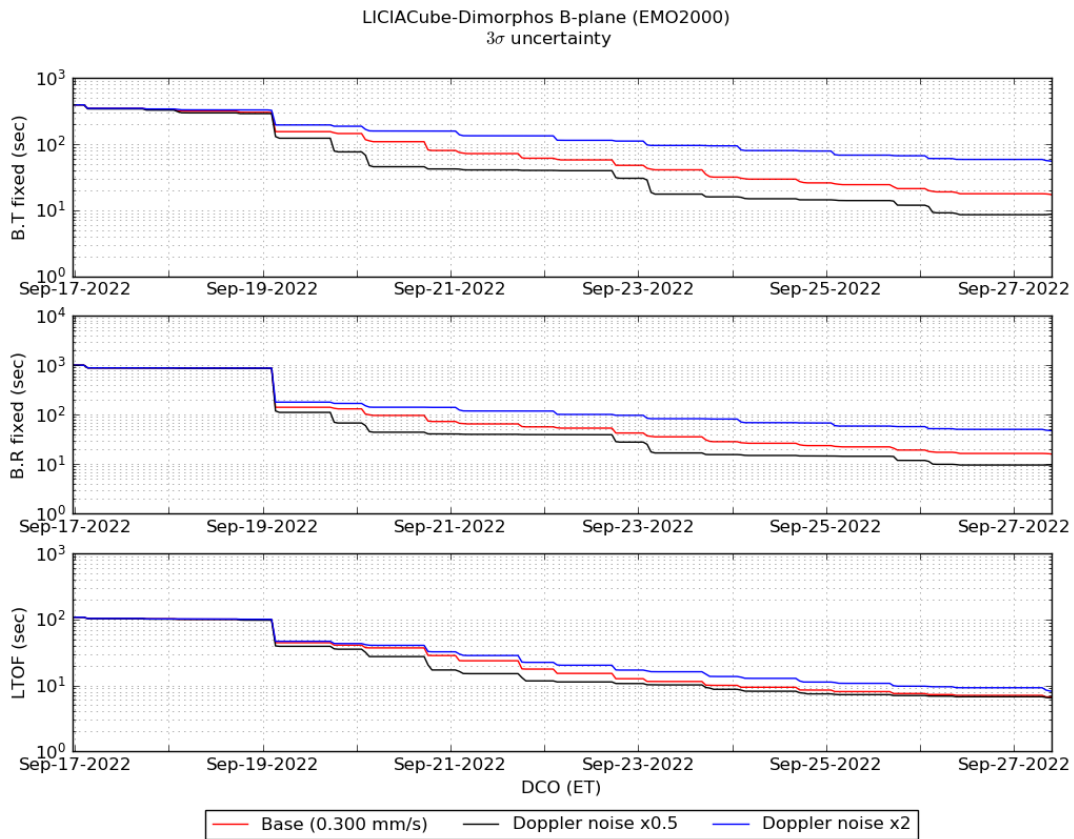
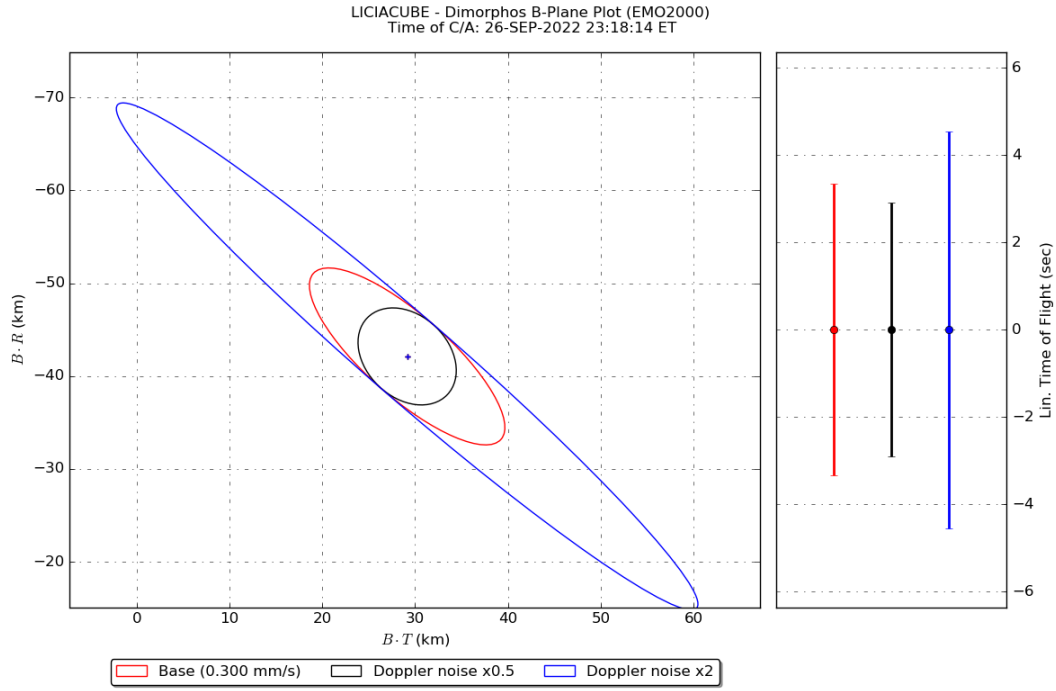
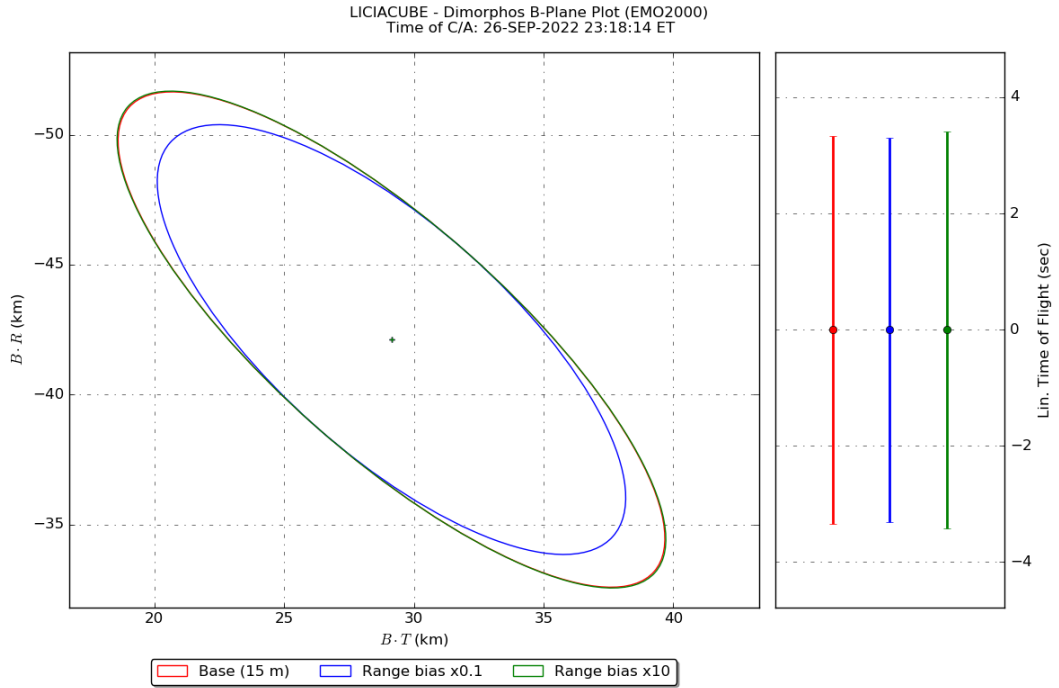
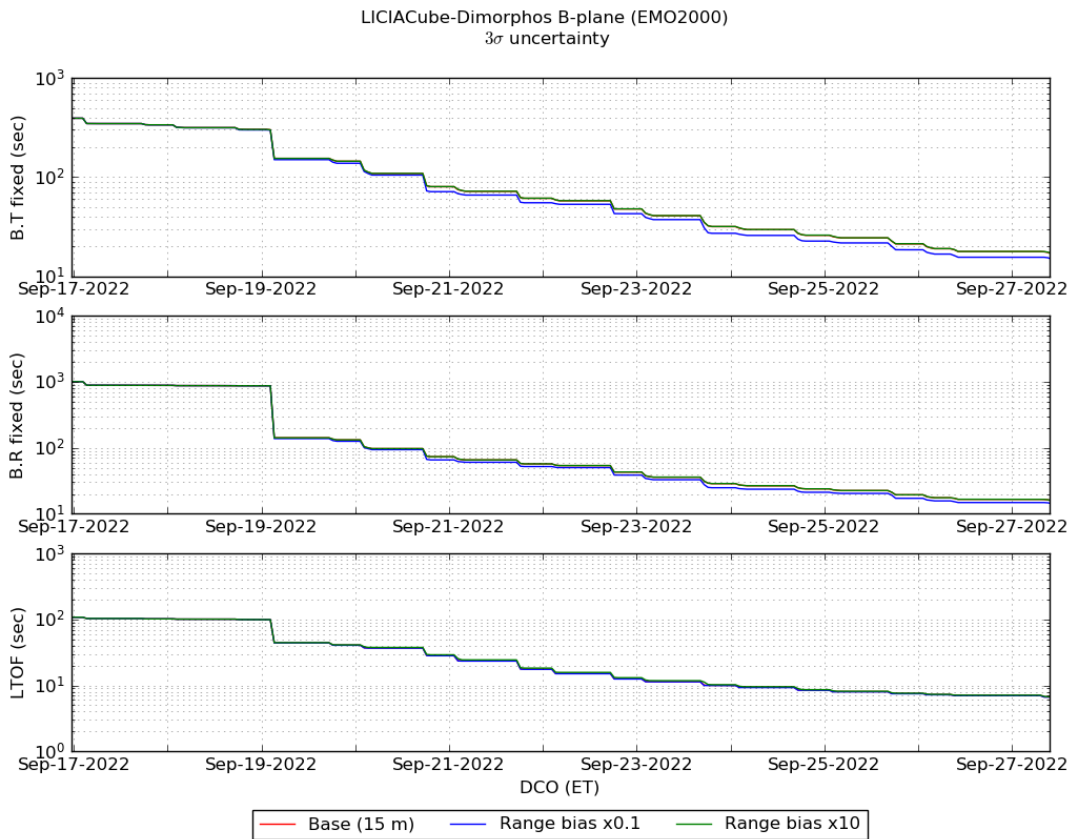


Figure 4.22: OD results assuming 0.1, 1 (0.300 mm/s) and 10 times the nominal Doppler noise.



(a) *S/C B-plane uncertainty at delivery DCO.*



(b) *B-plane parameters evolution.*

Figure 4.23: OD results assuming 0.1, 1 (15 m) and 10 times the nominal range bias.

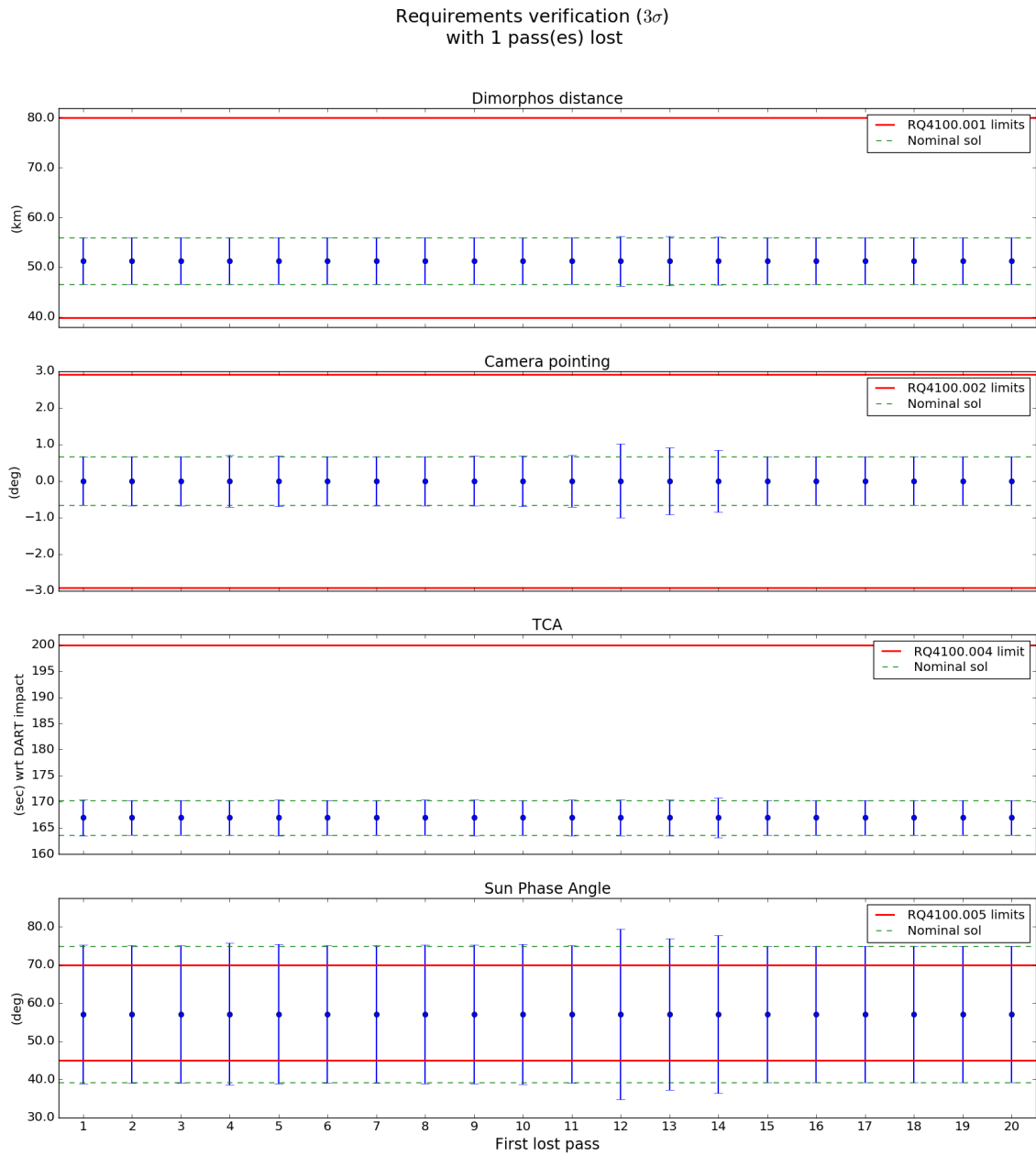


Figure 4.24: OD requirements verification with 1 lost pass.

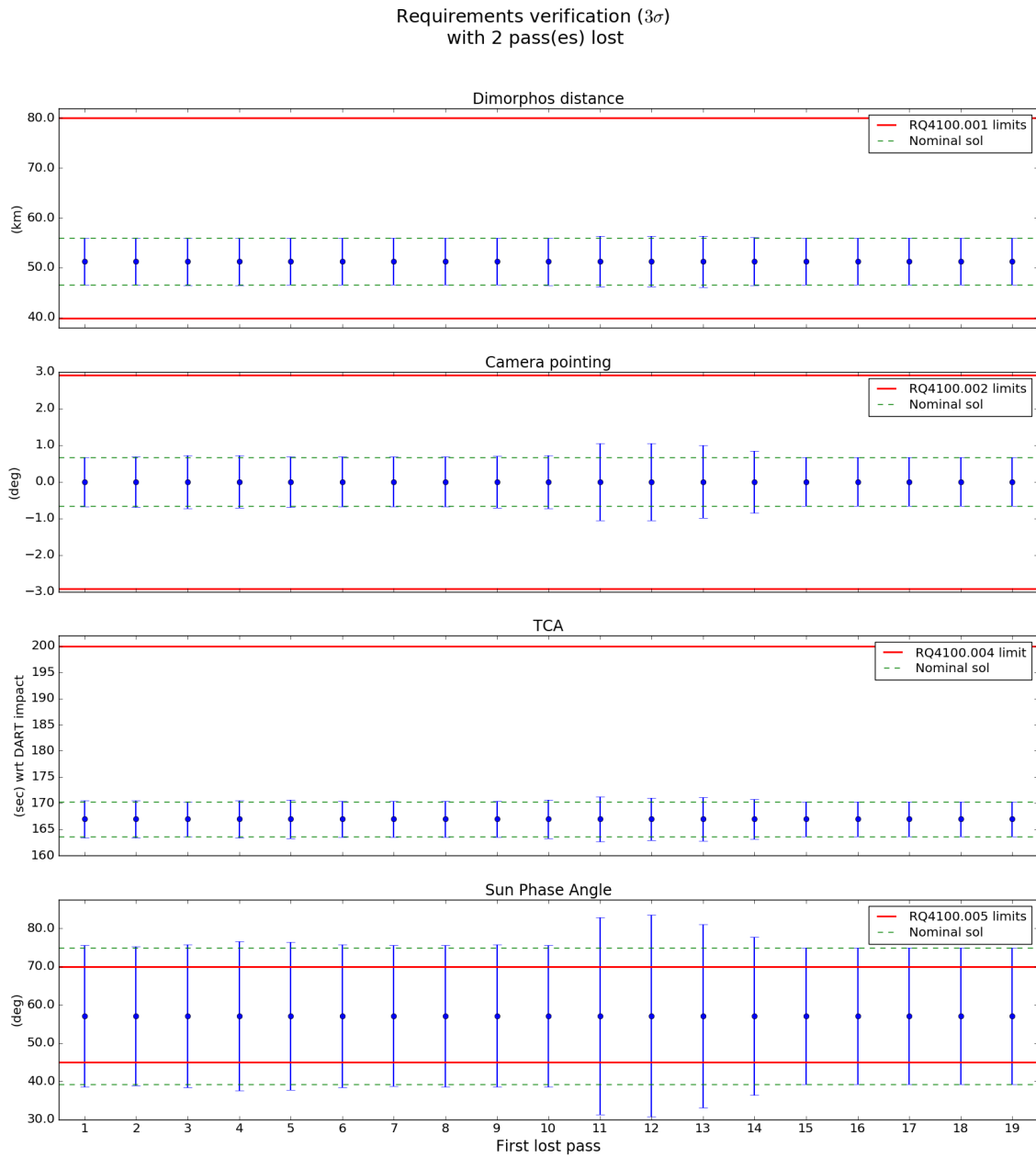


Figure 4.25: OD requirements verification with losing 2 consecutive passes.

appreciable deterioration of the SPA determination accuracy, while the weak effect on the camera pointing does not compromise its compliance. On the other hand, the loss of two consecutive tracking passes amplify this problem. In particular, any case including the loss of tracking pass 12 causes a larger exceeding of the SPA boundary and an increase in the pointing uncertainty, both fading for the following passes until the 14th. After this pass, the effect of a data loss will not affect the pre-flyby reconstruction. It is worth recalling from the mission timeline in figure 2.5 that pass 12 contains the OM2, and pass 14 is the last one before the delivery DCO. Hence, although the performance decay related to these passes loss is not large enough to compromise the whole mission, particular attention shall be paid to these passes during the operations.

### 4.7.3 Maneuver model

As already mentioned, the maneuvers are simulated and reconstructed as impulsive burns. Although this is expected to be a good approximation, as the maneuvers will be short, an analysis was performed to justify this assumption. Hence, the model of the largest maneuver OM1 has been modified to test different reconstruction methods' capability. To provide an accurate analysis during the generation of simulated observed observables, a more realistic model of the OM1 maneuver was implemented, which consists of:

- the main thrusters nominal  $\Delta V$  contribution as a finite burn of fixed duration, with a decreasing thrust profile and associated errors in the simulation;
- a set of 500 random impulse burn to account for RCS stabilization, conservatively assumed with a random spherical direction, and a  $\Delta V$  normal distribution of mean value  $\mu = 10\% \Delta V_{OM1,nom}$  and a standard deviation of  $\sigma = 50\% \mu$ .

The above-computed trajectory and the associated simulated tracking data are then processed using different maneuver models, namely:

- an impulsive burn with the same commanded  $\Delta V$  set at the finite burn start time and the baseline *a priori* uncertainties.
- an impulsive burn with the same commanded  $\Delta V$  set at the finite burn start time but a wider *a priori* time uncertainty equal to a 10% and 50% of the expected maneuver duration.
- an impulsive burn with the same commanded  $\Delta V$  set at the finite burn middle time and the baseline *a priori* uncertainties.
- an impulsive burn with the same commanded  $\Delta V$  set at the finite burn middle time but a wider *a priori* time uncertainty equal to a 10% and 50% of the expected maneuver duration.

The results are assessed in terms of maneuver reconstruction using an additional tracking pass after the maneuver. Results are reported in terms of maneuver time and  $\Delta V$ , both as visual depiction in figure 4.26 and in table 4.10. Several observations could be made on these results. First, regardless of the impulsive maneuver data, the  $\Delta V$  reconstruction converged to a reconstructed value about 1% lower than the finite burn with an estimated uncertainty about one order of magnitude lower than the *a priori*. Although compatible with its nominal value, the reconstructed one demonstrates that impulsive and finite burn may show a minimal bias. Instead, a more interesting behavior is visible in the estimation of the maneuver time. Being the finite burn spread over a time span (452 sec), one may

Case	Parameter	Nominal	Corrected	apSigma	Sigma	totDelta	/Sigma	/apSigma	unit
$\sigma_0 = 3$ s	DV	1.748e-03	1.737e-03	1.748100e-04	2.133e-05	-1.122e-05	0.526	0.064	km/sec
	TIME	0.000e+00	2.205e+02	3.000000e+00	5.064e-01	2.205e+02	435.378	73.498	sec
$T_0$	DV	1.748e-03	1.735e-03	1.748100e-04	2.133e-05	-1.278e-05	0.599	0.073	km/sec
	TIME	0.000e+00	2.269e+02	4.520000e+01	5.138e-01	2.269e+02	441.689	5.021	sec
$\sigma_0 = 0.1\Delta T_{burn}$	DV	1.748e-03	1.735e-03	1.748100e-04	2.133e-05	-1.279e-05	0.599	0.073	km/sec
	TIME	0.000e+00	2.270e+02	2.260000e+02	5.138e-01	2.270e+02	441.717	1.004	sec
$\sigma_0 = 3$ s	DV	1.748e-03	1.736e-03	1.748100e-04	2.134e-05	-1.191e-05	0.558	0.068	km/sec
	TIME	0.000e+00	2.191e+00	3.000000e+00	5.088e-01	2.191e+00	4.307	0.730	sec
$T_{mid}$	DV	1.748e-03	1.736e-03	1.748100e-04	2.134e-05	-1.192e-05	0.559	0.068	km/sec
	TIME	0.000e+00	2.256e+00	4.520000e+01	5.162e-01	2.256e+00	4.370	0.050	sec
$\sigma_0 = 0.1\Delta T_{burn}$	DV	1.748e-03	1.736e-03	1.748100e-04	2.134e-05	-1.192e-05	0.559	0.068	km/sec
	TIME	0.000e+00	2.256e+00	2.260000e+02	5.162e-01	2.256e+00	4.370	0.010	sec

Table 4.10: OD filter solution of a finite burn (OM1) using impulse burn models.

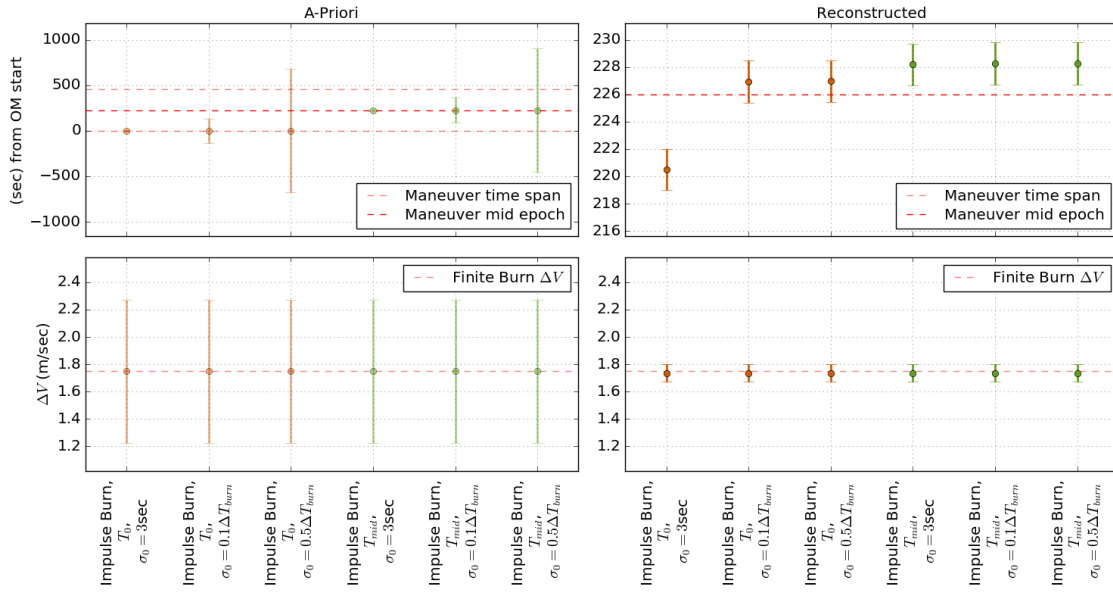


Figure 4.26: OD *a priori* and reconstructed epoch and  $\Delta V$  ( $3\sigma$ ) of a finite burn (OM1) using impulse burn models.

wonder what the correct point should be for an equivalent impulse burn. The results show that the *a priori* impulsive maneuver time should be set at the mid-time of the maneuver epoch, which provides for the time parameter lowest correction by the filter. Setting the impulse burn at the starting time of the finite burn will result in a too constrained parameter that will never reach the correct value unless a large *a priori* is used. Several tests have been performed, also setting a larger *a priori* value for the maneuver time up to  $1\sigma = 50\%\Delta T_{OM1}$  to obtain a reconstruction compatible with the mid-time case result.

# Chapter 5

## Flight Path Control simulations

### Contents

---

5.1	Introduction . . . . .	85
5.2	Statistical $\Delta v$ analysis . . . . .	85
5.3	Validation procedure . . . . .	87
5.4	Results . . . . .	88

---

### 5.1 Introduction

In this chapter, the FPC process is described in detail. At first, a linearized tool for the statistical  $\Delta V$  analysis is presented. In the following, FPC investigations procedure and results are shown to assess the feasibility of the guidance approach presented in section 1.4.2. For the complete approach phase, a complex and automated analysis was set up to perform a software-in-the-loop simulation. A comparison of the results is required to prove the applicability of the FPC method and the Linear Analysis of Maneuvers with Bounds and Inequality Constraints (LAMBIC) linear approach. The designed software performs a non-linear Monte Carlo analysis with model and state parameters perturbations. Its final goal is to correctly target the nominal aimpoint and eventually compute the statistical  $\Delta V$  to be compared with a coherent LAMBIC run.

### 5.2 Statistical $\Delta v$ analysis

The LAMBIC algorithm is used for the computation of the statistical  $\Delta V$  analysis [32, 15]. This is a useful tool to check the fuel required to meet the aimpoint target based on the model uncertainties. Instead of performing multiple non-linear propagations to assess the required propellant for each corrective maneuver, LAMBIC relies on a single OD run to produce the partial derivatives matrices required by LAMBIC. The calculation flow may be summarized as follows:

1. Given the *a priori* spacecraft state mapped at the encounter, and the partials derivatives, a certain number of samples states are generated from the initial covariance, mapped at the encounter. The deviation from the nominal encounter is computed as  $\Delta \mathbf{b}$ .

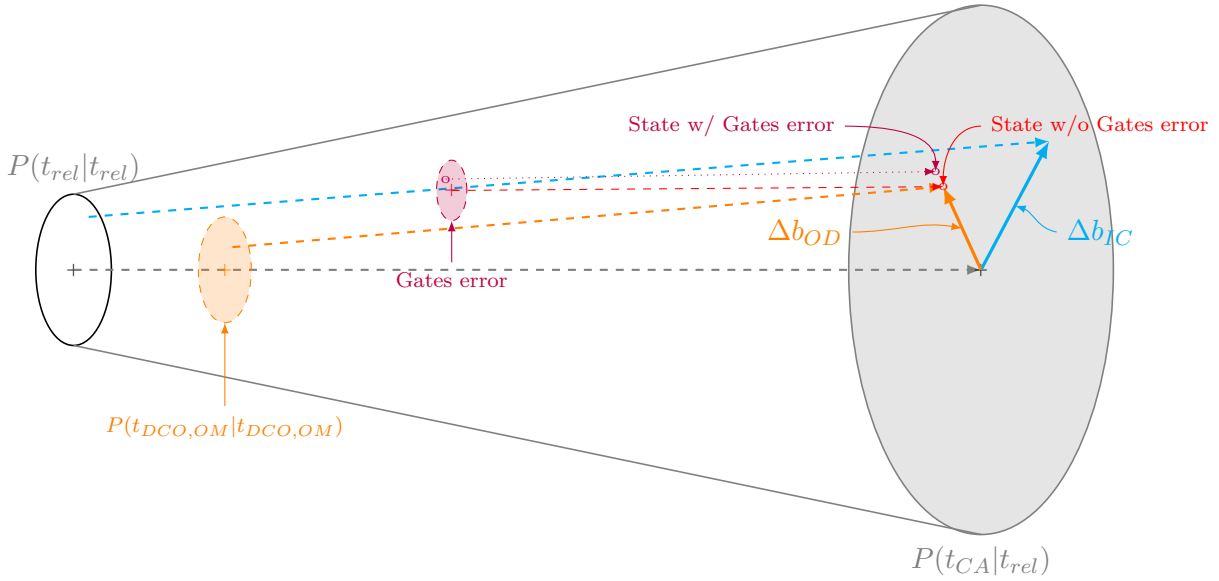


Figure 5.1: LAMBIC OD covariance propagation diagram.

2. An additional deviation is added to take into account the accuracy of the OD, computed by sampling the OD covariance matrix obtained from the DCO mapped to the encounter.
3. The correction maneuver is computed, under the linearization approximation, using the K-matrix introduced in equation 2.1.

For a more detailed description, we may refer to figure 5.1 where is depicted the working scheme for the first loop of the LAMBIC algorithm. Note that all the conditions are always mapped at the Dimorphos encounter B-plane, at the C/A epoch, namely demanding a match to the targeting  $B \cdot T$  and  $B \cdot R$  in-plane components plus the TCA. Starting from the sampled states generated from the initial covariance, the trajectory deviation at the target,  $\Delta \mathbf{b}$  are obtained. It is worth noting that, if only the initial covariance is assumed, the maneuvers can be directly computed as:

$$\mathbf{K}_1 \Delta \mathbf{v}_1 + \mathbf{K}_2 \Delta \mathbf{v}_2 + \dots = \Delta \mathbf{b}_{IC} \quad (5.1)$$

where the  $K_i$  is the partial derivatives matrix of the  $i$ -th maneuver  $\Delta \mathbf{v}_i$ . Therefore, it is possible to compute the corrective maneuver without further propagation from an evaluation of the mistargeting condition. Although, one should consider that the maneuver is computed from an estimated state which is affected by its correspondent OD uncertainty. This contribution, given in the picture by the orange dashed ellipse, may introduce a bias in the maneuver calculation, as we are targeting the aimpoint starting from an uncertain condition. Increasing the target deviation by a value from the sampled OD covariance at the encounter accounts for this contribution. Therefore, the deviation to clean up with the maneuver is:

$$\Delta \mathbf{b}_{design} = \Delta \mathbf{b}_{IC} + \Delta \mathbf{b}_{OD} \quad (5.2)$$

Thus, the  $i$ -th maneuver will be computed as

$$\Delta \mathbf{v}_{design} = K^{-1}(\Delta \mathbf{b}_{design} + \Delta \mathbf{b}_{OD}) \quad (5.3)$$

Nonetheless, the designed maneuver is not perfectly performed, so an error is added to the actual  $\Delta\mathbf{v}$  following the implemented maneuver execution error. The Gates model [63] is a particular model, usually employed for deep space mission and implemented in the LICIACube setup in section 4.4.

$$\Delta\mathbf{v}_{performed} = \Delta\mathbf{v}_{design} + \Delta\mathbf{v}_{error} \quad (5.4)$$

This method may include as many maneuvers as planned in the schedule by iterating the same flow, each time starting from a different condition provided by the OD covariance prediction from the previous cycle.

### 5.3 Validation procedure

At first, to assess the processing time and the capability of targeting the nominal state at the B-plane, the trajectory was manually perturbed by inserting an *a priori* error on the DART state at release, Didymos state, or a model parameter. Those conditions were quickly solved by the FPC algorithm in a few iterations. Therefore, a more complex software-in-the-loop simulation was set up. This study accounts for all the maneuvers to compute the produced dispersion, although release and CAL1 are assumed to be commanded with their deterministic, *a priori*  $\Delta V$ , eventually contaminated by the respective execution error. All other maneuvers are assumed to be closed-loop, and thus a correction to their nominal values exists to account for the retargeting. The computation is done by a fully automated software that performs the following steps:

1. retrieve the relevant information from an OD run, namely by loading a *ginlock* file;
2. perturb the initial conditions for the Didymos system, Dimorphos, the S/C, the SRP scale factor, and purely deterministic maneuvers accordingly to their respective *a priori* covariance;
3. propagate the trajectory, without the closed-loop maneuvers;
4. compute the deviation from the nominal target  $\Delta b_{design}$ ;
5. add the *i-th* search-for maneuver;
  - i perturb the nominal target aimpoint by a vector  $\Delta b_{OD}$  computed from the *i-th* maneuver DCO OD covariance;
  - ii run the FPC to find  $\Delta\mathbf{v}_{design} = K^{-1}(\Delta\mathbf{b}_{design} + \Delta\mathbf{b}_{OD})$ ;
  - iii perturb the found *i-th* maneuver and add to the propagation as  $\Delta\mathbf{v}_{performed} = \Delta\mathbf{v}_{design} + \Delta\mathbf{v}_{error}$ ;
  - iv re-propagate the trajectory;
6. repeat point 5 for all the closed-loop maneuvers;

The simulation computes the entire loop of the maneuvers calculation by iterating a given number of times (in our case, 10000) to get the statistics, namely the final dispersion in the C/A and the  $\Delta V$ .

The NAV simulations results are presented in the next section and eventually compared to the same setup results of LAMBIC. The targeting conditions of the aimpoint have been set on the B-plane in-plane components  $B \cdot R$  and  $B \cdot T$ , and the TCA, whose values are shown in table 5.1. The OD covariances are computed from a preliminary OD analysis

Table 5.1: Target point on the Dimorphos B-plane (EMO2000).

$B \cdot R$ (km)	$B \cdot T$ (km)	TCA
-42.1	29.0	26-SEP-2022 23:18:14.2503 ET

and fed to FPC and LAMBIC. These are used for the search-for maneuvers calculation, therefore are computed for each search-for maneuver at its respective DCO and mapped to the encounter conditions. Since the Gates model for the maneuvers execution error is already applied both in the FPC simulation and LAMBIC, the preliminary OD solution has been obtained without the maneuvers uncertainties.

The simulated samples (10000 trajectories) are finally processed to obtain the statistical distribution for different cases. At first, only initial conditions were perturbed, considering:

- DART full covariance matrix at release;
- Didymos Barycenter full covariance matrix;
- Dimorphos diagonal covariance matrix;
- SRP scale factor sigma.

Then, two additional cases have been implemented, adding the OD error for the maneuver calculation or the maneuver execution errors except for the release, which is always associated with deployment error. Finally, all the contributions were accounted for in the complete simulation.

## 5.4 Results

The obtained comparison results are summarized in tables 5.2 and 5.3 for non-linear Monte Carlo and LAMBIC, respectively. The comparison among the analyzed cases shows negligible differences which become more consistent in the case without the maneuver execution error (injection covariance + OD Error). Nonetheless, the maneuvers uncertainty provides the largest contribution to the overall  $\Delta V$  and the full case shows a difference of the total consumption less than 0.2%. Furthermore, it is worth noting that the non-linear algorithm took more than two hours to process 10000 samples whereas few seconds are required for the LAMBIC to retrieve comparable results.

Based on the comparison, it can be concluded that the LAMBIC can be reliably applied to the LICIAcube mission, and henceforth, the results will be obtained with the linearized algorithm.

Thus, the LAMBIC tool has been used in the pre-operations phase to verify the maneuvers fuel consumption required to achieve the B-plane target in table 5.1 in the selected scenarios. The hereafter presented case is the baseline one, namely the nominal release at 10 days before DART planned impact. The obtained values are reported for each maneuver in table 5.4 and the associated cumulative  $\Delta V$  during the approach phase is depicted in picture 5.2. A result of particular interest is that the 99 %-tile of the OM2A is comparable to the deterministic component of the OM1A.

These values consider both the closed-loop commanded value and the error committed during the execution so that it is possible to evaluate the remaining propellant mass. Note that the release does not contribute to the cumulative  $\Delta V$ , as it uses a spring compression energy to deploy. Moreover, although the deterministic value of OM1 provides the main contribution, its  $\Delta V$  is quite limited. Conversely, the corrective maneuvers

MNVN	Injection Covariance			Injection Covariance + Execution Error			Injection Covariance + OD Error + Execution Error		
	$\mu$	$1\sigma$	$\Delta V_{99\%}$	$\mu$	$1\sigma$	$\Delta V_{99\%}$	$\mu$	$1\sigma$	$\Delta V_{99\%}$
RELE	1.18	0.07	1.34	1.18	0.07	1.34	1.18	0.07	1.34
CAL1	2.00e-3	0.00	2.00e-3	2.00e-3	2.00e-4	2.47e-3	2.00e-3	0.00	2.00e-3
OM1	1.75	0.07	1.91	1.75	0.19	2.20	1.75	0.07	1.92
OM2	0.00	0.00	0.00	0.54	0.35	1.61	0.03	0.02	0.08
OM3	0.00	0.00	0.00	0.12	0.12	0.59	0.07	0.03	0.17
Total	1.75	0.07	1.91	2.41	0.66	4.40	1.85	0.12	2.17

Table 5.2:  $\Delta V$  statistics from Monte Carlo analysis. Results are in m/s. REL is not accounted in total row.

MNVN	Injection Covariance			Injection Covariance + Execution Error			Injection Covariance + OD Error + Execution Error		
	$\mu$	$1\sigma$	$\Delta V_{99\%}$	$\mu$	$1\sigma$	$\Delta V_{99\%}$	$\mu$	$1\sigma$	$\Delta V_{99\%}$
RELE	1.18	0.07	1.34	1.18	0.07	1.34	1.18	0.07	1.34
CAL1	2.00e-3	0.00	2.00e-3	2.00e-3	2.00e-4	2.46e-3	2.00e-3	0.00	2.00e-3
OM1	1.75	0.07	1.91	1.75	0.19	2.20	1.75	0.07	1.91
OM2	0.00	0.00	0.00	0.53	0.36	1.67	0.08	0.04	0.20
OM3	0.00	0.00	0.00	0.12	0.12	0.58	0.10	0.06	0.27
Total	1.75	0.07	1.91	2.40	0.67	4.45	1.94	0.17	2.38

Table 5.3:  $\Delta V$  statistics from LAMBIC analysis. Results are in m/s. REL is not accounted in total row.

Table 5.4: Statistical  $\Delta V$  from LAMBIC analysis.

MNVR	$\mu$ (m/sec)	$1\sigma$ (m/sec)	$\Delta V_{90\%}$ (m/sec)	$\Delta V_{95\%}$ (m/sec)	$\Delta V_{99\%}$ (m/sec)	Notes
RELE	1.18	0.07	1.27	1.29	1.34	No fuel consumption
CAL1	2.00e-3	2.00e-4	2.26e-3	2.33e-3	2.46e-3	Open-loop
OM1A	1.73	0.31	2.14	2.25	2.50	Closed-loop
OM2A	0.41	0.26	0.77	0.92	1.21	Closed-loop
OM3A	0.25	0.15	0.44	0.52	0.73	Closed-loop
Total	2.40	-	3.35	3.69	4.45	Not account for RELE

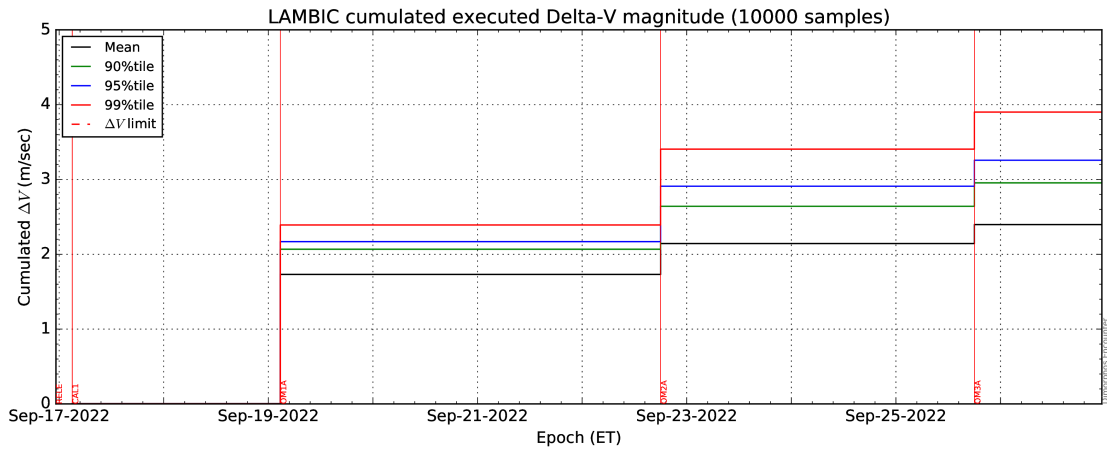


Figure 5.2: LAMBIC result for baseline trajectory.

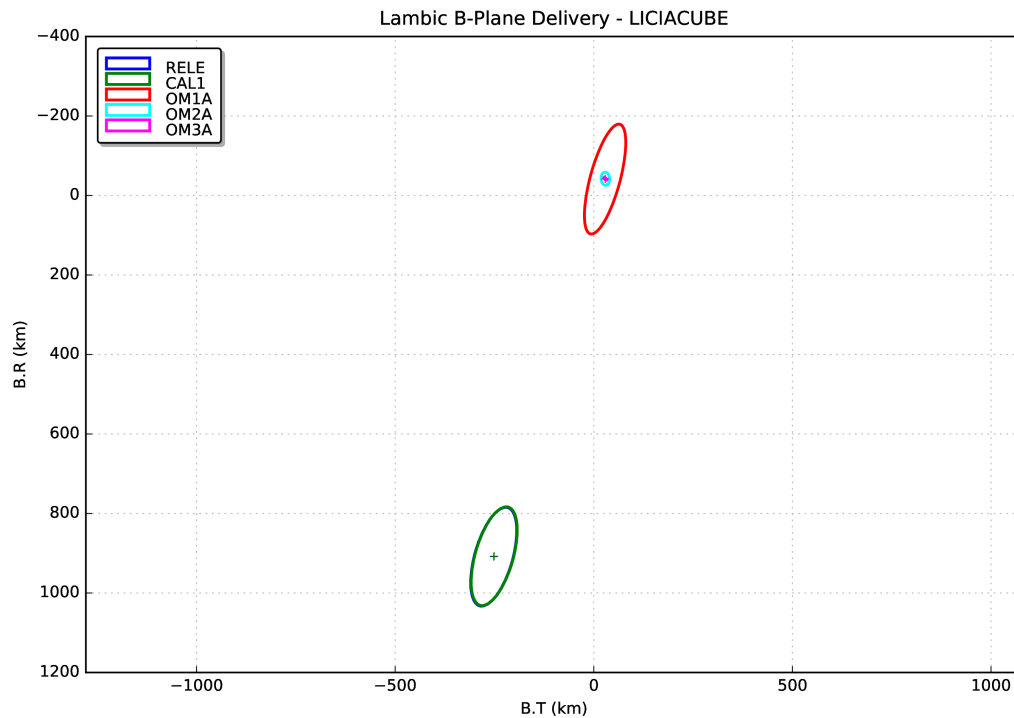


Figure 5.3: LAMBIC B-plane dispersion at each maneuver, for baseline trajectory.

OM2A and OM3A present a much larger  $\sigma$  compared to their mean values. Furthermore, the mean value of the corrective maneuvers decreases moving from OM2A to OM3A since the targeting is reached asymptotically. In the ideal case of an infinite series of corrective maneuvers, one would expect their mean value to decrease considering following maneuvers, reaching a steady value where the thrust is required only to clean up the previous maneuver execution error.

In addition to the  $\Delta V$  considerations, it is important to check the evolution of the trajectory B-plane parameters. Figure 5.3 represents the prediction of the B-plane coordinates of each case obtained by adding the following maneuvers to the initial condition. The uncontrolled trajectory would pass about 950 km far from Dimorphos. It is evident that the release and the CAL1 do not significantly contribute to targeting the aimpoint and, being purely deterministic, cannot reduce the predicted error. Conversely, the OM1A is the main targeting maneuver, which shifts the B-plane nominal coordinates to the desired one, with small inflation of the spacecraft covariance, due to OM1A execution error. Finally, the corrective maneuvers dramatically tear down the covariance while keeping the aimpoint.



# Chapter 6

## Operations preparation

### Contents

---

<b>6.1</b>	<b>Introduction</b>	<b>93</b>
<b>6.2</b>	<b>Interfaces</b>	<b>93</b>
<b>6.3</b>	<b>Navigation operations</b>	<b>94</b>
6.3.1	Staff	95
6.3.2	Processes	95
6.3.3	Maneuvers	97
<b>6.4</b>	<b>Tools</b>	<b>99</b>
<b>6.5</b>	<b>Testing</b>	<b>100</b>

---

### 6.1 Introduction

This chapter will describe the main steps, procedures, and interfaces used during the operations to provide a general overview of the ongoing preparation activities. The operations definition is still under development, with the contribution of all the teams involved. In fact, for this task, the collaboration of multiple operators is required to achieve the mission goals. This preliminary phase of operations mainly establishes all the required interfaces as well as internal and inter-teams procedures to follow not to miss any step during the operations. The identified procedures may also be used preliminarily to train the involved human resources and investigate possible critical steps in data exchange and computation that may jeopardize the mission goals.

### 6.2 Interfaces

Complete identification of the teams and access points shall be made at the beginning to establish hierarchies and data fluxes requirements. Therefore, the following teams were identified:

**ASI** team will supervise the inter-team iterations and make the final decisions whenever required.

**ARG** namely the Argotec team, will be responsible for the operations of the LICIACube, providing for telecommands generation and telemetry and data downlink.

**MA** team of the POLIMI will provide for baseline strategy modification, if required, and for the maneuver design.

**NAV** node is responsible for the trajectory reconstruction and propagation, and the computation of corrective maneuvers. Due to the critical role for the mission goals achievement, it is composed of two separated and independent teams which will work in parallel starting from the same set of data:

**UBO** from the University of Bologna, under ASI contract;

**JPL** from the Jet Propulsion Laboratory, granted to the LICIACube working group by APL agreement.

**DSN** represents the operators of the ground stations used to communicate and track the spacecraft.

**APL DART SCI** is the DART science team which handles its scientific data.

**JPL DART NAV** is the navigation team of DART which collects the probe navigation data and produces the correspondent trajectory and maneuvers reconstruction.

The interfaces among the teams for the LICIACube mission activities are depicted in figure 6.1. Two main blocks well separate the Italian and the American teams, connected through a redundant internet connection. The Italian side is under the supervision of the ASI. The operations are performed at the Mission Control Center (MCC) where the different teams will work concurrently either in direct or indirect contact with each other. The main node is represented by the front room, through which all the connections flow. The backroom is dedicated to the Argotec specialists in charge of the subsystems. In the MCC, there is also the Italian NAV team of UNIBO which will be physically in the main control room during the operations (at least for the most critical part of the mission, i.e., the approach phase). The MCC is also connected to the Space Science Data Center (SSDC) for the storage of the relevant scientific data. On the other hand, the US side is composed of two parts: the JPL side, which handles the G/Ss and the NAV teams (one for DART, one for independent LICIACube navigation) and the APL side, which operates the DART probe, collecting both mission and scientific data. Particular attention should be paid to the NAVs, which shall be fully separated and independent. For this reason, the point of contact with other teams shall be unique and equal to the teams to guarantee they both have the same input data to provide consistent results. This point of access is represented by the MCC which consists of a repository of the relevant data products on a SSH File Transfer Protocol (SFTP) server managed by Argotec. Other than the NAV teams, this server collects and distributes the data to the operations front room, where the S/C is handled, the MA team, and the Science teams through the Science Operations Center (SOC), the DART's Mission Operations Center (MOC) and the DSN. All the operators also have a direct mail and telephonic link to the LICIACube MOC and its online tool to notify any anomaly or important remark to share with other teams.

A NAV Interface Control Document (ICD) [29] has been developed to design and control the navigation data flow, with specifications of each input and output data required (called *data products*), along with their originator, availability and format.

### 6.3 Navigation operations

The NAV segment of the LICIACube mission comprehends the people, the hardware, and software required to provide a consistent and accurate reconstruction of the spacecraft

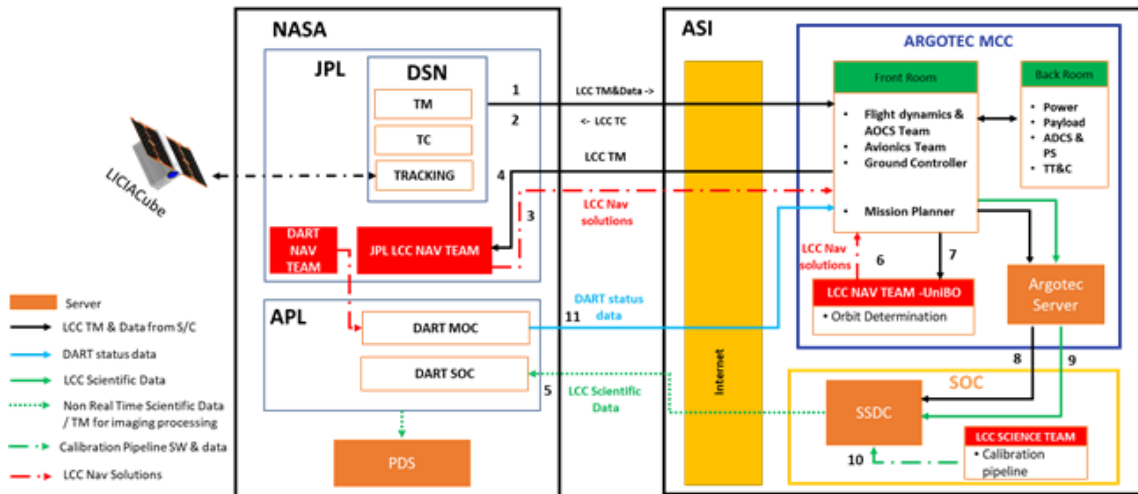


Figure 6.1: LICIACube operation interfaces.

orbit and fly it as close as possible to the reference conditions. This section analyzes the main resources in relation to the adopted procedures.

### 6.3.1 Staff

During the first 10 days, the LICIACube mission has its critical phase, subject to tight time requirements. Thanks to international agreements, two independent teams will perform the navigation, namely one team of the UNIBO and one from the JPL. Considering the LICIACube requirements and resources, the UNIBO NAV team has been structured as follows [3]:

- n.2 junior analyst, with substantial previous training on the specific setup of LICIACube, also obtained by a dedicated test phase. These are responsible for the reconstruction runs and the maneuver calculation, working independently.
- n.1 senior analyst with considerable experience in OD. This figure will act as a coordinator of the teams' work, eventually collecting the results of the runs for a first quick look of the achieved results. He will also be responsible for reporting issues experienced by other teams during the period of interest.
- n.1 senior analyst with considerable experience in OD, and a deep knowledge of the LICIACube setup. This person will be the supervisor of the NAV team, responsible for the solution approval and release.

This complete team is planned to follow the first 15 days of the mission at Argotec facilities (Turin) to have a stronger and more direct iteration with the other teams if required. Additional preparation time is planned 5 to 7 days before the release to set up the local hardware and run the last pre-flight analyses. The rest of the mission will be supported by a reduced team from the Radioscience and Planetary Exploration Laboratory of the UNIBO in Forlì.

### 6.3.2 Processes

The final work demanded of the NAV team is to deliver the reconstructed trajectory on the base of the acquired data and to provide maneuvers to correctly fly the probe, realigning

the actual trajectory with the reference one, if necessary. These tasks are achieved by a series of subsequent steps, which provide for the trajectory reconstruction, evaluation of the deviation from the reference, and, if the aimpoint condition requires it, the computation of corrective maneuvers. Moreover, preparation and closure actions are required to complete the data exchanges with other teams. Therefore, the typical process flow followed between a DCO and its related data products delivery are listed in the following activities:

1. Activity preparation: this includes all the setup of the incoming analysis. It foresees the complete update of the fields for the current arc to be analyzed: for example, the arc dates and the list of the maneuvers planned for the arc should be set.
2. Data download: this step provides the download of all the data products necessary for the arc reconstruction. All the latest operations data shall be downloaded from the MCC SFTP, mounted into a local folder, based on the ICD [29] guidelines.
3. Data pre-processing: the input data manipulation for format conversion, parsing, cleaning of spurious points, followed by a quick assessment of the data quality. The data pre-processing is a semi-autonomous script that provides for data parsing from input files, required format conversion, and file merging. The observables manipulation consists of two parts: a first quick look to get information about data quality, with possible spurious data erase, and a time compression from 1s to 60s integration time. Therefore data are ready to be processed by the OD, but an inspection is foreseen before starting to confirm the correctness of the pre-processing outputs.
4. Orbit Determination: once the setup files and input data have been prepared and checked, the reconstruction may begin. The OD process is performed by a script which may require more iteration to converge. The convergence is achieved when the solve-for parameters (and thus the residuals) do not significantly change compared to the previous step. As the stop condition is not implemented in the algorithm, each analyst launches the runs until he considers the solution has converged.
5. OD solution consistency check: the OD results should be evaluated in terms of data residuals and parameters estimation. The operator then evaluates the obtained results, thanks to an internal reporting tool, which provides a deep in-look into the quantities of interest, mainly the filter parameters variation, the B-plane conditions, and the relative miss-targeting. The pointing uncertainties are also reported to check the NAV requirements compliance.
6. Computation of the corrective maneuver: whenever the aimpoint and/or the related dispersion are not achieved with the prediction of the reconstructed trajectory, a corrective maneuver is computed to realign the actual trajectory to the reference one by targeting the B-plane aimpoint.
7. Internal solution consistency check and approval: the results of the previous points should be evaluated in terms of trajectory reconstruction and achievement of the desired target, along with its correspondent dispersion. The analyst generates a report and packs the run folder into a self-consistent executable folder, with the report files and logbook files containing notes of hot points and problems faced. These data are sent to the supervisor, who will receive two sets of independent analyses and, comparing them may either decide to accept one of them or require further analyses.

8. Data upload: once the supervisor grants his acceptance, the selected solution-related files are uploaded to the MCC server, and a notification is sent to the other teams.
9. Verification of the finite burn: the potential corrective burn computed as impulsive is externally converted into a finite burn by the MA. The obtained maneuver shall be eventually verified into the OD model by replacing the impulse burn with the finite one. Finally, the supervisor provides for the approval of the finite burn implementation, and reports are automatically generated eventually comparing the UNIBO solution to the JPL one.
10. Team meeting: at the end of the work, a meeting is called to decide on the necessity of maneuver implementation. Maneuvers are compared between UNIBO and JPL, and the presentation previously prepared is shown to the team to support the delivered solutions. Finally, a decision is taken on the reconstructed trajectory to use for the operation (as it affects pointing, timeline, etc...) and which maneuver to implement, and the relevant files are labeled as *approved*.

A detailed representation of the above described flow, is depicted in figure 6.2.

### 6.3.3 Maneuvers

The realization of trajectory correction maneuvers involves several steps performed by different teams. This section provides a detailed description of the correction maneuvers process. Based on the schedule draft in figures 2.5 and 2.6, two to four maneuvers are planned, depending on the release time. Among them, three are closed-loop, i.e., they are performed based on a command updated during the operations and computed with the observables acquired. Therefore the high-level procedure for the maneuver computation has been developed to be performed after the OD trajectory reconstruction (figure 6.3).

The OD team compares the B-plane target with the propagated B-plane crossing, including the uncertainties. If the propagated B-plane uncertainty ellipse is out of the set boundaries or any other requirement is not verified, the following maneuver is computed to correct the actual trajectory by targeting the B-plane aimpoint, established before the operations and available in the dedicated data product. This calculation is performed through the Flight Path Control (FPC) routine, whose algorithm has been described in section 1.4.2. It requires as input a set of coordinates and their nominal values and a convergence condition for any of them. The outputs will be the computed maneuver to be performed as a MONTE command to be implemented for the related trajectory propagation. At the end of this process, the OD team validates the computed impulse burn maneuver and sends it to the MA. Thus, the impulsive burn is externally translated into a finite burn, defined by a thrust model and a duration, which is eventually sent back to the OD team. The analyst converts the finite burn to MONTE implementation, then provides it to the OD software. Finally, the propagated finite burn trajectory is obtained and checked against the impulsive burn one, the B-plane conditions, the compliance with the requirements, and the estimated fuel consumption. If the check is passed, the maneuver is accepted and formally delivered to the LICIACube team by server upload and notification. When both NAV teams deliver their solutions, a comparison report is prepared by autonomous script, and a *NAV Solution Acceptance Meeting* is called. During the meeting, the proposed solutions are presented with their — possible — different approaches and results. In the end, one solution is chosen by ASI, and the related data product are labeled as the chosen ones. Thus, Argotec may retrieve the data required to prepare the telecommands for the spacecraft activity.

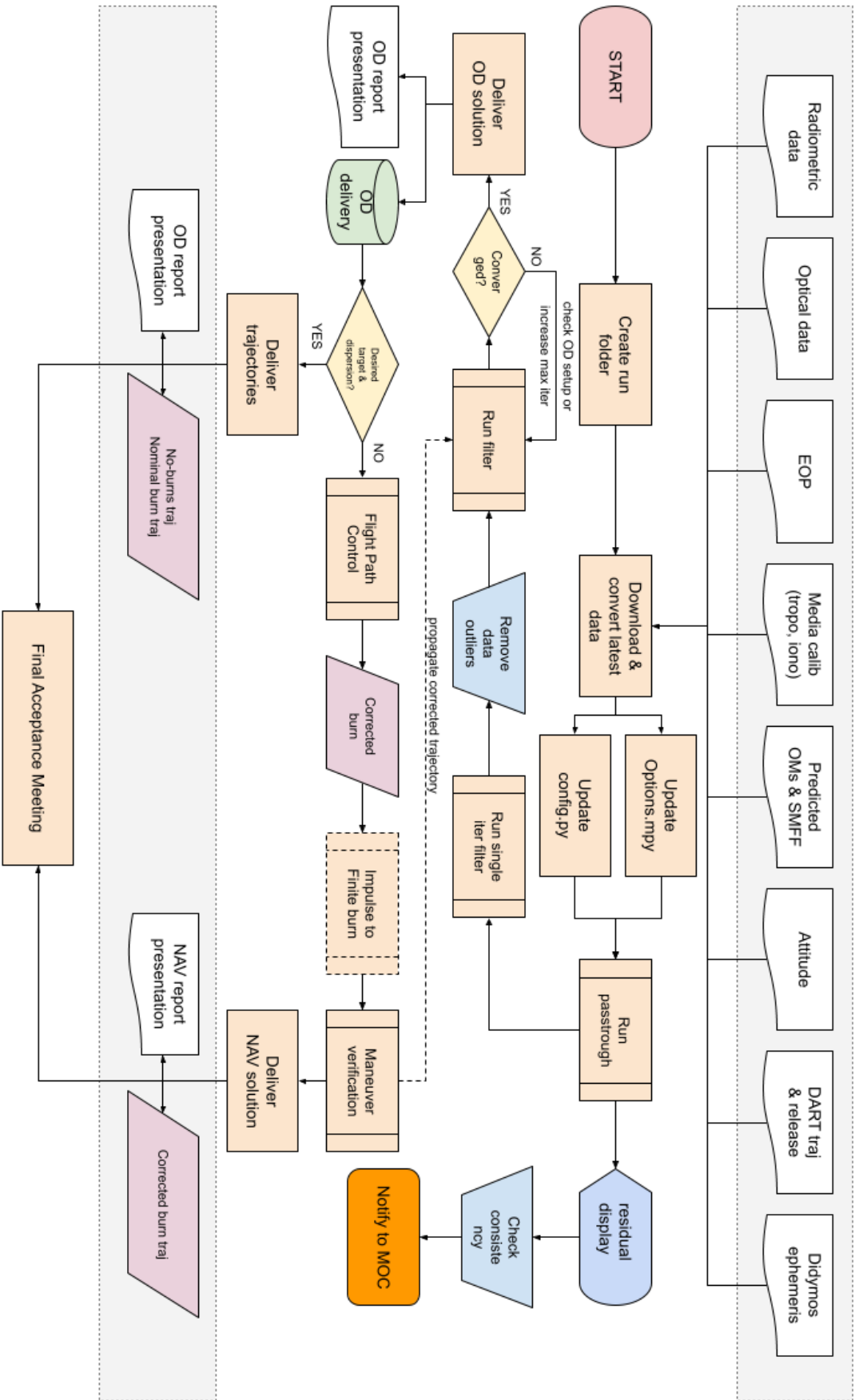


Figure 6.2: Navigation operation process schematic [3].

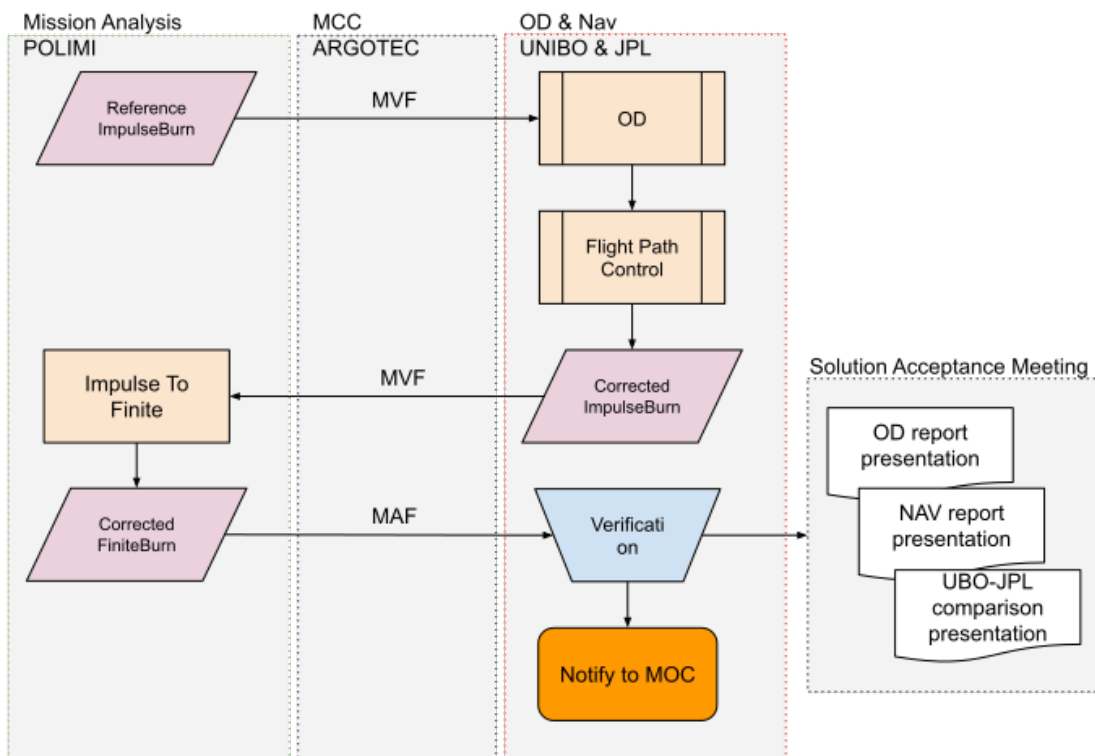


Figure 6.3: Maneuver design and verification sub-process schematic.

## 6.4 Tools

The standardization of the mission processes is of primary importance in order to have a complete toolkit for the OD and NAV. Although many steps cannot be fully automated since they are strongly mission dependent and require human interaction, most of the work has been implemented into a series of Python and bash scripts to be efficiently configured and run. The existing scripts for the OD have been encapsulated in a more extensive setup. It is based on strict files organization for the internal runs files and a smoother organization for the Input and Output (I/O) files. The resulting structure of the run folder can be summarized as follows:

**Options.mpy** General run initialization file, containing the files to include in the model, the filter configuration, and the software setup.

**config.py** General run configuration file, containing a list of the input files to include, where the initial conditions are retrieved.

**inputs** Folder containing all the files which define the model.

**att** Folder containing the support attitude files.

**data** Folder containing the data information, both for noise level and inputs data edit commands.

**eph** Folder containing the support ephemeris files.

**media** Folder containing the support media corrections files.

**trk** Folder containing the support observables files.

**outputs** Folder containing the run results.

The main tools developed are listed below:

**Input file parsing** uses the library parsers to cast all the required files into the correspondent MONTE model files, asking for confirmation of the operator for any step. A semi-autonomous approach is preferable due to possible miss-formatting or file corruption which may endanger the setup.

**OD and NAV reporting** exploits many sub-routines specifically developed to extract data from the run generated files (ginlock, mappings, residuals) and report the relevant information. It automatically encapsulates the plots, tables, and notes in a latex presentation, compiling them into a pdf file. The presentation's content is strongly mission-dependent and shall be customized before the operations. Nonetheless, a large variety of outputs can be extracted thanks to the developed dedicated library.

**Flight Path Control** is a script that, recalling a configuration file for the aimpoint and maneuvers and the MONTE's differential trajectory correction algorithm, can design the correction maneuver to apply and directly export the command implementation in MONTE's format.

It is also worth recalling that all the processes were automated for the importation, computation and correction, and data exportation during the simulations campaign. It surely increases the operating speed, not requiring any manual action but the initial setup. Although this is scarcely applicable to the operations phase, thanks to the experience matured, it has been possible to develop a robust list of steps to be followed, which has become the core of the developed procedure. Furthermore, extensive analyses of the entire process have highlighted some critical points, which have been included in the testing list, both to characterize the runs procedure better and to train the operators.

The developed *nav* library includes scripts for:

**I/O parsers** For any of the existing or developed formats, it has been developed a parser to cast the exchange file data into the correspondent MONTE structure. Vice-versa, for the exportation, data can be read from the ginlock and written into formatted files. These parsers exist for maneuvers, events, covariance, and asteroid physical constants files.

**Outputs data reports** A large variety of plots, tables, and notes can be extrapolated from the reconstruction and design outputs to provide a rapid but clear idea of the solution quality and robustness. These include visualization of the target conditions (reconstructed and corrected predictions), data residuals and coverage, uncertainty evolution, and pointings.

## 6.5 Testing

The pre-operations testing aims at verifying the capability of the hardware, software, and team of accomplishing the full NAV process in the required time. Therefore, tests are planned to validate the interfaces, both for the link connection and the data products format and working of the software. This latter is planned in three separated parts:

- non-real-time: namely the OD and FPC processes, as well as the data exchange, are performed without strict time constraints. Some data can be dummy generated to perform the analysis (e.g., tracking data).
- real-time nominal S/C conditions: consists of a complete loop of data exchange, analysis, and iterations with other teams, in compliance with the nominal schedule. Nominal working conditions are assumed for the S/C behavior.
- real-time off-nominal S/C conditions: similar to the previous test, but with the corruption of one or more data batch or S/C subsystem anomalies. Although not preemptively informed of the changes introduced, the OD team shall be able to correctly perform the identification of the error causes and possibly correct or mitigate its effect.

These testing activities are critical as they also allow the training of the staff. Gaining experience in atypical reconstruction conditions and under time pressure may help find criticism, which shall be reported and solved before real operations. At the present date, detailed procedures are under development for the testing.



## Chapter 7

# Conclusions and future perspectives

The CubeSat employment in deep space is a relatively new application with great potential to support typical, large, and high-cost probes. Nonetheless, the navigation of these microsattellites may be difficult when dealing with strong requirements, given the platform limitations related to the commercial off-the-shelf hardware usually employed.

In this dissertation thesis, we exploited the study of the LICIACube mission to demonstrate the capabilities of a CubeSat platform and associated ground segment to perform reliable navigation, allowing to achieve the mission goals. The build of a dedicated setup in MONTE for the navigation of the microsattellites in deep space has allowed to propagate the trajectory and assess the expected reconstruction uncertainties. The feasibility of the navigation has been demonstrated by meeting the Dimorphos encounter requirements under conservative but realistic assumptions. The robustness of the reference trajectory to achieve the mission goals have been tested extensively, providing a sensitivity analysis against the main parameters of interest. Among them, the Didymos Barycenter a-priori uncertainty has been identified as the major contributor to the probe's prediction at C/A. Also, the maneuver execution error model has demonstrated a significant effect on the results, in particular for those maneuvers closer to the last DCO, where the less tracking data are available to perform the a-posteriori reconstruction.

The trajectory reconstruction capability has been analyzed along with the pre-operation covariance analyses. A linearized approach was proposed to compute the corrective maneuvers, given a perturbed model and/or deviations in the spacecraft's initial position. The linearized model was validated against non-linear Monte Carlo analysis and used to compute the required propellant statistics, proving the mission feasibility.

In the last chapter, an overview of the ongoing activities to operations preparation was presented. Although a general draft has been prepared based on an already flown deep-space mission, procedures and testing plans adapted to a microsattellite scenario are still under the definition. The main limitation is the limited staff, which is much tinier than a typical mission. Nonetheless, the employment of already tested core functions from MONTE allows to soft some pre-operations testing, such as the OD code validation. In the context of the LICIACube mission, future activities include a detailed test phase of the end-to-end navigation activities. The tests will provide possible improvements to the developed code or additional functions to implement in order (mainly) to save time during the operations, reaching a higher level of automation.

In the more general view of the microsattellite navigation, future opportunities such as the ArgoMoon mission (whose navigation is in charge of the University of Bologna) will

allow us to extend some of the considerations made during this dissertation and possibly some of the developed tools.

---

# List of Figures

1.1	(65803) Didymos sum of daily delay-Doppler observation obtain using Arecibo.	4
1.2	DART 3D view.	5
1.3	Schematic representation of the OD process	7
2.1	LICIACube 3D view.	16
2.2	Definition of target B-plane coordinates	21
2.3	LICIACube K-inverse matrix norm.	23
2.4	LICIACube trajectory in the Dimorphos orbital plane.	26
2.5	LICIACube approach phase timeline for nominal release.	28
2.6	LICIACube approach phase timeline for contingency release.	28
3.1	Dimorphos orbit around Didymos primary during LICIACube mission (XY plane).	37
3.2	Gravitational model of Didymos primary.	41
3.3	LICIACube accelerations near to the C/A.	43
3.4	LICIACube shape.	44
4.1	LICIACube dispersion verification.	50
4.2	Comparison of B-plane dispersion and OD covariance propagations in the cases of uncontrolled and targeted trajectories.	52
4.3	Pointing angle computation.	53
4.4	LICIACube mission Doppler noise evaluation.	55
4.5	Gates error representation.	57
4.6	Expected spacecraft B-plane uncertainty ( $3\sigma$ ) against DCO, for baseline setup assuming nominal release.	61
4.7	Expected B-plane parameters uncertainty evolution ( $3\sigma$ ) with respect to DCO, for baseline setup assuming nominal release.	62
4.8	Expected DSN pointing uncertainty ( $3\sigma$ ), for baseline setup assuming nominal release.	62
4.9	Expected SPA uncertainty ( $3\sigma$ ) at delivery DCO, for baseline setup assuming nominal release.	63
4.10	Expected LEIA camera locking FOV uncertainty ( $3\sigma$ ), for baseline setup assuming nominal release.	64
4.11	Expected spacecraft B-plane formal uncertainty ( $3\sigma$ ) against DCO, for baseline setup assuming backup release.	65
4.12	Expected B-plane parameters uncertainty evolution ( $3\sigma$ ) with respect to DCO, for baseline setup assuming backup release.	65
4.13	Expected DSN pointing uncertainty ( $3\sigma$ ), for baseline setup assuming backup release.	66

4.14	Expected SPA uncertainty ( $3\sigma$ ) at delivery DCO, for baseline setup assuming backup release. . . . .	66
4.15	Expected LEIA camera locking FOV uncertainty ( $3\sigma$ ), for baseline setup assuming backup release. . . . .	67
4.16	OD results against the DART probe's covariance scale factor. . . . .	69
4.17	OD results against the Didymos Barycenter covariance scale factor. . . . .	70
4.18	OD results against the maneuvers execution error scale factor. . . . .	71
4.19	OD results against the decoupled maneuvers execution error scale factor. . . . .	73
4.20	OD robustness results analysis requirements verification. . . . .	75
4.21	OD B-plane results comparison with different observables types. . . . .	77
4.22	OD results assuming 0.1, 1 (0.300 mm/s) and 10 times the nominal Doppler noise. . . . .	78
4.23	OD results assuming 0.1, 1 (15 m) and 10 times the nominal range bias. . . . .	79
4.24	OD requirements verification with 1 lost pass. . . . .	80
4.25	OD requirements verification with losing 2 consecutive passes. . . . .	81
4.26	OD <i>a priori</i> and reconstructed epoch and $\Delta V$ ( $3\sigma$ ) of a finite burn (OM1) using impulse burn models. . . . .	84
5.1	LAMBIC OD covariance propagation diagram. . . . .	86
5.2	LAMBIC result for baseline trajectory. . . . .	90
5.3	LAMBIC B-plane dispersion at each maneuver, for baseline trajectory. . . . .	91
6.1	LICIACube operation interfaces. . . . .	95
6.2	Navigation operation process schematic [3]. . . . .	98
6.3	Maneuver design and verification sub-process schematic. . . . .	99

# List of Tables

1.1	Heliocentric orbital parameters of (65803) Didymos [37]. . . . .	4
2.1	LICIACube antenna parameters. . . . .	17
2.2	LICIACube measured group delay. . . . .	17
2.3	LICIACube cameras parameters. . . . .	18
2.4	LICIACube orbital parameters with respect to Dimorphos at the encounter epoch, in EME2000. . . . .	25
2.5	LICIACube mission main events. . . . .	26
2.6	LICIACube maneuvers schedule for nominal release. . . . .	29
2.7	LICIACube maneuvers schedule for backup release. . . . .	30
2.8	LICIACube Data Cut-Offs schedule during approach phase, nominal release case. . . . .	30
2.9	LICIACube Data Cut-Offs schedule during approach phase, backup release case. . . . .	31
3.1	Rotational model of Didymos primary: <i>a priori</i> values and uncertainties. . . . .	34
3.2	Rotational model of Didymos secondary: <i>a priori</i> values and uncertainties. . . . .	35
3.3	Didymos Barycenter state at DART nominal impact time, in EME2000. . . . .	36
3.4	Didymos barycenter state uncertainty on October 1st, 2022 at 00:00 ET, computed from DART NAV team using $DCO=T_0 - 12$ days, expressed as covariance matrix of Brouwer-Clemence set III parameters. . . . .	36
3.5	Dimorphos state at DART nominal impact time, in EME2000. . . . .	36
3.6	Gravitational model for Didymos primary. . . . .	40
3.7	Gravitational model for Didymos secondary. . . . .	41
3.8	LICIACube state (assumed coincident to DART) at release epoch, in EME2000. . . . .	42
3.9	LICIACube uncertainty with respect to Didymos Barycenter at release epoch in EME2000, computed using $DCO=T_0 - 12$ hours. . . . .	42
3.10	LICIACube geometrical and optical properties by panels. . . . .	44
4.1	Gates and time execution error model $1\sigma$ coefficients. . . . .	57
4.2	Gates and time release error model $1\sigma$ coefficients. . . . .	57
4.3	Filter nominal setup for estimated parameters, for nominal release. . . . .	59
4.4	Filter nominal setup for estimated parameters, for backup release. . . . .	60
4.5	Filter nominal setup for considered parameters. . . . .	60
4.6	Expected accuracy of the LICIACube state with respect to Dimorphos at C/A, for nominal release . . . . .	60
4.7	Expected accuracy of the LICIACube state with respect to Dimorphos at C/A, for backup release . . . . .	61
4.8	Robustness analysis results. . . . .	74

---

4.9	OD results comparison with different observables types. . . . .	76
4.10	OD filter solution of a finite burn (OM1) using impulse burn models. . . . .	83
5.1	Target point on the Dimorphos B-plane (EMO2000). . . . .	88
5.2	$\Delta V$ statistics from Monte Carlo analysis. . . . .	89
5.3	$\Delta V$ statistics from LAMBIC analysis. . . . .	89
5.4	Statistical $\Delta V$ from LAMBIC analysis. . . . .	90

# Bibliography

- [1] M.F. A'Hearn, M.J.S. Belton, W.A. Delamere, J.Kissel, K.P. Klaasen, L.A. McFadden, K.J. Meech, H.J. Melosh, P.H. Schultz, J.M. Sunshine, P.C. Thomas, J. Veverka, D.K. Yeomans, M.W. Baca, I. Busko, C.J. Crockett, S.M. Collins, M. Desnoyer, C.A. Eberhardy, C.M. Ernst, T.L. Farnham, L. Feaga, O. Groussin, D. Hampton, S.I. Ipatov, J.Y. Li, D. Lindler, C.M. Lisse, N. Mastrodemos, W.M. Owen, J.E. Richardson, D.D. Wellnitz, and R.L. White. Deep Impact: Excavating Comet Tempel 1. *Science*, 310(5746):258–264, 2005.
- [2] T.J. Ahrens and A.W. Harris. Deflection and fragmentation of near-Earth asteroids. *Nature*, 360:429–433, December 1992.
- [3] P. Antreasian, S. Ardalan, K. Criddle, R. Ionasescu, R. Jacobson, J. Jones, R. Mackenzie, D. Parcher, F. Pelletier, D. Roth, P. Thompson, and A. Vaughan. Orbit Determination Processes for the Navigation of the Cassini-Huygens Mission. In *SpaceOps 2008 Conference, Heidelberg, Germany*, May 2008.
- [4] P.G. Antreasian, M.C. Moreau, C.D. Adam, A. French, J. Geeraert, K.M. Getzandanner, D.E. Highsmith, J.M. Leonard, E. Lessac-Chenen, A. Levine, J. McAdams, L. McCarthy, D. Nelson, B. Page, J. Pelgrift, S. Rieger, E. Sahr, D. Wibben, B. Williams, K. Williams, D. Lauretta, B. Ashman, K. Berry, M. Corvin, A. Lounis, J. Lyzhof, J. Small, B. Sutter, J. Swenson, and the OSIRIS-REx Team. Early navigation performance of the OSIRIS-REx approach to Bennu. In *Guidance, Navigation, and Control, 2019*, Advances in the Astronautical Sciences, pages 141–160. Univelt Inc., 2019.
- [5] J. Bellerose, D. Roth, Z. Tarzi, and S. Wagner. The Cassini Mission: Reconstructing Thirteen Years of the Most Complex Gravity-Assist Trajectory Flown to Date. In *SpaceOps 2018 Conference, Marseille, France*, pages 575–588, May 2019.
- [6] B. Bertotti, G. Comoretto, and L. Iess. Doppler tracking of spacecraft with multi-frequency links. *Astronomy and Astrophysics*, 269:608–616, 1993.
- [7] B. Bertotti, P. Farinella, and D. Vokrouhlický. *Physics of the Solar System: Dynamics and Evolution, Space Physics, and Spacetime Structure*. Astrophysics and space science library. Kluwer Academic Publishers, 2003.
- [8] S. Bhaskaran, S. Desai, P. Dumont, B. Kennedy, W. Null, W. Owen Jr., J. Riedel, S. Synnott, and R. Werner. Orbit Determination Performance Evaluation of the Deep Space 1 Autonomous Navigation System. In *Spaceflight Mechanics Meeting, Monterey, California*, January 1998.
- [9] G.J. Bierman. *Factorization Methods for Discrete Sequential Estimation*. Dover Books on Mathematics. Dover Publications, 2006.

- [10] B.G. Bills, S.W. Asmar, A.S. Konopliv, R.S. Park, and C.A. Raymond. Harmonic and statistical analyses of the gravity and topography of Vesta. *Icarus*, 240:161–173, September 2014.
- [11] A. Capannolo, G. Zanotti, M. Lavagna, E. Mazzotta Epifani, E. Dotto, V. Della Corte, I. Gai, M. Zannoni, M. Amoroso, and S. Pirrotta. Challenges in LICIA Cubesat trajectory design to support DART mission science. *Acta Astronautica*, 182:208–218, 2021.
- [12] I. Carnelli, A. Gálvez, and F. Ongaro. Learning to deflect Near Earth Objects: Industrial design of the Don Quijote mission. In *57th International Astronautical Congress*, volume A3, page 5.05, November 2006.
- [13] A.F. Cheng, A.S. Rivkin, P. Michel, J. Atchison, O. Barnouin, L. Benner, N.L. Chabot, C. Ernst, E.G. Fahnestock, M. Kueppers, P. Pravec, E. Rainey, D.C. Richardson, A.M. Stickle, and C. Thomas. AIDA DART asteroid deflection test: Planetary defense and science objectives. *Planetary and Space Science*, 157:104–115, 2018.
- [14] S. R. Chesley, D. Farnocchia, and S. P. Naidu. Asteroid (65803) Didymos Ephemeris Delivery, JPL Solution 181. JPL IOM 392R-21-003, February 2021.
- [15] M.K.J. Chung, Shyam Bhaskaran, S.R. Chesley, Allen Halsell, C.E. Helfrich, D.C. Jefferson, T.P. McElrath, B.P. Rush, T.C.M. Wang, and C.W.L. Yen. Epoxi trajectory and maneuver analyses. *Advances in the Astronautical Sciences*, 142:1213–1226, January 2012.
- [16] B. Cotugno. LICIACube data for analyses, personal communication, April 2019.
- [17] The CubeSat Program, Cal Poly San Luis Obispo. *CubeSat Design Specification*, 13 edition, February 2014.
- [18] DART investigation team. Design Reference Asteroid rev. 3.11. Technical report, The Johns Hopkins University Applied Physics Laboratory, November 2021.
- [19] J. de León, J. Licandro, M. Serra-Ricart, N. Pinilla-Alonso, and H. Campins. Observations, compositional, and physical characterization of near-Earth and Mars-crosser asteroids from a spectroscopic survey. *Astronomy and Astrophysics*, 517:25, July 2010.
- [20] R.P. de Santayana and M. Lauer. Optical measurements for rosetta navigation near the comet. In *25th International Symposium on Space Flight Dynamics, Munich, Germany*, 2015.
- [21] V. Di Tana, B. Cotugno, S. Simonetti, G. Mascetti, E. Scorzafava, and S. Pirrotta. ArgoMoon: There is a Nano-Eyewitness on the SLS. *IEEE Aerospace and Electronic Systems Magazine*, 34(4):30–36, 2019.
- [22] V. Di Tana, G. Mascetti, S. Pirrotta, C. Fiori, R. Rinaldo, S. Simonetti, and B. Cotugno. ArgoMoon: Challenges and design solutions for the development of a Deep Space Small Satellite. In *69th International Astronautical Congress 2018*. International Astronautical Federation, October 2018.
- [23] E. Dotto, V. Della Corte, M. Amoroso, I. Bertini, J.R. Brucato, A. Capannolo, B. Cotugno, G. Cremonese, V. Di Tana, I. Gai, S. Ieva, G. Impresario, S.L. Ivanovski,

- M. Lavagna, A. Lucchetti, E. Mazzotta Epifani, A. Meneghin, F. Miglioretti, D. Modenini, M. Pajola, P. Palumbo, D. Perna, S. Pirrotta, G. Poggiali, A. Rossi, E. Simioni, S. Simonetti, P. Tortora, M. Zannoni, G. Zanotti, A. Zinzi, A.F. Cheng, A.S. Rivkin, E.Y. Adams, E.L. Reynolds, and K. Fretz. LICIAcube - The Light Italian Cubesat for Imaging of Asteroids In support of the NASA DART mission towards asteroid (65803) Didymos. *Planetary and Space Science*, 199:105–185, 2021.
- [24] C. Duncan. Iris for INSPIRE CubeSat Compatible, DSN Compatible Transponder. In *27th Annual AIAA/USU Small Satellite Conference, Logan, Utah*, 2013.
- [25] S. Evans, W. Taber, T. Drain, J. Smith, H.C. Wu, M. Guevara, R. Sunseri, and J. Evans. MONTE: the next generation of mission design and navigation software. *CEAS Space Journal*, 10(1):79–86, 2018.
- [26] D. Farnocchia, S. Eggl, P. W. Chodas, J. D. Giorgini, and S. R. Chesley. Planetary encounter analysis on the B-plane: a comprehensive formulation. *Celestial Mechanics and Dynamical Astronomy*, 131(36), August 2019.
- [27] F. Ferrari, V. Franzese, M. Pugliatti, C. Giordano, and F. Topputo. Preliminary mission profile of Hera’s Milani CubeSat. *Advances in Space Research*, 67(6):2010–2029, 2021.
- [28] A. Fujiwara, J. Kawaguchi, D. K. Yeomans, M. Abe, T. Mukai, T. Okada, J. Saito, H. Yano, M. Yoshikawa, D. J. Scheeres, O. Barnouin-Jha, A. F. Cheng, H. Demura, R. W. Gaskell, N. Hirata, H. Ikeda, T. Kominato, H. Miyamoto, A. M. Nakamura, R. Nakamura, S. Sasaki, and K. Uesugi. The Rubble-Pile Asteroid Itokawa as Observed by Hayabusa. *Science*, 312(5778):1330–1334, 2006.
- [29] I. Gai and M. Zannoni. *LICIAcube Navigation Interface Control Document, rev. 1.3A*. University of Bologna, June 2021.
- [30] H.R. Goldberg, Ö.K. Birgin Ritter, A. Henrique, P. Tortora, C. Prioroc, B. Garcia Gutierrez, P. Martino, and I. Carnelli. The Juventas CubeSat in Support of ESA’s Hera Mission to the Asteroid Didymos. In *33rd Annual AIAA/USU Conference on Small Satellites*, 2019.
- [31] L.A. Gomez Casajus. *Development of methods for the global ephemeris estimation of the gas giant satellite systems*. PhD thesis, University of Bologna, 2018.
- [32] T. D. Goodson. Monte-carlo maneuver analysis for the microwave anisotropy probe. In *AAS/AIAA Astrodynamics Specialist Conference*, 2001.
- [33] R.J. Hanson and F.T. Krogh. A Quadratic-Tensor Model Algorithm for Nonlinear Least-Squares Problems with Linear Constraints. *ACM Trans. Math. Softw.*, 18(2):115–133, June 1992.
- [34] X. Hu and C. Jekeli. A numerical comparison of spherical, spheroidal and ellipsoidal harmonic gravitational field models for small non-spherical bodies: examples for the Martian moons. *Journal of Geodesy*, 89:159–177, February 2014.
- [35] L. Iess, F. Budnik, C. Colamarino, A. Corbelli, M. Di Benedetto, V. Fabbri, A. Graziani, R. Hunt, N. James, M. Lanucara, R. Maddé, M. Marabucci, G. Mariotti, M. Micolino, P. Racioppa, L. Simone, P. Tortora, M. Westcott, and M. Zannoni.

- ASTRA: Interdisciplinary study on enhancement of the end-to-end accuracy for spacecraft tracking techniques. In *Proceedings of the International Astronautical Congress, IAC*, volume 5, January 2012.
- [36] M.K. Jah. Derivation of the B-Plane (Body Plane) and its associated parameters. In *A Lecture Series on Orbit Mechanics and Interplanetary Mission Design*. University of Colorado, 2002.
- [37] Jet Propulsion Laboratory - California Institute of Technology. Small-body database didymos solution 181. [https://ssd.jpl.nasa.gov/tools/sbdb\\_lookup.html#/?sstr=65803](https://ssd.jpl.nasa.gov/tools/sbdb_lookup.html#/?sstr=65803). Accessed: 2022-01-23.
- [38] Jet Propulsion Laboratory - California Institute of Technology. *DSN Telecommunications Link Design Handbook, 101 70-m Subnet Telecommunication Interfaces, Rev. G*, September 2019.
- [39] S. Kikuchi, F. Terui, N. Ogawa, T. Saiki, G. Ono, K. Yoshikawa, Y. Takei, Y. Mimasu, H. Ikeda, H. Sawada, S. V. Wal, S. Sugita, S. Watanabe, and Y. Tsuda. Design and Reconstruction of the Hayabusa2 Precision Landing on Ryugu. *Journal of Spacecraft and Rockets*, 57(5):1033–1060, 2020.
- [40] E. Kulu. Nanosatellites by launch years. <https://www.nanosats.eu/>. Accessed: 2022-01-20.
- [41] D. Lubey and J. Bellerose. DART and Didymos uncertainties, personal communication, October 2021.
- [42] V. Marchese. *ARG-ICD-LCC-0221, LICIA Cube Satellite Proto-Flight Model Main Properties, rev. 1*. Argotec, May 2021.
- [43] G. Mariotti and P. Tortora. Experimental validation of a dual uplink multifrequency dispersive noise calibration scheme for Deep Space tracking. *Radio Science*, 48(2):111–117, 2013.
- [44] T. Martin-Mur and B. Young. Navigating MarCO, the First Interplanetary CubeSats. In *18th Australian International Aerospace Congress, Melbourne*, February 2019.
- [45] P. Michel, M. Kueppers, H. Sierks, I. Carnelli, A.F. Cheng, K. Mellab, M. Granvik, A. Kestilä, T. Kohout, K. Muinonen, A. Näsilä, A. Penttilä, T. Tikka, P. Tortora, V. Ciarletti, A. Hérique, N. Murdoch, E. Asphaug, A. Rivkin, O. Barnouin, A. Campo Bagatin, P. Pravec, D.C. Richardson, S.R. Schwartz, K. Tsiganis, S. Ulamec, and O. Karatekin. European component of the AIDA mission to a binary asteroid: Characterization and interpretation of the impact of the DART mission. *Advances in Space Research*, 62(8):2261–2272, 2018.
- [46] P. Muñoz, F. Budnik, V. Companys, B. Godard, C.M. Casas, Morley T., and V. Janarthanan. Rosetta navigation during lander delivery phase and reconstruction of Philae descent trajectory and rebound. In *25th International Symposium on Space Flight Dynamics*, 2015.
- [47] S. P. Naidu, S. R. Chesley, and D. Farnocchia. Updated orbit of Dimorphos, the satellite of binary near-Earth asteroid (65803) Didymos. JPL IOM 392R-21-004, February 2021.

- [48] S.P. Naidu, L.A.M. Benner, M. Brozovic, M.C. Nolan, S.J. Ostro, J.L. Margot, J.D. Giorgini, T. Hirabayashi, D.J. Scheeres, P. Pravec, P. Scheirich, C. Magri, and J.S. Jao. Radar observations and a physical model of binary near-Earth asteroid 65803 Didymos, target of the DART mission. *Icarus*, 348:113777, 2020.
- [49] R.S. Park, A.S. Konopliv, S.W. Asmar, B.G. Bills, R.W. Gaskell, C.A. Raymond, D.E. Smith, M.J. Toplis, and M.T. Zuber. Gravity field expansion in ellipsoidal harmonic and polyhedral internal representations applied to Vesta. *Icarus*, 240:118–132, September 2014.
- [50] D. Perna, M.A. Barucci, and M. Fulchignoni. The near-Earth objects and their potential threat to our planet. *Astronomy and Astrophysics*, 21:65, September 2013.
- [51] R. Phillips and M. Wieczorek. Potential anomalies on a sphere: Applications to the thickness of the lunar crust. *Journal of Geophysical Research. Planets*, 103(E1):1715–1724, 1998.
- [52] P. Pravec. Photometric Survey for Asynchronous Binary Asteroids. *Society for Astronomical Sciences Annual Symposium*, 24:61, April 2005.
- [53] P. Pravec, L.A.M. Benner, M.C. Nolan, P. Kusnirak, D. Pray, J.D. Giorgini, R.F. Jurgens, S.J. Ostro, J.L. Margot, C. Magri, A. Grauer, and S. Larson. (65803) 1996 GT. *IAU Circ.*, 8244:2, November 2003.
- [54] P. Pravec, P. Scheirich, P. Kušnirák, K. Hornoch, A. Galad, S.P. Naidu, D. Pray, J. Vilagi, Š. Gajdoš, L. Kornos, Y. Krugly, W.R. Cooney, J. Gross, D. Terrell, N. Gaftonyuk, J. Pollock, M. Husarik, V. Chiorny, R. Stephens, and A. LaCluyze. Binary asteroid population. 3. Secondary rotations and elongations. *Icarus*, 267, December 2015.
- [55] A.S. Rivkin, N.L. Chabot, A.M. Stickle, C.A. Thomas, D.C. Richardson, O. Barnouin, E.G. Fahnestock, C.M. Ernst, A.F. Cheng, S. Chesley, S. Naidu, T.S. Statler, B. Barbee, H. Agrusa, N. Moskovitz, R. Terik Daly, P. Pravec, P. Scheirich, E. Dotto, V. Della Corte, P. Michel, M. Küppers, J. Atchison, and M. Hirabayashi. The Double Asteroid Redirection Test (DART): Planetary Defense Investigations and Requirements. *The Planetary Science Journal*, 2(5):173, August 2021.
- [56] P. Scheirich and P. Pravec. Results from modeling of photometric data of Didymos (2003-2021), September 2021.
- [57] A.B. Sergeevsky, G.C. Snyder, and R.A. Cunniff. *Interplanetary mission design handbook. Earth to Mars ballistic mission opportunities, 1990-2005*, volume I, part 2. NASA/JPL, September 1983. JPL PUBLICATION 82-43.
- [58] S. Simonetti. LICIACube pointing budget, personal communication, May 2021.
- [59] B.D. Tapley, B.E. Schutz, and G.H. Born. Fundamentals of Orbit Determination. In *Statistical Orbit Determination*, chapter 4, pages 159–284. Academic Press, Burlington, 2004.
- [60] C.L. Thornton and J.S. Border. *Radiometric tracking techniques for deep-space navigation*. John Wiley & Sons, 2003.

- 
- [61] D.A. Vallado, Wayne D., and McClain. F. Statistical Orbit Determination. In *Fundamentals of Astrodynamics and Applications*, chapter 9, pages 649–740. McGraw-Hill, 1997.
- [62] T. Villela, C. A. Costa, A. M. Brandão, F. T. Bueno, and R. Leonardi. Towards the Thousandth CubeSat: A Statistical Overview. *International Journal of Aerospace Engineering*, 2019, January 2019.
- [63] S.V. Wagner and T.D. Goodson. Execution-error modeling and analysis of the Cassini-Huygens spacecraft through 2007. *Proceedings of the AAS/AIAA Space Flight Mechanics Meeting*, January 2008.
- [64] R. Walker, D. Binns, C. Bramanti, M. Casasco, P. Concari, D. Izzo, D. Feili, P. Fernandez, J.G. Fernandez, P. Hager, D. Koschny, V. Pesquita, N. Wallace, I. Carnelli, M. Khan, M. Scoubeau, and D. Taubert. Deep-space CubeSats: thinking inside the box. *Astronomy & Geophysics*, 59(5):5.24–5.30, October 2018.
- [65] K.J. Walsh. Rubble Pile Asteroids. *Annual Review of Astronomy and Astrophysics*, 56(1):593–624, September 2018.
- [66] K.J. Walsh and D.C. Richardson. Binary near-Earth asteroid formation: Rubble pile model of tidal disruptions. *Icarus*, 180(1):201–216, January 2006.
- [67] T.C. Wang, R. Stanford, and P. Sunseri, R. and Breckheimer. Survey of optimization techniques for nonlinear spacecraft trajectory searches. In *Astrodynamics Conference*, page 4285, 1988.
- [68] R.A. Werner. The Gravitational Potential of a Homogeneous Polyhedron or Don't Cut Corners. *Celestial Mechanics and Dynamical Astronomy*, 59(3):253–278, July 1994.
- [69] R.A. Werner and D.J. Scheeres. Exterior Gravitation of a Polyhedron Derived and Compared with Harmonic and Mascon Gravitation Representations of Asteroid 4769 Castalia. *Celestial Mechanics and Dynamical Astronomy*, 65:313–344, September 1996.
- [70] S.C. Werner and B.A. Ivanov. Exogenic Dynamics, Cratering, and Surface Ages. In Gerald Schubert, editor, *Treatise on Geophysics (Second Edition)*, pages 327–365. Elsevier, Oxford, second edition edition, 2015.